Applications of Parameter Inference and Modelling in Cardiac Single-Cell Action Potential Models

Antesar Mohammed Aldawoud

SUBMITTED IN FULFILMENT OF THE REQUIREMENTS FOR THE DEGREE OF
DOCTOR OF PHILOSOPHY

SCHOOL OF MATHEMATICS AND STATISTICS

COLLEGE OF SCIENCE AND ENGINEERING

09 2024

Abstract

Cardiac electrophysiological modelling has long been a valuable tool for exploring both normal and abnormal heart rhythms, playing a crucial role in diagnosing heart conditions and developing effective therapies. This thesis focuses on single-cell cardiac electrophysiology, with particular attention to the variability in action potential (AP) and its impact on anti-arrhythmic treatments. The primary goal is to investigate this common issue in cardiac electrical excitation models and understand its implications for anti-arrhythmic therapies. To achieve this, a variety of action potential models, ranging from complex to simplified, are employed to provide an analysis.

Firstly, a method is presented that uses an asymptotic approximation of action potential duration (APD) in a simplified model to study ion-channel block dynamics. This approach involves determining the specific properties of each myocyte based on the parameter values of a selected model. Drug effects on ion conductance are quantified using a multiplicative factor, and a mathematical formula is developed to approximate APD. This formula is then used to establish model parameters as functions of APD and drug-induced changes in APD for each heart cell. Additionally, two protocol-related parameters are calibrated using an adaptive-domain approach based on optimal excitability. This precise formulation allows for direct assessment of the conditions required to maintain a constant APD or its variations. It also enables predictions about the proportion of excitable cells after drug application, as well as insights into stimulus periods and dose-response relationships, consistent with experimental data.

Subsequently, a regression method is developed to predict drug responses in cardiac electrophysiology models by assessing how alterations in ion channel conductances affect model outputs. The method focuses on predicting changes in action potential duration (APD) following drug administration. The Ordinary Least Squares regression model provided accurate predictions, effectively capturing the relationship between drug-induced changes in ion channel conductances and APD. In addition to the standard regression model, an advanced approach is employed by incorporating nonlinear terms to capture the complex relationships between conductances and physiological biomarkers. These nonlinear predictors enable the model to account for interactions and dependencies that linear models often overlook. The enhanced model unables more accurate predictions of the effects of ionic conductances..

Finally, a method is introduced to reproduce action potential variability observed in experimental rabbit cardiomyocytes using Gaussian process emulators and rejection sampling. The method accurately captures variations in APD and correlates them with changes in ionic conductances across a population of models. By utilizing rejection sampling in combination with GP emulation, large populations of models are efficiently generated, enabling the study of the interactions between ionic conductances, action potentials, and drug effects without requiring extensive computational resources.

This thesis enhances the understanding of cardiac electrophysiology by addressing variability in action potential and its implications for anti-arrhythmic treatments. It proposes an integrated approach combining modelling and experimentation, offering new insights into the complex dynamics of cardiac function.

Contents

List of Tables

List of Figures

Acknowledgements

Initially, I would like to extend sincere gratitude to the government of Saudi Arabia and the Saudi Electronic University for giving me the opportunity to pursue my PhD.

I am deeply appreciative of the assistance I have received from many people throughout my PhD. Most importantly, I would like to extend my deepest thanks to my research supervisors at the University of Glasgow, Professor Radostin D. Simitev and Dr. Hao Gao, for their encouragement, patience, motivation, and extensive knowledge. Their exceptional guidance helped me in my research, develop many skills, including coding, and write this thesis.

Additionally, I would like to extend my gratitude to Muhamad Hifzhudin Bin Noor Aziz for his assistance, as well as for his insightful discussions and feedback on my research.

I am extremely grateful to my family, my husband Soud, my daughter Sarah, and my son Abdulaziz, for their constant and loving support, devotion, and understanding, which have enabled me to successfully complete this research. I am also deeply appreciative of all the love, unwavering encouragement, and prayers from my parents and siblings.

Declaration

I declare that this thesis unless otherwise indicated by citation, is the result of my work and was not submitted for any other degree at the University of Glasgow or any other educational institutions.

Abbreviations

V_m	Membrane voltage
AP	Action potential
APA	Action potential amplitude
APD	Action potential duration
APD90, APD50	Action potential duration at 90%,and 50% repolarisation respectively
RMP	Resting membrane potential
CaT	Calcium transient
CaTA	Calcium transient amplitude
I_{CaL}	L-type calcium current
I_{CaT}	T-type calcium current
I_{K1}	Inward rectifier potassium current
I_{Kr}	Rapid delayed rectifier potassium current
I_{Kss}	Slow delayed rectifier potassium current
I_{Na}	Fast sodium current
I_{NaK}	Sodium - potassium ATPase current
I_{NCX}	Sodium - calcium exchanger current
I_{to}	Transient outward potassium current
GP	Gaussian process

Chapter 1

Introduction

1.1 Introduction

Cardiac action potentials (APs) are electrical impulses generated by the movement of ions through specialised channels and exchangers located across the membranes of cardiomyocytes, the heart's muscle cells. These action potentials are crucial for initiating and coordinating the contractions that pump blood throughout the body. The variation in action potentials across different regions of the heart is significant and is depicted in Figure 1.1, highlighting how these differences contribute to the heart's overall function.

The study of heart electrophysiology, which focuses on the electrical properties of the heart, has been an area of intense research. Understanding electrophysiology is essential not only for comprehending the normal functioning of the heart but also for diagnosing and treating a wide range of cardiac disorders. These disorders, particularly arrhythmiasconditions where the heart beats irregularly, too fast, or too slowpose serious health risks.

In the United Kingdom, arrhythmias affect more than 2 million people, according to the NHS (National Health Service n.d.). Some arrhythmias are associated with severe cardiac conditions that can lead to sudden cardiac death. Alarmingly, this accounts for approximately 100,000 deaths annually in the UK alone (National Health Service n.d.). The primary types

of arrhythmias are atrial fibrillation (AF), which is defined by the rapid and irregular beating of the atria; supraventricular tachycardia, which is a rapid heart rate that originates above the heart's ventricles; bradycardia, which is characterised by an abnormally slow heart rate; heart block, a condition in which the electrical signals are partially or completely blocked as they travel through the heart; and ventricular fibrillation, a life-threatening arrhythmia that causes the ventricles to contract ineffectively instead of pumping blood (Zipes et al. 2017).

The consequences of these arrhythmias are significant, as they can result in serious problems such as stroke, cardiac insufficiency, and abrupt cardiac arrest (Bonow et al. 2011). Hence, electrophysiology plays a crucial role not just in comprehension but also in the advancement of life-saving interventions and treatments (Muszkiewicz et al. 2016). Through the examination of the complex nature of cardiac action potentials and their diverse variations, researchers might contribute to advancement in treating these critical heart rhythm diseases. For decades, cardiac electrophysiology modelling has been an essential tool for researching both normal and pathological heart functions. Studies conducted at the membrane, cellular, tissue, and organ levels have contributed to the development of a wide range of biophysically detailed cardiac action potential (AP) models (Muszkiewicz et al. 2016). A common practice in model development is to begin with parameter identification for specific ion channels using whole-cell voltage-clamp experiments. Typically, model parameters are assigned fixed values, resulting in a single predicted outcome. However, the APs recorded from actual cardiac cells during experiments show variability, both within the same cell from one beat to another (intrinsic variability) and between different cells (extrinsic variability)(Johnstone et al. 2016). The goal of this thesis is to explore variability in cardiac electrophysiology in both normal and abnormal conditions, as well as under the influence of drugs.

1.2 Variability in Cardiac Electrophysiology

Variability is a fundamental characteristic of all biological systems (Trayanova et al. 2023). It is particularly evident in physiological functions among individuals of the same species and plays a significant role in the progression and treatment of diseases (Marder and Taylor 2011). In cardiac electrophysiology, variability is pronounced both between and within cells, even among

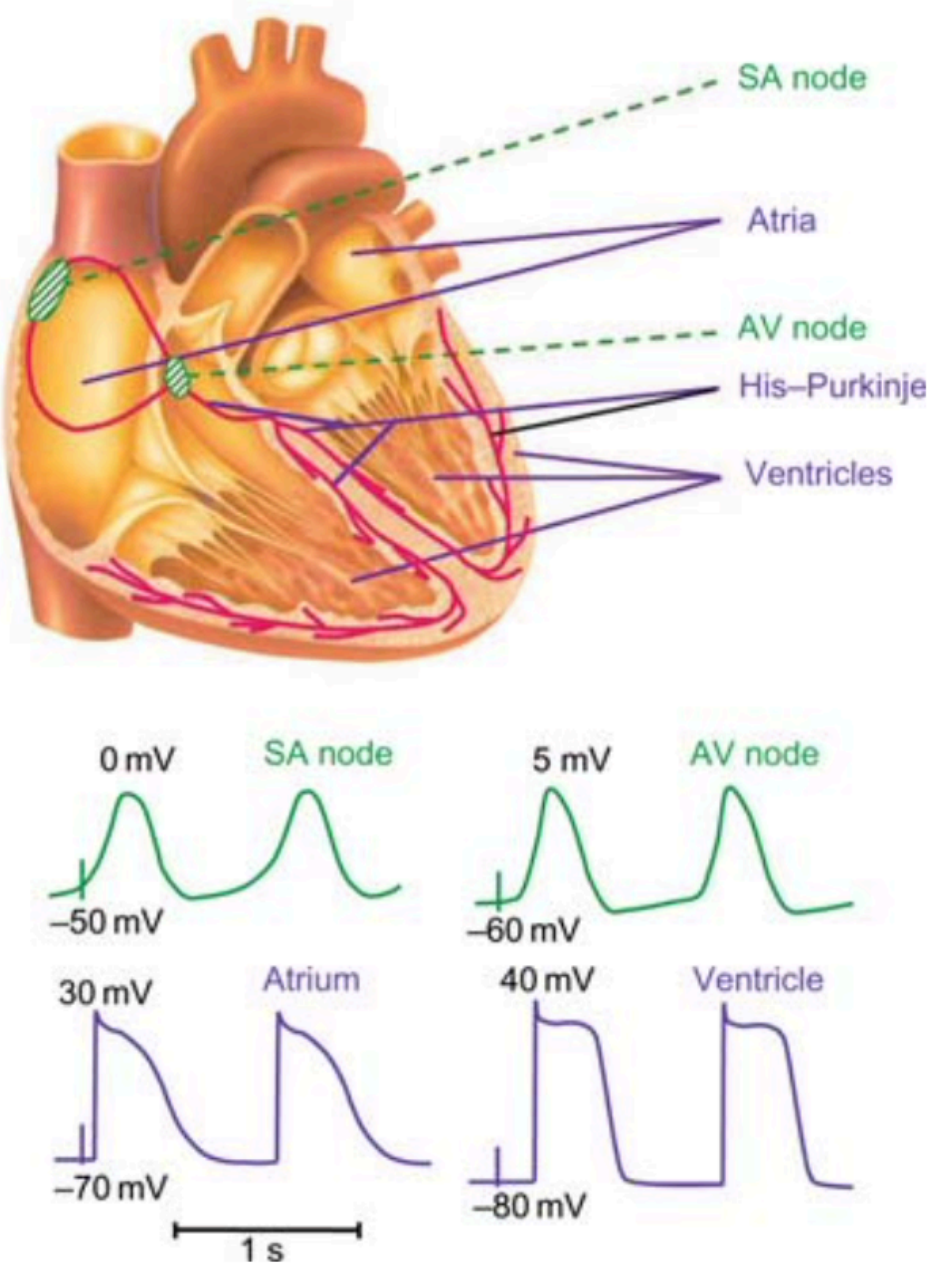

Figure 1.1: Various regions in the heart and typical corresponding APs. Green for SA, AV nodes; violet, for Atria and Ventricle. Figure is from (Michael et al. 2009)

cells from the same region of the heart (Feng et al. 1998). At the level of individual cardiomyocytes, variability is observed in the shape and duration of the action potential (AP). Notably, recent studies have shown that cardiomyocytes from healthy animals with nearly identical genetic backgrounds still exhibit significant heterogeneity (Lachaud et al. 2022).

Several key elements contribute to variability in cardiac electrophysiology. One major factor is ion channel gating, where non-linear dynamics, such as APD alternans, can cause changes within cells (Johnstone et al. 2016). Additionally, extrinsic variability may arise from natural differences among cells, such as cell size or the expression levels of ion channels. Measurement errors during experimental data collection can further increase variability when these data are used to derive parameters for cardiac AP models (Clayton et al. 2020). A potential source of variability lies in the biophysical processes that regulate the flow of ionic currents across the cellular membrane. Proteins crucial for electrophysiological function control the sarcolemmal flux of ions such as sodium, calcium, and potassium. Any imbalance in these ionic currents can lead to variations in AP morphology and duration (Muszkiewicz et al. 2016).

Intra-subject variability in electrophysiology is highlighted in studies such as (Bueno-Orovio et al. 2012), which investigates spatial heterogeneities and variations in repolarisation across different regions of the heart. Factors such as sex and age have been recognised as significant contributors to variability among individuals. For instance, (Sims et al. 2008) demonstrated that sex, age, and regional differences in the expression of the I_{CaL} ionic current influence arrhythmia characteristics in rabbits. On a cellular level, variability in ion concentrations inside and outside cells impacts AP features like the resting membrane potential (RMP) and the duration of AP at 90% repolarisation (APD90) (Passini et al. 2014). Additionally, inter-cellular variability in cardiac cell volume and membrane capacitance has been linked to the patient's age, as shown in (Polak and Fijorek 2012). Temporal variability, such as beat-to-beat changes in the action potential, is influenced by factors like AP alternans and ion channel kinetics (Walmsley et al. 2015).

Exploring physiological variability through experimental approaches alone is challenging due to the need to average data to control experimental errors. Recent studies have demonstrated the effectiveness of computer models in examining the underlying causes of physiological variability (Britton et al. 2013 and Groenendaal et al. 2015). Unlike traditional computational modelling, which generates only an average virtual cardiomyocyte, a collection of averaged

data may not accurately represent any specific cardiomyocyte (Ni et al. 2018). To address this limitation, the population of models approach has gained popularity in electrophysiological modelling and has been used to investigate variability in cardiac APs (Muszkiewicz et al. 2016). later we provide more information about this approach.

Addressing the inter-subject and intra-subject heterogeneity in physiological and pathological functions remains a significant challenge in biology and medicine (Sánchez et al. 2014). Historically, both experimental and computational studies have often overlooked the importance of variability, despite its critical role in understanding cardiac function. Recently, however, new modelling frameworks have been developed to explore the mechanisms underlying physiological variability in cardiac electrophysiology and its contribution to increased arrhythmic risk. These frameworks have been designed to investigate various arrhythmia conditions across different animal species, including humans.

To analyse variability in cardiac electrophysiology, several methodologies have been employed. These include cell-specific modelling approaches, sensitivity analysis methods, and the use of populations of cardiac cell models that are subject to experimental constraints and calibration. These methods have significantly enhanced our understanding of the heterogeneity present in both normal and abnormal cardiac function. Below we provide a brief overview of the research conducted using these methodologies to address variability in cardiac electrophysiology.

1.2.1 Cell-Specific Modelling Approach

The cell-specific modelling approach is a powerful technique designed to create biophysically detailed models of specific cells used in experiments (Muszkiewicz et al. 2016). This method addresses particular research questions by closely matching experimental data with models. However, the complexity of the protocols involved limits the number of cells that can be investigated and modeled, thereby restricting the exploration of the full parameter space seen in experimentally-calibrated populations of models. (Syed et al. 2005) pioneered this technique

by using a genetic algorithm to align a biophysically complex model of the human atrial action potential with AP traces produced by several cell models, as well as with experimental data. This methodology was further employed in subsequent studies such as the one by (Davies et al. 2012).

1.2.2 Sensitivity Analysis Approach

Sensitivity analysis is a method used to investigate the impact of varying model parameters on outputs like the action potential and intracellular calcium transients (Muszkiewicz et al. 2016). This technique involves altering parameters of interest around baseline model values, typically one at a time, with variations ranging from $\pm 15\%$ to $\pm 30\%$ from the baseline parameter value. For instance, (Romero et al. 2009) used univariate sensitivity analysis in a model of human ventricular single cells to study the effects of such variations on pre-clinical measures associated with arrhythmia risk, such as APD. Similarly, (Pueyo et al. 2010) employed sensitivity analysis to gain new insights into the processes of ventricular rate adaptation and its connection with proarrhythmic risk in humans.

1.2.3 Population of Models Approach

A population of cell models is created by varying a set of model parameters, typically the maximum channel conductances. Each model in the population has slightly different electrophysiological characteristics. This population can then be calibrated to match experimental data, such as action potential characteristics (Britton et al. 2013). Alternative approaches include Bayesian calibration (Johnstone et al. 2016) or Gaussian process emulators (Chang et al. 2015). The resulting population of models can be used to analyse the mechanisms associated with specific parameters of a single model.

The population of models approach is considered an extension of sensitivity analysis, as it involves varying multiple parameters simultaneously. Originally employed in cardiac electrophysiology by researchers like (Sobie and Sarkar 2011; Sobie 2009), this method modifies multiple parameters in ventricular cell models, with values drawn from a log-normal distribution centered on their baseline values. Regression analysis is then used to develop simplified models that link changes in ionic current parameters to changes in cellular characteristics. This

approach has been applied to examine the influence of variability on repolarisation reserve and the response to ionic channel block. For example, (Devenyi and Sobie 2016) recently used this methodology to investigate the impact of calcium transients in rat cardiomyocytes by iterating with experiments. Further work using this method can be found in studies by (Cummins et al. 2014 and Sarkar et al. 2012).

1.2.4 Experimentally-Calibrated Populations of Models Approach

Experimentally calibrated populations of models involve using ensembles of computer models constrained by experimental data to investigate the factors contributing to physiological variability under various conditions, such as disease and drug effects (Muszkiewicz et al. 2016). This approach has been employed to explore variability in both inter-subject and intra-subject conditions by using experimentally calibrated populations of single cardiomyocyte models. The first use of this approach in neuroscience was pioneered by (Marder and Taylor 2011), and it has since gained popularity in cardiac excitation studies. (Passini et al. 2016) applied this approach to study hypertrophic cardiomyopathy, a genetic disorder of the heart that carries an increased risk of arrhythmias due to the lack of specific drug treatments. Additionally, (Zhou et al. 2013 and Zhou et al. 2016) used this technique to investigate the mechanisms behind cardiac alternans, which refers to the regular variations between repeated action potentials produced by a single cell. In recent work by (Sánchez et al. 2014), they calibrated a population of models using experimental datasets from over 450 cell samples obtained from individuals with atrial fibrillation (AF) and sinus rhythm. This study explored the ionic mechanisms driving inter-subject heterogeneity in human atrial AP characteristics between AF and baseline cells.

1.3 A recent Study on Variability of Action Potential

Recent research has highlighted considerable differences in ion channel expression among individual cells (Clark et al. 2023). Tables 1.1 and 1.2 at the end of this chapter summarise key studies that have explored this variability, providing further insights into the underlying mechanisms. While 1.3 summarises the key elements in each chapter of this thesis.

We are particularly interested in the recent research conducted by (Lachaud et al. 2022) highlighted in Table 1.2, which offers valuable insights into the variability of action potential (AP) waveform within the left ventricle (LV) of individual hearts. In this study (Lachaud et al. 2022), AP characteristics of nearly 500 isolated cardiomyocytes were measured using voltage-sensitive fluorescent dyes. These cells, obtained from specific regions of the left ventricular wall of 12 rabbit hearts, had their APD values recorded before and after inhibiting specific ion channels with two different drugs. The study revealed a surprising variability in APD90 among the healthy, uncoupled cardiomyocytes before drug administration. At a stimulation rate of 2 Hz, the interquartile range of APD90 was 40 to 50 ms, with a median value of 250 ms. This variation, which was not attributable to cell dissociation damage, was significantly larger than the regional differences observed within single hearts or between different hearts. Furthermore, after inhibiting the IK(r) ionic current with 30 nM Dofetilide and the ICa(L) current with 1μM Nifedipine, cells with nearly identical baseline APD90 values exhibited a wide range of different ΔAPD90 responses.

Cardiac Model	Uncertain inputs	Outputs	Method	Results
Sobie 2009				
Luo and Rudy 1991 Fox et al. 2002 Kurata et al. 2005	Relative Current Strength	APD Vpeak & Vrest $\Delta\left[\mathrm{Ca}^{2+}\right]_{\mathrm{i}}$	PLS Regression	Presentd a novel method that accurately quantifies parameter sensitivities in cardiac models enhancing the evaluation of computational predictions.
Sarkar and Sobie 2010				
Tusscher et al. 2004 Hund et al. 2008	Relative Current Strength	AP & Ca^{2+} biomarkers	Inverse Regression	Presentd a regression-based method that precisely defines most ion conductances in a ventricular myocyte model enabling prediction of parameter changes
Gemmell et al. 2014				
Shannon et al. 2004 Mahajan et al. 2008	Relative Current Strength	APD90, APD50	Clutter-based Dimension Reordering	Reproduced the experimentally observed variability in ventricular APD, identified key conductances and their interactions that influence repolarisation.
Chang et al. 2015				
Luo and Rudy 1991	Relative Current Strength	APD90, APD50	Bayesian Emulation	Built GP emulators effectively analyse uncertainty and sensitivity in models, efficiently predicting how key outputs are influenced by specific parameters.
Morotti and Grandi 2017				
Morotti et al. 2016	Relative Current Strength	EAD	Logistic Regression	Identified the key ion conductances which cause early afterdepolarisations, confirming mechanistic insights through logistic regression analysis.
Gong and Sobie 2018				
Paci et al. 2013 Shannon et al. 2004 Livshitz and Rudy 2009 O'Hara et al. 2011	Relative Current Strength	APD90 & CaTa	Multi-variable Regression	Developed a regression model that predicts drug responses across different cell types, providing a valuable approach to enhance drug development and overcome limitations of experimental models.

Table 1.1: Studies that addressed and assessed variability in cardiac electrophysiology

Cardiac Model	Uncertain inputs	Outputs	Method	Results
Pouranbarani et al. 2019				
Tusscher et al. 2004 Iyer et al. 2004	Relative Current Strength	Membrane resistance R_m	Multi-objective optimisation	Introduced a multi-objective fitting method that accurately reproduced R_m in cardiac cells, balancing the trade-off between fitting AP waveforms and R_m
Feeny et al. 2020				
Electrocardiogram test	Clinical features ECG features	prediction score of cardiovascular mortality	Machine Learning	Explored how AI and ML transforming cardiac EP by enhancing disease detection, diagnosis & patient prediction while addressing challenges in their clinical practice
Coveney and Clayton 2020				
Courtemanche et al. Maleckar et al. 2009	Relative Current Strength	APD90, APD50 Vmax, V20, V40 dV_{m}/dt, & $\mathrm{Rest}_{\mathrm{Vm}}$ $\mathrm{Ca}_{\mathrm{min}}$, & $\mathrm{Ca}_{\mathrm{max}}$	Gaussian Emulation	Built GP emulators that are effective for analysing sensitivity and uncertainty in cardiac models, predicting key differences in how parameter changes affect model outputs.
Aziz and Simitev 2021				
Biktashev et al. 2008 Noble 1962 Luo and Rudy 1991 Courtemanche et al.	Relative Current Strength	APD90	Nelder and Mead 1965 method	Developed a simplified cardiac excitation model that accurately replicates detailed models and experimental data while improving computational efficiency
Lachaud et al. 2022				
Shannon et al. 2004	Relative Current Strength	APD & ΔAPD	Rejection Sampling	Linked Intra-regional variability in rabbit ventricular APs to the heterogeneous contributions of specific ion channels, that was accurately reproduced and analysed using a population of models that match experimental data.

Table 1.2: Studies that addressed and assessed variability in cardiac electrophysiology

Cardiac Model	Uncertain inputs	Outputs	Method	Results
Chapter 3; published in Simitev et al. 2023				
McKean Jr 1970	Relative Current Strength	APD & ΔAPD	Inverting a closed-form expression for APD using fast- slow simple model of electrical excitability	Develops a method to quantify electrophysiological properties of individual cardiomyocytes, enabling accurate predictions of drug effects, including APD changes, cell excitability, and dose-response relationships.
Chapter 4				
Luo and Rudy 1991 Tusscher et al. 2004	Relative Current Strength	$\mathrm{V_{max}}$, APD90, APD30, CaTa, CaT90, CaTrest	OLS Regression Step-wise Regression with nonlinear outputs	Develops a regression model to predicts drug response. Enhances predictive accuracy in cardiac models by including nonlinear relationships between conductances and physiological outputs.
Chapter 5				
Shannon et al. 2004	Relative Current Strength	APD90, APD50, APD30, ΔAPD90 ΔAPD50, ΔAPD30	Rejection Sampling using Gaussian Process Emulators	Builds GP emulators and uses rejection sampling to accurately reproduces variations of APD that match experimental data.

Table 1.3: Chapters of this thesis address and assess variability in cardiac electrophysiology

The study by (Lachaud et al. 2022) investigated the differences in action potential (AP) waveform within a single heart, across various regions of the same heart, and among individual cardiomyocytes. The findings revealed a notable degree of variability in APD, highlighting the complex and heterogeneous nature of cardiac electrophysiology. By comparing intrinsic variability within single hearts to inter-regional and inter-cellular differences, the study emphasises the necessity of accounting for these variations when developing models and treatments for cardiac arrhythmias. Such variability is critical for comprehending the mechanisms that contribute to arrhythmogenic events and has significant implications for the development of personalised and precise therapeutic approaches for treating cardiac conditions. Additionally, the study highlights that APD alone does not uniquely determine the electrophysiological response of myocytes to drugs Additionally, suggesting the need for identifying further independent biomarkers to improve the accuracy of ΔAPD90 estimation.

1.4 Development of Anti-Arrhythmic Drugs

The heart's ability to pump blood is driven by the coordinated contraction of approximately 50 million individual cardiac cells. Each contraction is initiated by the excitation of electrical impulses known as transmembrane action potentials (AP) (Bers 2001). These electrical impulses are crucial for maintaining the rhythmic contractions necessary for effective blood circulation throughout the body.When the duration of these action potentials is altered due to disease, inherited disorders, or environmental factors, the heart becomes susceptible to arrhythmias-electrical instabilities that can quickly lead to a fatal reduction in cardiac output (Anumonwo and Pandit 2015; Tse 2016). The alteration in action potential duration can disrupt the heart's normal rhythm, leading to life-threatening conditions. The strong motivation to develop anti-arrhythmic drugs stems from the need to regulate action potential duration and restore it to normal levels (Darbar 2018). These drugs are designed to prevent or correct arrhythmias by targeting the underlying electrical disturbances within the heart. The APD and its change under drug influence (ΔAPD) are key biomarkers used in the design and evaluation of anti-arrhythmic drugs (Corrias et al. 2010). Monitoring these biomarkers allows researchers to assess the effectiveness of drugs in regulating heart rhythms and preventing arrhythmias. Recent advancements in optics-based techniques within cardiac electrophysiology have enabled

the development of high-throughput systems capable of measuring APD and other secondary AP waveform biomarkers at rates of up to 200 cells per hour (Warren et al. 2010; Lachaud et al. 2018; Müllenbroich et al. 2021). These technological improvements have significantly enhanced the ability to study cardiac electrophysiology, allowing for more precise and efficient drug testing and development.

1.5 Structure of Thesis

This thesis is centered on the analysis of single-cell models of the action potential (AP) and their application in cardiac electrophysiology. The primary objective is to address key challenges in the field by using cardiac action potential models. This thesis employs several distinct mathematical models of cardiomyocytes, including the simplified McKean model (McKean Jr 1970), the Shannon model for rabbit left ventricular (LV) cardiomyocytes (Shannon et al. 2004), the Luo-Rudy model for mammalian ventricular cells (Luo and Rudy 1991), and the ten Tusscher model for human ventricular cells (Tusscher et al. 2004). These models are instrumental in understanding the complex interactions and dynamic behaviour of electrophysiological systems, particularly when dealing with multiple interdependent variables. Unlike experimental methods, mathematical models allow for the manipulation and measurement of variables in ways that are otherwise not feasible. However, it is essential to acknowledge that these models are inherently imperfect representations of actual biological processes. Therefore, verifying that their primary predictions align with experimental data is crucial for ensuring their reliability.

In recent years, statistical techniques have been developed and applied across various scientific disciplines to quantify uncertainty in the parameters that influence model behavior. These techniques provide a range of predictions by accounting for the uncertainty and variability inherent in electrophysiological systems. Parameter uncertainty, often stemming from incomplete understanding, is a significant challenge in cardiac electrophysiology. This thesis aims to explore these challenges by treating key characteristics of cardiac models, such as maximal

conductances, as random variables that follow a probability distribution rather than fixed values. This probabilistic approach allows for the analysis of how variations in these distributions can provide insights into the specific ionic currents that contribute to beat-to-beat variability in action potential models.

This thesis is organised into seven comprehensive chapters, each meticulously designed to guide the reader through the research process and findings. In this section, we will present a detailed outline of the thesis structure, offering a summary of the key topics and concepts explored in each chapter.

Chapters 1 & 2: These are the introductory chapters, Chapter 1 presents a concise overview of cardiac electrophysiology, establishes the research context, explains the motivation behind the research, and clearly defines the aims and research questions for each chapter within the thesis. Chapter 2 builds upon this introduction by offering a more detailed examination of cardiac electrophysiology. It traces the development of action potential models, beginning with the pioneering work of Hodgkin and Huxley (Hodgkin and Huxley 1952), and explores how these models have evolved. The chapter also delves into the fundamental mathematical equations that govern cardiac cellular electrophysiology, detailing the specific roles of various ionic currents in generating action potentials.

Chapter 3: This chapter focuses on addressing a significant gap in cardiac electrophysiology by applying a basic conceptual model of cellular excitability to analyse experimental findings related to ion channel block in a large and heterogeneous population of uncoupled cardiomyocytes. Previous studies, including the work by Lachaud (Lachaud et al. 2022), have primarily involved measuring the shortening of APD in approximately 500 rabbit ventricular myocytes treated with Nifedipine. These cells, collected from various regions of the left ventricles of multiple rabbits, demonstrated notable intrinsic variability in their APD and drug responses. However, despite extensive research in this area, the complex and variable nature of cellular responses has not been fully captured or explained by existing models.

To address this gap, our work in Chapter 3 begins by solving the McKean model (McKean Jr 1970), a simple yet effective representation of the transmembrane action potential (AP). The McKean model is chosen for its simplicity and effectiveness in representing rabbit ventricular APD restitution. It is a fast-slow system of piecewise linear ordinary differential equations (ODEs) similar to the FitzHugh-Nagumo type. This model was selected because its equations incorporate the essential dynamics found in true cardiac AP models, including the traditional Tikhonov slow-time subsystem characteristic of the McKean type. I solved the McKean model during the first year of my PhD. The rest of the chapter is completed in the third year.

Building on the McKean model (McKean Jr 1970), we employ an asymptotic approximation of APD to analyse the ion channel block studies conducted by (Lachaud et al. 2022). In this analysis, we infer the cellular properties of each myocyte based on cell-specific parameter values within the McKean model (McKean Jr 1970). This approach provides a more detailed understanding of how individual variations in cellular properties contribute to the observed variability in APD and drug responses. The analysis of fast-slow systems, such as the McKean model (McKean Jr 1970), is based on rigorous foundations established by traditional theorems from (Tikhonov 1952; Pontryagin 1957; and Fenichel 1979). A comprehensive reference with detailed explanations and a wide range of sources is available in (Kuehn et al. 2015).

It is important to note that there are various alternative versions of the McKean kinetics besides the one we used in Chapter 3, (McKean Jr 1970); they can be found in (Barkley 1991, and Fall et al. 2002). These variants, along with the FitzHugh-Nagumo model, would produce similar results - to the results in Chapter 3 - in terms of their overall characteristics, but they may not be as conveniently expressed as the closed form presented in this chapter. The McKean equations are a suitable phenomenological model for the restitution of the rabbit ventricular APD. This is because realistic cardiac AP models typically have a Tikhonov slow-time subsystem of McKean type, even though the overall model is essentially non-Tikhonov, as shown by (Biktashev et al. 2008).

A critical challenge in studying intrinsic variability is the difficulty in linking action potential waveforms, which originate from ionic currents to the electrophysiological properties of individual myocytes, including ion channel conductances and kinetic parameters (Pandit 2018). Current high-throughput techniques, such as patch-clamping of ionic currents, are not feasible for large numbers of cells (exceeding 100). Additionally, combining these techniques with voltage-sensitive dyes introduces further technical challenges, complicating the accurate measurement of electrophysiological properties across multiple cells.

In (Lachaud et al. 2022) employed a rejection sampling procedure using the detailed ionic (Shannon et al. 2004) model to represent rabbit myocytes. This involved conducting a parameter sensitivity analysis, varying ionic conductances, and generating $50,000$ model variants. These models were then calibrated by rejecting those variants outside the experimental APD90 range. However, these calibrated models were not cell-specific, and the population was not unique. Moreover, many parameters remained at baseline values, limiting the model's adaptability and complicating causal inference (Biktashev et al. 2008).

Given the complexity and limitations of detailed models, Chapter 3 introduces a simplified phenomenological model, specifically the McKean model (McKean Jr 1970), to mathematically describe the experimental procedures used by (Lachaud et al. 2022). Simplified models, like those developed by (Mitchell and Schaeffer 2003; FitzHugh 1961; Nagumo et al. 1962; and Aliev and Panfilov 1996), provide a more manageable approach to understanding cardiac action potentials. The McKean model (McKean Jr 1970), in particular, stands out due to its simplicity, featuring only three intrinsic parameters. It allows for an exact solution of the AP waveform in a closed form. Through phase-space analysis, we derived a simplified asymptotic relationship between APD and the model's parameters, illustrating their geometric behavior. This model was then applied to the experimental data from (Lachaud et al. 2022), enabling us to uniquely determine individualised McKean model parameters for each rabbit myocyte.

Chapter 4: In Chapter 3, we used the McKean model to infer cell-specific parameters based on experimental data, benefiting from its simplicity and analytical approximations. While this approach proved effective for analyzing ion-channel block in a large population of uncoupled cardiomyocytes. This approach becomes less practical when we transition to more complex models, such as the LR1 model (Luo and Rudy 1991). As this model incorporates detailed biophysical properties and multiple ionic currents, it will require computational demands. To address this, Chapter 4 introduces simpler, faster, and more cost-effective regression-based methods that can efficiently analyze conductances and predict outcomes in complex cardiac models like LR1, without compromising accuracy.

This chapter aims to enhance the understanding of sensitivity in computational models of cardiac myocyte electrical activity by introducing a more efficient method for rapidly assessing the impact of parameter changes on model outputs. Traditionally, evaluating model parameters has been a time-consuming process, often requiring significant computational resources. To address this challenge, we develop and test a novel approach that improves the speed and efficiency of parameter assessment. Specifically, this work explores the use of both linear and nonlinear regression models to analyse the relationship between ion channel conductances and physiological outputs, with the goal of enhancing the predictive accuracy of cardiac electrophysiology models.

Computational models in cardiac electrophysiology are extensively used to investigate the mechanisms of arrhythmias and other heart-related phenomena. These models provide valuable insights, generating predictions, guiding experiments, and quantifying complex physiological processes. However, they face significant challenges, particularly in capturing the experimental variability in action potential duration (APD). Previous studies by (Sobie 2009; Sarkar et al. 2012; and Sobie and Sarkar 2011) employed partial least squares (PLS) regression to develop simplified models that link ion channel conductance changes to physiological outputs such as action potentials and calcium transients. While these linear models have been instrumental in the field, they do not fully capture the complex nonlinear relationships between variables, leaving room for further improvement.

Building on this prior work, Chapter 4 introduces both ordinary least squares (OLS) regression and nonlinear regression models to address these limitations. We extend the methodology by applying these models to predict drug responses in the Luo-Rudy model, focusing specifically on the effects of reducing the conductance G_{K} by 30% to simulate ion-channel block, similar to the Dofetilide experiments conducted by (Lachaud et al. 2022). By adjusting the G_{K} values in the model, we were able to calculate new APD90 values after drug application for each cell. This application demonstrates the versatility of our regression techniques, highlighting their utility not only for sensitivity analysis but also for accurately predicting drug-induced changes in computational models of cardiac electrophysiology.

The second study presented in Chapter 4 introduces a novel approach to parameter sensitivity analysis by combining both linear and nonlinear regression techniques. This method offers a more robust framework for understanding the complex relationships between ion channel conductances and physiological outputs. By expanding upon Sobies work, which primarily focused on linear models, we incorporated nonlinear termsspecifically the squares of biomarker valuesinto the analysis. This extension allows for a more comprehensive examination of the correlations between ion channel conductances and action potential characteristics, enhancing the predictive power and accuracy of cardiac models.

To investigate the relationship between ionic conductances and biomarkers, we focused on predicting G_{CaL}, the maximal L-type calcium current permeability, based on six key biomarkers. Regression models were developed that incorporated both linear and nonlinear terms. The inclusion of nonlinear predictors allowed us to account for more complex dependencies between G_{CaL} and the biomarkers. Stepwise regression was applied, starting with a full model consisting of 12 terms6 linear and 6 nonlinearand backward selection was used to refine the model. This process identified the most relevant predictor variables influencing G_{CaL}.

Chapters 5 & 6: In Chapter 4, stepwise regression helped identify key linear and nonlinear relationships between ion channel conductances and biomarkers. However, its limitations in capturing more complex nonlinear interactions became evident, with only 9 out of 16 conductances showing significant nonlinear terms. To address this, Chapter 5 introduces Gaussian Process (GP) regression, a non-parametric and probabilistic framework that adapts to varying dynamics across different data ranges. This method offers a more flexible and robust way of capturing complex nonlinear interactions, making it better suited for modeling the intricate dynamics present in cardiac electrophysiology.

Chapter 5 investigates the variability of action potentials (APs) in a population of rabbit cardiomyocytes under both controlled and drug-induced conditions. The primary goal is to explore the mechanisms responsible for this variability by integrating experimental data with computational modeling techniques. Specifically, this chapter focuses on creating and analyzing a population of models using GP emulators, calibrated to match observed data. This approach offers an efficient and cost-effective alternative to traditional simulation methods for understanding how variability across cells influences drug action.

Previous studies, such as those by Lachaud (Lachaud et al. 2022), utilized detailed ionic current models like the Shannon model to study action potentials in rabbit cardiomyocytes (Shannon et al. 2004). They combined rejection sampling procedures with parameter sensitivity analysis, generating 50,000 model variants. These variants were calibrated by rejecting those that fell outside the experimental APD90 range, allowing for an investigation of the effects of hERG and L-type calcium channel blocks.

Building on this foundation, Chapter 5 employs the same detailed ionic current model but introduces a novel approach using GP emulators instead of traditional simulators. GP emulators provide a faster, more computationally efficient method for generating model populations within the experimental APD90 range, enabling a broader analysis of how cell-to-cell variability affects drug responses, particularly in relation to hERG and L-type calcium channel blocks.

By using GP emulators, the computational cost and time required for generating and analyzing large model populations are significantly reduced. This method offers a scalable solution for exploring the complex interactions between ionic currents and drug effects in cardiac cells. Additionally, it allows for a quantitative comparison between the impacts of drug-induced channel blocks and findings from previous studies, offering new insights into similarities and discrepancies between different modeling approaches.

Chapter 5 introduces GP emulators as an alternative to traditional simulation methods, enabling faster and more efficient generation and analysis of large model populations. This approach is used to explore relationships between ionic conductances, action potentials, and drug effects. The chapter focuses on results related to APD90 with Nifedipine, while Chapter 6 will expand the analysis to additional outputs such as APD50, APD30, and the effects of Dofetilide.

Chapters 7: This chapter serves as the concluding chapter of this thesis, providing a comprehensive summary of our research findings, discussing the strengths and limitations of each chapter, and outlining possible chances for future research.

Chapter 2

Background

2.1 Introduction

This chapter provides the essential mathematical and biological foundations for understanding cardiac function and electrophysiology. It begins with a detailed explanation of the heart's structure and its role as a muscular pump. The chapter then delves into the mechanisms underlying the heart's electrical excitation and the propagation of action potentials (APs). A brief overview is also presented on the evolution of cardiac electrophysiology models, starting from the pioneering model by Hodgkin and Huxley (Hodgkin and Huxley 1952). These models, which characterise the electrical activity of the heart at the cellular level, serve as powerful tools for studying both individual cells and the entire heart, particularly in the context of abnormal cardiac conditions. Additionally, the chapter reviews several experimental techniques used to measure ionic currents and transmembrane potential in cardiomyocytes.

2.2 The Heart Structure

The heart is a muscular organ situated behind the sternum, centrally located in the chest. It consists of four chambers: the right and left ventricles, which are the lower chambers, and the right and left atria, which are the upper chambers. The left atrium and left ventricle together form what is commonly known as the left heart, while the right atrium and right ventricle are collectively referred to as the right heart (Saxton et al. 2023). The four chambers are organised into two pumpsthe right and lefteach responsible for directing blood flow to the pulmonary and systemic circulations, respectively.

The right atrium receives deoxygenated blood from the body, excluding the lungs, via the superior and inferior vena cavae. Additionally, the coronary sinus allows deoxygenated blood from the heart muscle itself to drain into the right atrium. Consequently, the right atrium acts as a reservoir for deoxygenated blood. From the right atrium, the blood flows into the right ventricle, the primary pumping chamber of the right heart, through the tricuspid valve (Mori et al. 2019).

2.2.1 Heart Function

The right ventricle pumps blood to the lungs for oxygenation via the right ventricular outflow tract, the pulmonic valve, and the pulmonary artery. As the blood passes through the capillaries in the lungs, it becomes oxygenated due to its close proximity to the oxygen-rich air in the alveoli. This oxygenated blood is then collected by four pulmonary veins, two from each lung, which empty into the left atrium.

The left atrium serves as a reservoir for oxygenated blood and, similar to the right atrium, transfers blood to its corresponding ventricle through both active and passive mechanisms. Consequently, the left ventricle fills with oxygenated blood as it passes through the mitral valve. The left ventricle, the main pumping chamber of the left heart, then propels the oxygen-rich blood into the systemic circulation through the aortic valve.

This cycle is repeated with each heartbeat. The primary function of the four cardiac valvesthe tricuspid, pulmonic, mitral, and aortic valvesis to ensure the unidirectional flow of blood, preventing any backflow. Figure 2.1 illustrates the internal anatomy of the heart, including these essential valves.

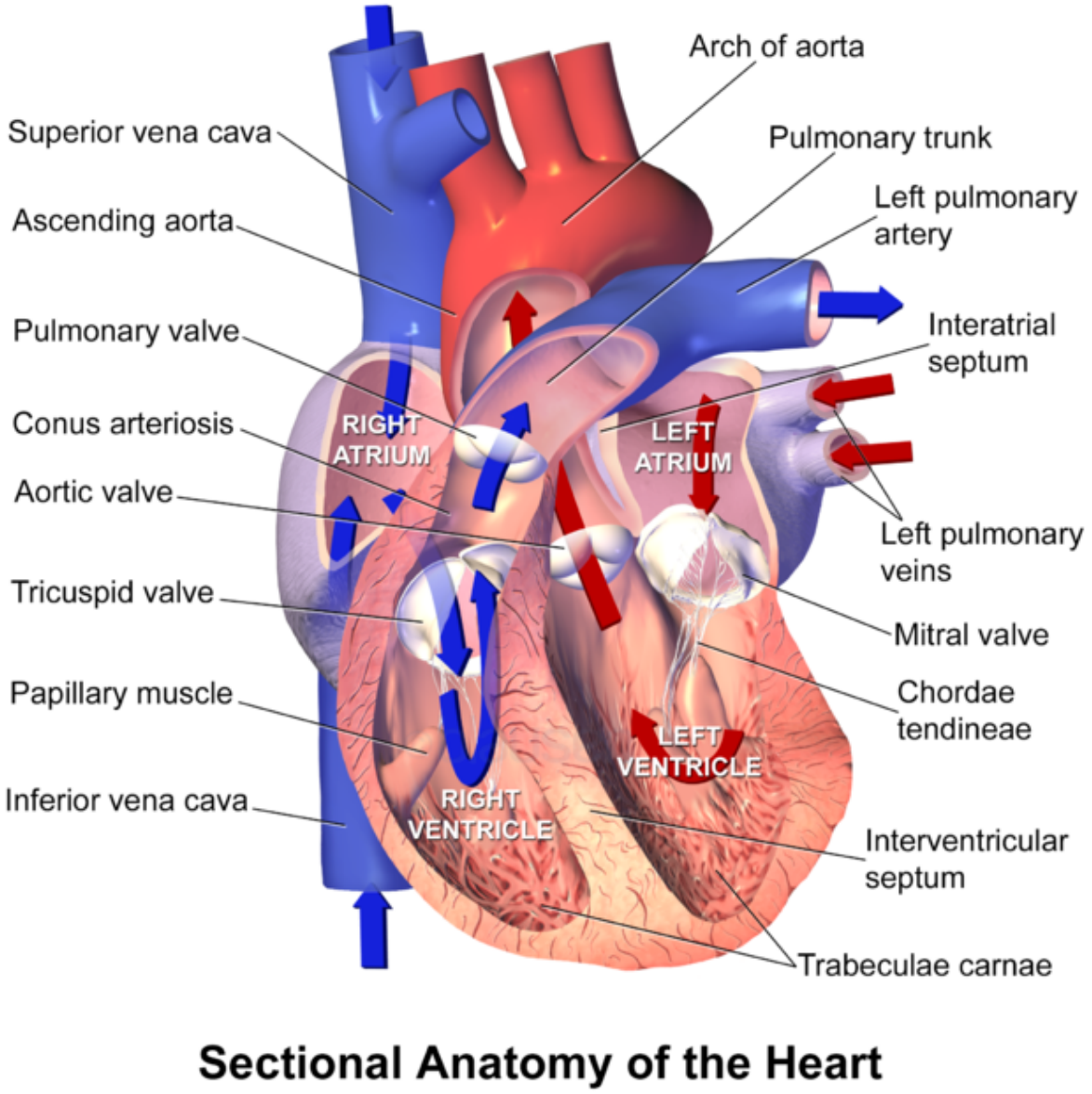

Figure 2.1: Sectional anatomy of the heart showing the four cardiac chambers (right atrium, left atrium, right ventricle, left ventricle), the major blood vessels, and the key valves (tricuspid, pulmonary, mitral, and aortic valves) responsible for ensuring unidirectional blood flow. Figure is from (Wikimedia Commons contributors 2024a)

2.2.2 Cardiac Conduction System

The heart functions as a pump that circulates blood throughout the entire body. Electrical signals propagate down the conduction pathway of the heart with each beating. The process begins when the sinoatrial (SA) node generates an excitation signal. Simply put, this excitation signal undergoes four stages: initially, it is directed to the atria, where it goes through contraction. The signal is then delayed by the atrioventricular (AV) node until the atria are empty of blood. This signal is then transmitted to the Purkinje fibers by the bundle of His, which is the central bundle of nerve fibers. The Purkinje fibers transport it to the ventricles, which are the lower cardiac chambers, where it causes their contraction (Padala et al. 2021). Each of these stages constitutes a complete contraction of the heart muscle. To ensure that the heart continues to pulse, the heart conduction system sends thousands of signals each day. A diagram of the cardiac conduction system is shown in Figure 2.2, which illustrates the entire path of the excitation signal.

The heart functions as a pump that circulates blood throughout the entire body, and this action is driven by electrical signals that propagate through the heart's conduction pathway with each heartbeat. The process begins when the sinoatrial (SA) node generates an excitation signal. This signal then undergoes four key stages (Padala et al. 2021), outlined below:

- Atrial Contraction: The excitation signal is first directed to the atria, causing them to contract.
- Atrioventricular Node Delay: The signal is delayed by the atrioventricular (AV) node, allowing the atria to fully empty their blood into the ventricles.
- Transmission via the Bundle of His: The signal is then transmitted through the bundle of His, the central bundle of nerve fibres, to the Purkinje fibres.
- Ventricular Contraction: The Purkinje fibres carry the signal to the ventricles, the heart's lower chambers, triggering their contraction.

These stages together result in a complete contraction of the heart muscle (Padala et al. 2021). To maintain the heart's continuous rhythm, the heart's conduction system sends thousands of signals each day. A diagram of the cardiac conduction system, shown in Figure 2.2, illustrates the entire path of the excitation signal.

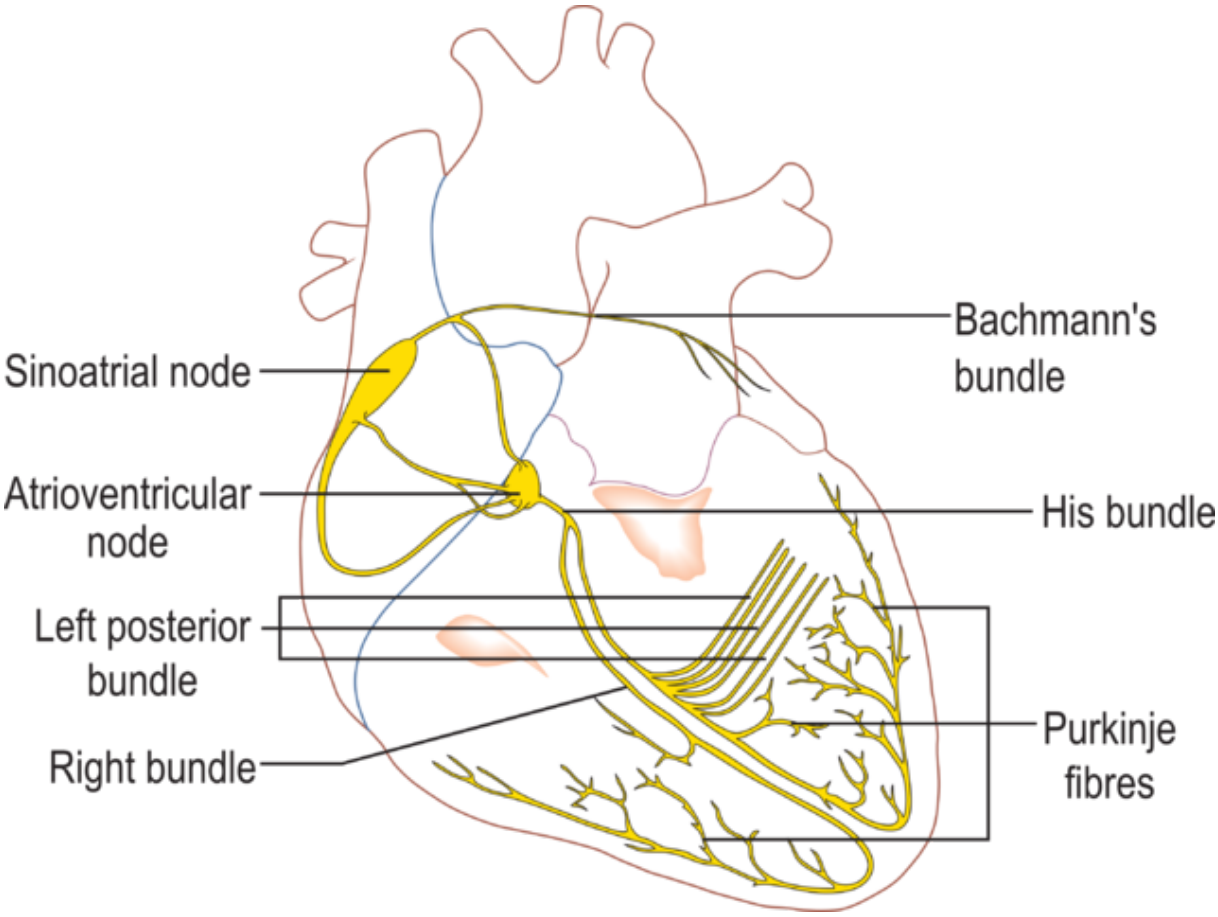

Figure 2.2: Diagram of the cardiac conduction system, illustrating the flow of electrical impulses through the heart, starting from the sinoatrial (SA) node, passing through the atrioventricular (AV) node, and propagating via the bundle of His, right and left bundle branches, and Purkinje fibers to coordinate the contraction of the heart muscle. Figure is from (Wikimedia Commons contributors 2024b)

2.3 Cardiac Electrophysiology

The heart is an incredibly sophisticated organ. Every one of the roughly 3 billion heartbeats that occur in an average person's life necessitates the coordinated contraction of billions of cardiac muscle cells, known as cardiomyocytes. This synchronised contraction is crucial for the rhythmic pumping of blood, which is essential for sustaining life. The coordination of this action is directed by a complex electrical system.

The complicated nature of the cardiac electrophysiology system involves dynamic changes in multiple components across various spatial and temporal scales. However, the quantitative nature of cardiac electrophysiology, governed by physical laws and biological principles, can be accurately measured in patients using non-invasive methods. This characteristic makes it well-suited for computational modelling approaches that are based on mechanistic principles and data analysis.

Computational models of cardiac electrophysiology provide individual parameters with precise control, and their replicability enables a comprehensive assessment of cardiac arrhythmia functions. In recent decades, there has been an increasing interest in the use of computer modelling for mechanistic investigations of cardiac electrophysiology (Trayanova et al. 2023). The computational modelling of cardiac electrophysiology has made substantial progress over the past seven decades, resulting in the establishment of recognised methodologies and an expanding collection of practical applications.

2.3.1 Cardiac Action Potential

The cardiac AP refers to a change in the electrical potential across the cell membrane, typically ranging from 60 to 120 mV. This process begins from a negative value known as the resting membrane potential (RMP) in functional cardiac cells, which varies between -95 and -40 mV (András et al. 2021). The RMP in excitable cells is primarily determined by the conductance of inwardly rectifying K^+ currents and can be approximately calculated using the Nernst equation, accounting for the uneven distribution of K^+ ions across the cell membrane. The electrogenic ATP-dependent Na^+-K^+ pump also plays a crucial role in maintaining the RMP by exporting 3 Na^+ ions and importing 2 K^+ ions (Lee 1996). Under normal conditions, the APD determines the effective refractory period (ERP), which is the minimum amount of time required before a new stimulus can trigger another AP. However, under pathological conditions, such as hyperkalaemia, the relationship between APD and ERP can be disrupted, leading to post-repolarisation refractoriness (Shaw and Rudy 1997). When discussing the cardiac AP, it is important to consider two key aspects:

- **Variability Across Different Heart Regions:** The term cardiac AP does not refer to a uniform structure, as the shape and characteristics of the transmembrane potential changes vary significantly across different regions of the heart, as illustrated in Figure 1.1 in previous chapter. Therefore, it is essential to study and describe individual APs in a region-specific manner.

- **Species-Specific Differences:** There are also significant variations in cardiac APs between different species, even when measured from comparable regions of the heart(Britton et al. 2013). This issue is particularly important, as many experimental findings have been obtained from studies conducted on various species, yet this variability is often overlooked.

2.3.2 Phases of the Ventricular Action Potential

The ventricular AP is typically categorised into five distinct phases, each playing a crucial role in the cardiac cycle. Figure 2.3 illustrates the AP of ventricular cardiomyocytes, highlighting the sequential progression through these phases. Below is a brief summary of each phase:

- **Phase 0: Upstroke** Phase 0 is characterised by rapid depolarisation, where the membrane potential shifts into a positive voltage range within approximately 2 ms. This phase is crucial for the swift propagation of the cardiac AP. The rapid upstroke is driven by the activation of the fast sodium current ($\mathrm{I_{Na}}$), which significantly increases the membrane conductance of $\mathrm{Na^+}$. This results in a rapid positive shift in voltage across the cell membrane, reaching a threshold value of around -70 mV and further increasing to approximately $+40$ mV. If the initial stimulus is insufficient to reach the threshold potential, the fast sodium channels will not activate, and no AP will be generated (Sakakibara et al. 1993).

- **Phase 1: Initial Repolarisation** Phase 1 involves a rapid partial repolarisation of the membrane. This phase sets the stage for the subsequent plateau phase. It begins with the rapid inactivation of the $\mathrm{Na^+}$ channels, while transient outward potassium channels (I_{to}) open and close quickly, allowing potassium ions to leave the cell. This phase appears as a notch on the AP waveform (Benitah et al. 2010).

- **Phase 2: Plateau** Phase 2 is characterised by a stable, prolonged plateau, making it the longest phase of the AP. It is unique to cardiac cells and marks the entry of calcium ions (Ca^{2+}) into the cell. During this phase, the repolarisation slows down due to the inward flow of Ca^{2+}, counterbalanced by the outward movement of potassium ions through the I_{Ks} current. The membrane potential remains depolarised and relatively constant during this prolonged phase.

- **Phase 3: Final Repolarisation** Phase 3 involves rapid repolarisation, which restores the membrane potential to its resting value. During this phase, the L-type Ca^{2+} channels close, while the potassium channels from Phase 2 remain open. Additional potassium channels, including I_{Kur}, I_{Kr}, and I_{Ks}, contribute to the outward currents that play major roles in controlling repolarisation. The slow deactivation of these channels ensures that they continue to contribute to the outward current throughout Phase 3, allowing the membrane potential to return to its resting level (Grant 2009a).

- **Phase 4 : Resting Potential** Phase 4 marks the end of the action potential. In standard non-pacemaker cells, the membrane potential during this phase is relatively stable, typically around -90 mV. The resting membrane potential is the result of a balance between the influx of ions like Na^{+} and Ca^{2+}, and the efflux of K^{+}, regulated by various membrane pumps. During Phase 4, the membrane potential is slightly depolarised (between -50 to -65 mV) and undergoes slow diastolic depolarisation, eventually leading into Phase 0 (Dhamoon and Jalife 2005).

2.3.3 Transmembrane Ion Channels and Transporters in the Heart

The cardiac AP represents the change in voltage across the cell membrane, driven by the movement of ions through ion channels. These ion channels open and close in a dynamic and coordinated manner, facilitating the propagation of electrical signals within the heart (Grant 2009b). A significant advancement in the study of cardiac electrophysiology was the development of the patch-clamp technique, which is widely used to quantify transmembrane ionic currents in the heart. This technique is particularly effective in studying isolated myocytes, allowing for the precise recording and analysis of individual ionic currents passing through single ion channels, as well as the collective currents across the entire sarcolemma.

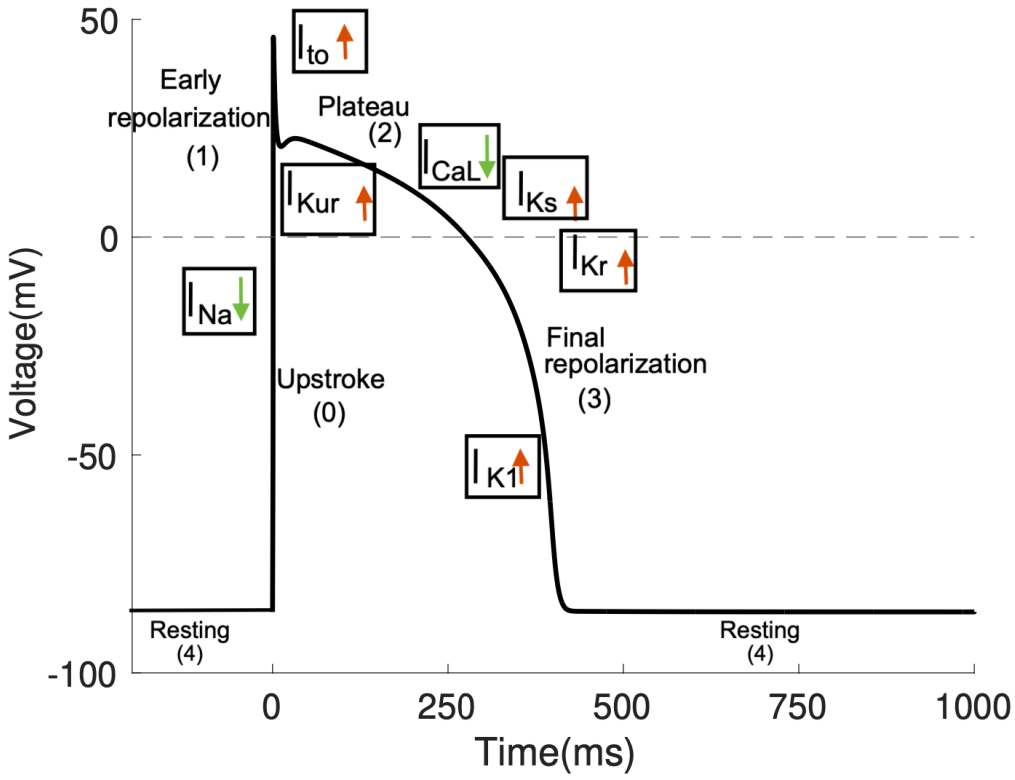

Figure 2.3: The arrows in the figure represent ionic currents: upward arrows indicate outward currents (leaving the cell), while downward arrows indicate inward currents (entering the cell). This figure illustrates the five distinct phases of the ventricular cardiomyocyte action potential (AP) and the ionic currents contributing to each phase. During Phase 0 (Upstroke), the rapid depolarization is driven by I_{Na} (downward arrow), indicating a large inward sodium ion flow that causes a rapid positive shift in membrane potential. In Phase 1 (Initial Repolarization), I_{to} (upward arrow) and I_{Kur} (upward arrow) facilitate partial repolarization by allowing potassium ions to leave the cell. Phase 2 (Plateau) is maintained by I_{CaL} (downward arrow), representing inward calcium ion flow, while I_{Ks} (upward arrow) provides outward potassium ion flow, balancing the inward calcium current and maintaining the plateau. During Phase 3 (Final Repolarization), I_{Kr} (upward arrow) accelerates the outward flow of potassium ions to drive rapid repolarization, and I_{K1} (upward arrow) contributes toward the end of repolarization to restore the membrane potential to its resting state. Finally, in Phase 4 (Resting Potential), I_{K1} (upward arrow) maintains the stable resting membrane potential by counterbalancing small inward sodium and calcium ion leaks.

Before the use of the patch-clamp technique, recordings of transmembrane currents were less accurate due to inadequate voltage control of the sample. Moreover, the precise determination of rapid current changes and gating kinetics was challenging and often unattainable (Banyasz et al. 2011).Table 2.1 summarises the various transmembrane ion channels and their roles in the generation of the cardiac AP. Readers are encouraged to refer to the publication by (András et al. 2021) for a more detailed and comprehensive understanding of the different transmembrane ion channels in cardiac cells.

Current	Description	AP Phase	Activation Mechanism
I_{Na}	Fast Inward Sodium	Phase 0	Voltage, depolarisation
Ito,f	Transient Outward, fast	Phase 1	Voltage, depolarisation
Ito,s	Transient Outward, slow	Phase 1	Voltage, depolarisation
I_{Kur}	Ultrarapid Delayed Rectifier	Phase 1 & 2	Voltage, depolarisation
$I_{\mathrm{Ca,L}}$	Calcium, L-type	Phase 2	Voltage, depolarisation
I_{Kr}	Rapid Delayed-rectifying Potassium	Phase 3	Voltage, depolarisation
I_{Ks}	Slow Delayed-rectifying Potassium	Phase 3	Voltage, depolarisation
I_{K1}	Inward Rectifier Potassium	Phase 3 & 4	Voltage, depolarisation

Table 2.1: This table contains the membrane ion currents responsible for generating the action potential (AP).

2.4 Computational Modelling of Cardiac Action Potentials

The extensive range of experimental data characterising the structure and function of myocytes has enabled the development of sophisticated electrophysiological models. These models can accurately simulate APs and conduction properties across various species, including humans. Over the past 70 years, significant progress has been made in modelling and replicating the electrophysiology of the heart.

Computational models offer complete observability and controllability in simulations, allowing researchers to overcome the limitations inherent in experimental models. These models provide predictions grounded in a deep understanding of underlying systems, and these predictions can be readily tested. By guiding further research and connecting to existing knowledge of physiological mechanisms, computational models play a critical role in advancing the field.

Furthermore, when simulations fail to replicate a specific phenomenon, it highlights potential gaps in current knowledge or contradictions within the field. This presents an opportunity to uncover essential elements or mechanisms that may not be represented in the model but are crucial for understanding specific events in living cells. A computer model of cardiac cellular electrophysiology typically includes a set of differential equations that describe the processes of transmembrane ionic transport and excitation-contraction coupling. The primary modelling frameworks used are outlined below (András et al. 2021):

2.4.1 Hodgkin-Huxley Models

The Hodgkin-Huxley framework is one of the most commonly employed approaches for modeling ionic currents in excitable cells like neurons and cardiac cells. The objective of a Hodgkin-Huxley model is to replicate the biophysical characteristics of ion channels, as determined through patch-clamp experiments.

The membrane voltage V_M is represented by Equation (2.1), which simulates the cardiac action potential (AP) as the product of the inverse of membrane capacitance (C_M) and the sum of all ionic currents $\sum_{\mathrm{X}} \mathrm{I_X}$, where each $I_{X(t)}$ represents the current for a specific ion channel X.

Equation (2.2) shows the three major components determining the magnitude of an ion current I_X. This includes the open probability P_{open}, which refers to the likelihood that an individual ion channel is in an open state at any given time, allowing ions to flow through it. This probability is governed by a set of independent "gates" (e.g., activation and inactivation gates) that follow ordinary differential equations (ODEs) controlled by the membrane voltage (V_M). The combined states of these gates determine the proportion of open channels. Subsequently, the open channel conductance and the ionic driving force across the channel are used to compute the total current (Hodgkin and Huxley 1952). The driving force reflects the electrochemical gradient that drives ion movement across the membrane.

$$\frac{dV_M}{dt} = -\frac{1}{C_M} \sum_{\mathrm{X}} \mathrm{I_X(t)}, \tag{2.1}$$

where:

$$I_{X(t)} = (\text{ Conductance }_X) \cdot (\text{ Open Probability }_X) \cdot (\text{ Driving Force }_X). \tag{2.2}$$

The open probability of a channel depends on the states of its gates, which are governed by probabilities that evolve over time. For example, if a channel requires three activation gates to be open to conduct ions, the open probability can be expressed as:

$$P_{\text{open}} = m^3 \cdot h, \tag{2.3}$$

where m represents the probability that an activation gate is open, and h represents the probability that the inactivation gate is not inactivated. These probabilities change over time according to ordinary differential equations (ODEs) driven by the membrane voltage (V_M). The equation for the driving force is:

$$\text{Driving Force}_{X} = (V_M - E_X), \tag{2.4}$$

where: V_M is the membrane potential, and E_X is the Nernst or reversal potential for the ion X.

However, the Hodgkin-Huxley model has limitations, particularly in its inability to include state-dependent effects, such as drug binding that occurs only when a channel is in an open state. In such cases, Markov models provide a more suitable approach.

2.4.2 Markov Models

Markov models can be considered an extension of Hodgkin-Huxley models, enabling them to effectively capture complex structures because they represent the probabilities of state transitions as time-evolving variables. These transitions depend on the present state of the channel and are influenced by factors such as membrane voltage or drug interactions. When Hodgkin-Huxley cannot be used, Markov models are often employed in such scenarios, as they can express different states of a channel (such as open, closed, inactivated by voltage, or inactivated by drugs) along with the probability of transitioning between these states (Mahajan et al. 2008). The transitions between states depend on state variables, such as the membrane voltage V_M r other modulating factors.

In a Markov model, a channel can transition between multiple states, such as:

$$C_X \underset{k_{\beta_X}}{\overset{k_{\alpha_X}}{\rightleftharpoons}} O_X \underset{k_{\beta_B}}{\overset{k_{\alpha_B}}{\rightleftharpoons}} B_X \tag{2.5}$$

where:

- C_X : Closed state of the channel,
- O_X : Open state of the channel,
- B_X : Blocked or inactivated state,
- k_{α_X} and k_{β_X} : Forward and backward transition rates between closed and open states, and
- k_{α_B} and k_{β_B} : Transition rates between open and blocked/inactivated states.

The probability of the channel being in a particular state evolves over time, rather than the physical gates themselves following ODEs. These probabilities are driven by the transitions between states, which depend on factors such as membrane voltage V_M. For the open state (O_X):

$$\frac{dO_X}{dt} = k_{\alpha_X} C_X - k_{\beta_X} O_X - k_{\alpha_B} O_X + k_{\beta_B} B_X \tag{2.6}$$

The equation describes the dynamics of the open state (O_X) probability by accounting for various transitions: the influx from the closed state (C_X) at a rate of $k_{\alpha_X} C_X$; the efflux back to the closed state at a rate of $k_{\beta_X} O_X$; and the transitions between the open state and the blocked state (B_X), with $k_{\alpha_B} O_X$ representing the rate from open to blocked, and $k_{\beta_B} B_X$ from blocked to open.

The overall open probability (P_{open}) is the sum of probabilities of all states considered “open”, such as O_X. The total ionic current through the channel I_X is then calculated as:

$$I_X = P_{\text{open}} \cdot g_X \cdot (V_M - E_X) \tag{2.7}$$

where:

- g_X : Single-channel conductance.
- V_M : Membrane potential.
- E_X : Reversal potential of the ion.

Markov models are beneficial for accurately representing state-dependent drug binding, where a drug binds only when the channel is in the open state. However, this increased flexibility also introduces challenges in terms of model identification and parameter estimation (Trayanova et al. 2023).

2.5 A Brief History of Cardiac Electrophysiology Models

Mathematical modelling has proven to be a powerful tool for understanding complex biological systems. The study of excitable cellular membranes, particularly in cardiomyocytes, has become increasingly popular for in-depth mathematical modelling due to the intricate and dynamic nature of these systems. Cardiomyocyte physiology is a highly complex biological system, characterised by numerous interacting components that behave in a non-linear manner. The activity of each ion channel, pump, and transporter dynamically changes over time in response to rapidly shifting environmental conditions. Cardiac cell models are constructed based on extensive experimental data obtained from various preparations using techniques such as whole-cell and single-channel patch clamps. This data helps with the design of the model structure, determines the parameters of the model components, and validates the model’s accuracy (Fink et al. 2011).

Mathematical models of the heart exist on various spatial scales, from the subcellular cardiac dyad to the entire heart. This study focuses on mathematical models representing a single, isolated cardiomyocyte. Typically, a single model is assumed to be representative of an entire cell type, although it may not fully capture the behavioural variation within individual cells. These models are mathematical representations of the electrical events in the cell that produce APs. They often involve numerous ordinary differential equations (ODEs) that represent state variables such as membrane voltage, ion concentrations in subcellular regions, ion channel dynamics, and the various states of ion channels. As models become more complex, it becomes increasingly challenging to accurately constrain every parameter, which can lead to greater overall inaccuracy and errors in the system. Therefore, experimental tests of key model predictions are crucial; they help validate the model and ensure that the parameters are set appropriately, thereby improving the models accuracy and reliability. Voltage and gating kinetics can be quantified by fitting the equations of the mathematical model to experimental patch clamp recordings of the relevant current. This close calibration between ion channel formulations and experimental data results in a high degree of validity between simulation and experiment.

The first mathematical model for AP was the groundbreaking work on electrical activity in the squid giant axon proposed by (Hodgkin and Huxley 1952). This was a significant breakthrough in the computational modelling of electrophysiology. The current equation is:

$$C_m \frac{dV_m}{dt} = I_{\text{ext}} - (I_{\text{Na}} + I_{\text{K}} + I_{\text{L}}), \tag{2.8}$$

where

- V_m is the membrane potential,
- I_{ext} is the external current applied to the membrane, and
- $I_{\text{Na}}, I_{\text{K}}$, and I_{L} are the sodium, potassium, and leakage currents, respectively.

The Ionic currents are defined as:

$$I_{\mathrm{Na}} = g_{\mathrm{Na}} m^3 h \left(V_m - E_{\mathrm{Na}}\right),$$
$$I_{\mathrm{K}} = g_{\mathrm{K}} n^4 \left(V_m - E_{\mathrm{K}}\right),$$
$$I_{\mathrm{L}} = g_{\mathrm{L}} \left(V_m - E_{\mathrm{L}}\right),$$

where:

- g_{Na} and g_{K} are the maximal conductances for sodium and potassium, respectively,
- $E_{\mathrm{Na}}, E_{\mathrm{K}}$, and E_{L} are the equilibrium potentials for sodium, potassium, and leakage ions, respectively.

The gating variable equations are defined as follow:

$$\frac{dm}{dt} = \alpha_m(1-m) - \beta_m m,$$
$$\frac{dh}{dt} = \alpha_h(1-h) - \beta_h h,$$
$$\frac{dn}{dt} = \alpha_n(1-n) - \beta_n n,$$

where α and β are rate constants that depend on the membrane potential and govern the opening and closing of the ion channels.

Given the similarities between neuronal and cardiac excitable properties, the Hodgkin-Huxley (HH) current equations (2.8) have served as the foundation for computational cardiac electrophysiology. As a result, numerous mathematical models of cardiac electrophysiology have been developed, each aimed at addressing specific research questions. One modification of the (HH) current equations (2.8) is the work by (FitzHugh 1961), who developed simplified equations to simulate excitation and propagation. Modern models are often divided into distinct subcellular compartments, and subsequent studies have provided models for specific cardiac regions (e.g., ventricular cardiomyocytes, Purkinje fibres, atrial cardiomyocytes) across different animal species (e.g., mouse, guinea pig, rabbit, dog). For a detailed overview of the most well-known and advanced mathematical models in cardiac electrophysiology, refer to (Fenton and Cherry 2008).

2.5.1 Ventricular Models

Due to the clinical importance of ventricular fibrillation, the study of computational cardiac electrophysiology has primarily focused on ventricular cardiomyocytes. A significant breakthrough in ventricular modelling was the development of the Luo-Rudy model for a guinea pig cell (Luo and Rudy 1994). Another highly influential model is the Shannon rabbit model (Shannon et al. 2004). This model effectively separates the various components of the delayed rectifier current and incorporates the junctional subspace, with a particular emphasis on the precise description of calcium handling. The model was later modified by (Mahajan et al. 2008) to optimise its rate-dependent characteristics, and it has been used to investigate alternans.

Modelling and simulating the electrical activity of the human ventricles are critical aspects of computational cardiac electrophysiology. A primary distinction between humans and other animals is the significant dependence of human cardiomyocytes on IKr for repolarisation, unlike in other species (Jost et al. 2013). The first widely recognised models for human ventricular activity were developed by (Tusscher et al. 2004, and 2006). The O'Hara et al. (ORd) model (O'Hara et al. 2011) is now considered the most prominent human ventricular model. This model was developed and tested using a diverse set of experimental data, some of which were specifically collected for the purpose of developing the model.

2.5.2 Atrial Models

Research on modelling and simulating human atrial electrophysiology has become a popular and important topic. Two well-known models of human atrial electrophysiology were developed by (Courtemanche et al. 1998) and (Nygren et al. 1998). Both models accurately reproduce the unique AP shape of atrial myocytes. For a more extensive review of atrial modelling and simulation, readers are encouraged to consult (Wilhelms et al. 2013). These models are based on experimental data from explanted hearts or samples from open heart surgery patients. They have provided significant insights into the mechanisms underlying cardiac arrhythmias under various conditions and have been used for both clinical and commercial applications (e.g., Koivumäki et al. 2011 and Bai et al. 2018).

2.5.3 Purkinje Cell Models

While Noble's early work (Noble 1962) focused on Purkinje fibre cells in the initial cardiac electrophysiological models, advancements in this area have been inconsistent. However, there has been an increased interest in Purkinje fibres, leading to the development of models that specifically examine their function and alterations in heart failure, the electrophysiological foundation of rabbit Purkinje fibres, and the role of Purkinje fibres in the development of arrhythmias (McAllister et al. 1975, and Di Francesco and Noble 1985). A recent development in this field is the Purkinje model by Trovato et al. (Trovato et al. 2020), which includes a thorough calibration using human data under various conditions. This model provides valuable insights into Purkinje cells early after-depolarisations (EADs).

2.6 Applications of Cardiac Electrophysiology Models

Mathematical models that accurately represent the physical properties of the heart have been developed to simulate its functioning at various levels, ranging from individual cells to the entire organ. These models provide critical insights into the underlying mechanisms of complex heart diseases and help in understanding clinical observations, ultimately contributing to improved patient therapy. Below, several applications of these computational models in cardiac electrophysiology are outlined.

2.6.1 Understanding Mechanisms of Normal Heart Rhythm and Arrhythmias

Cardiac electrophysiology models have greatly enhanced our understanding of both normal cardiac function and the mechanisms underlying arrhythmias. These computational models are frequently used to investigate the specific impact of individual ion currents on various cardiac mechanisms (Odening et al. 2021). For example, simulations at the cellular level have shed light on the development of proarrhythmic events such as alternans and early afterdepolarisations (EADs). Early modelling work suggested that the reactivation of $I_{\mathrm{Ca,L}}$ contributes to the formation of EADs, while $I_{\mathrm{K,r}}$ plays a significant role in the rate dependency of these events (Zeng and Rudy 1995). Furthermore, populations of ionic models can be employed to explore the relative contributions of individual ionic currents to specific mechanisms. For in-

stance, this approach was used to study atrial fibrillation (AF), where all AF model populations exhibited consistent changes in $I_{\mathrm{K,1}}$, $I_{\mathrm{K,ur}}$, and I_{to} (Sánchez et al. 2014). Subsequent analyses revealed that variability in APD90 is primarily influenced by inter-subject variability in $I_{\mathrm{K,1}}$ and $I_{\mathrm{Na,K}}$, while variability in APD50 and APD20 is determined by a combination of factors, including $I_{\mathrm{K,ur}}$, $I_{\mathrm{Ca,L}}$, and I_{to}.

2.6.2 Estimating Proarrhythmic Risks of Ion-Channel Mutations

Another important application of cardiac cellular electrophysiology models is in predicting the proarrhythmic effects of ion-channel mutations. Patch-clamp experiments alone cannot fully elucidate how changes in ion channels affect APs or cellular proarrhythmia biomarkers. Computational modelling bridges this gap by linking biophysical changes at the ion-channel level to alterations in AP characteristics, thereby identifying potential triggers for abnormal heart rhythms (Trayanova et al. 2023). For example, in the study by (Miller et al. 2023), electrophysiological alterations associated with long QT syndrome type-3 (LQTS3) mutations were implemented in 1,000 models with varying baseline electrophysiological parameters. The study found that while some models did not exhibit a phenotype with any of the mutations, others displayed a long QT phenotype with one, two, or all three mutations, depending on their baseline characteristics. Notably, models with increased $I_{\mathrm{K,s}}$ or $I_{\mathrm{K,1}}$ were less affected by the mutations.

2.6.3 Cardiac Antiarrhythmic Pharmacotherapy

Antiarrhythmic drugs (AADs) remain a cornerstone of therapy for patients with arrhythmias, particularly atrial fibrillation (AF). However, the effectiveness of currently available AADs is limited, and they are often associated with proarrhythmic side effects (Crumb Jr et al. 2016). Drug-induced proarrhythmia is a significant limitation in the clinical use of these medications (Heijman et al. 2021), highlighting the need for safer and more effective AADs. Cardiac cellular electrophysiology models have become valuable tools in studying the effects of AADs and evaluating the potential antiarrhythmic properties of new drugs. Initially, the suppressive effects of AADs on ion channels were simulated by reducing the maximum ion flow. This approach

provides insights into the general electrophysiological consequences of targeting multiple ion channels. For instance, it can reveal the combined antiarrhythmic effects of targeting various K^+ channels at different pacing rates, using experimentally calibrated populations of virtual human atrial myocyte models (Ni et al. 2020).

In summary, cardiac electrophysiology models are powerful tools for understanding the intricate mechanisms of heart function and disease, predicting the impact of genetic mutations, and guiding the development of safer and more effective drug treatments.

Chapter 3

Phenomenological analysis of simple ion channel block in large populations of uncoupled cardiomyocytes

The results presented in this chapter have been published in (Simitev et al. 2023). This chapter follows the published paper and includes figures from the paper with the agreement of all authors.

3.1 Introduction

Traditionally, the understanding of arrhythmia mechanisms and the development of anti-arrhythmic drug therapies have been based on the assumption that myocytes, or heart muscle cells, from the same region of a single heart exhibit similar, if not identical, action potential waveforms and responses to drugs. However, recent studies have challenged this assumption, revealing significant variability in the electrical behaviour of uncoupled healthy myocytes, not only between different hearts but also within the same region of a single heart (Muszkiewicz et al. 2016).

In this chapter, I present a novel methodology for quantifying the unique electrophysiological characteristics of large populations of uncoupled cardiomyocytes, particularly under conditions where ion channels are blocked. This method utilises a fast-slow conceptual model of electrical excitability, with the model parameters reflecting the distinct properties of each cell. The approach is applied to a dataset comprising nearly 500 rabbit ventricular myocytes, where the action potential duration (APD) was experimentally measured both before and after the administration of the drug Nifedipine (Lachaud et al. 2022).

Within this chapter, the effect of the drug is modelled by a multiplicative factor that modifies the effective ion conductance. An asymptotic expression for APD is derived, allowing for the inversion of this formula to extract model parameters as functions of both APD and the drug-induced change in APD (ΔAPD) for each myocyte. Additionally, the methodology involves calibrating two protocol-related quantities; basic cycle length and drug dose.

The resulting explicit APD expression, along with the corresponding set of model parameters, enables a range of critical predictions and analyses. First, it allows for a detailed evaluation of the specific conditions necessary to maintain a consistent APD or ΔAPD. It also provides insights into the proportion of cells likely to remain excitable following drug application, thereby contributing to a deeper understanding of cellular responses to drug treatments. Furthermore, this approach facilitates the prediction of how variations in the stimulus period might influence the overall response of the cardiomyocytes, offering a deep understanding about dynamic changes in cellular excitability. Finally, it enables the prediction of dose-response curves, which are validated against additional experimental data. This comprehensive approach provides a powerful tool for advancing the understanding of drug effects on cardiac cells.

In this chapter, I will start by describing the experimental data used in the research. Following this, I will detail the steps involved in solving the McKean model and deriving the asymptotic approximation of the action potential duration, which will be applied to the experimental data. Next, I will calibrate the basic cycle length and drug dosage. Finally, I will explore the interrelationships of the parameters in the McKean model and the experimental data.

3.1.1 Experimental Data and Modelling of Drug Action on Cardiac Cells

In this chapter, I present and analyse the experimental data used to develop and validate a model of drug action on cardiac cells. The ion-channel block experiments conducted by (Lachaud et al. 2022) form the basis of this analysis, where the action potential (AP) characteristics of nearly 500 uncoupled cardiomyocytes were measured using voltage-sensitive fluorescent dyes. These cells were carefully isolated from specific regions of the left ventricular walls of 12 rabbit hearts, including apical, basal and endo, mid, and epicardial sub-regions, to create a large and diverse population of myocytes. Following isolation, the cells were loaded with voltage-sensitive dyes to facilitate precise measurement of their electrical activity.

The experiment commenced with the application of a periodic excitation stimulus at a basic cycle length of 500 milliseconds, corresponding to a stimulation frequency of 2 Hz. Action potential duration at 90% repolarisation (APD90) was measured for each cell under these baseline conditions. The results revealed unexpectedly large variability in APD90 values among the healthy cardiomyocytes, with an interquartile range of 40 to 50 milliseconds and a median value of 250 milliseconds (ms). This variability was significantly greater than the regional differences in APD90 observed within single hearts and exceeded the differences between individual hearts. Importantly, this variation was determined not to be caused by damage from the cell dissociation process.

In the subsequent step of the experiment, specific ion channel inhibitors were introduced to observe their effects on APD90. The IKr ionic current was inhibited using 30 nM of Dofetilide, and the ICa(L) current was blocked with $1\mu\mathrm{M}$ of Nifedipine. Following the administration of these drugs, APD90 was measured again. It was observed that cells with nearly identical

baseline APD90 values exhibited a wide range of changes in APD90 (ΔAPD90) after drug application. This result demonstrated that APD alone does not adequately characterise or predict the electrophysiological response of myocytes to drug treatment, challenging common assumptions. The study aimed to interpret these findings using a conceptual mathematical model to gain a better understanding of the underlying mechanisms. Detailed descriptions of the experimental methods, quality control procedures, statistical analyses, and experimental datasets are provided in (Lachaud et al. 2022).

3.1.1.1 The experimental protocol

The experimental protocol for isolating and analyzing rabbit cardiomyocytes is found in (Lachaud et al. 2022), we briefly list the main details as follows:

- Animal Preparation:
  - Species: Male New Zealand White rabbits weighing between 2 and 2.5 kg.
  - Pre-treatment: Intravenous administration of 500 IU heparin.
  - Anesthesia: Overdose of sodium pentobarbitone at $100\mathrm{mg/kg}$.
- Heart Extraction and Perfusion:
  - Post-extraction: Hearts were excised following anesthesia.
  - Perfusion Method: Retrograde perfusion at $25\ \mathrm{mL/min}$, maintained at $37^{\circ}\mathrm{C}$.
  - Perfusion Solution: Nominally calcium-free Krebs-Henseleit solution containing $0.6\mathrm{mg/mL}$ collagenase (Type 1, Worthington Chemical) and $0.1\mathrm{mg/mL}$ protease (Type XIV, Sigma).
  - Perfusion Duration: 6-8 minutes.
- Tissue Dissection:

  - Left Ventricle (LV) Processing: The free wall of the LV was dissected.
  - Layer Separation: Endocardial and epicardial layers were isolated, each approximately 11.5 mm thick.
  - Regional Segmentation: In certain instances, basal and apical segments were separated by approximately 1 cm.

- Cell Preparation and Dye Loading:
  - Dye: FluoVolt voltage-sensitive dye.
  - Concentration: $0.17\mu\ \mathrm{L}/\mathrm{mL}$ in Krebs medium.
  - Loading Duration: 25 minutes at $20^{\circ}\mathrm{C}$.
  - Post-loading Wash: Cells were washed with Krebs-Henseleit solution containing $1.8\mathrm{mmol}/\mathrm{L}$ extracellular calcium.

- Imaging Setup:
  - Observation Platform: Cells were placed on a 35 mm dish with a cover-glass base.
  - Environmental Control: Stage incubator maintained at $37 \pm 1^{\circ}\mathrm{C}$.
  - Microscopy: Utilized $40\times$(NA 0.95) objective lens. item Excitation: Wavelength of 470 ± 20 nm using a light-emitting diode.
  - Emission Collection: Emitted light was collected between 510 and 560 nm using a photomultiplier.
  - Data Acquisition: Signals were digitized at a rate of 10 kHz.

- Cell Stimulation and Selection:
  - Stimulation Frequency: 2 Hz.
  - Pulse Duration: 2 ms.

– Intensity: 1.5 times the threshold, delivered via carbon plate electrodes.

– Inclusion Criteria: Cells that maintained consistent response to 2 Hz field stimulation for more than 4 minutes were selected for analysis.

Drug	Ion Channel Target	IC_{50}
Dofetilide	hERG (I_{Kr})	7 (nM)
Nifedipine	L-type Ca^{2+} (I_{CaL})	0.2 (μM)

Table 3.1: Ion Channel Targets and IC_{50} Values of Dofetilide and Nifedipine taken from (Gao et al. 2020) and (Charnet et al. 1987) respectively

3.2 Method

3.2.1 The equations of McKean model

In order to analyse the research results of (Lachaud et al. 2022), we examine a two-dimensional system of first-order ordinary differential equations, known as the McKean model. McKean introduced this model for the action potential of spiking neurons in (McKean Jr 1970). The equations are comparable to the FitzHugh-Nagumo equations (FitzHugh 1961 and Nagumo et al. 1962), which are themselves a simplified version of the groundbreaking Hodgkin & Huxley (Hodgkin and Huxley 1952) model for the squid giant axon's action potentials. The equations of the McKean model are:

$$\frac{\mathrm{d}v}{\mathrm{d}t} = \varepsilon^{-1} f(v,w;a,b), \qquad f(v,w;a,b) := -(v - H(v-a) + w), \tag{3.1a}$$

$$\frac{\mathrm{d}w}{\mathrm{d}t} = g(v,w;a,b), \qquad g(v,w;a,b) := v - bw, \tag{3.1b}$$

where v and w are functions of time t and dynamical variables, representing the voltage potential across the myocyte's trans-sarcolemmal membrane and an effective gating variable, respectively. The model incorporates three key parameters: a, b, and ε, where ε is a small positive value such that $0 < \varepsilon \ll 1$. Equations (3.1) are dimensionless, with variables v and w and parameters a, b, and ε scaled to remove units. This simplifies analysis by focusing on the system's dynamics without dependence on physical measurements.

The function $H(v-a)$ represents the Heaviside step function defined as:

$$H(v-a) = \begin{cases} 0 \text{ if } v < a, \\ 1 \text{ if } v \geq a. \end{cases}$$

The initial conditions for the McKean model are given as follows:

$$v(0) = v_{\text{stim}} > a, \quad w(0) = w_0, \tag{3.2a}$$

$$v(k\beta) = v_{\text{stim}}, \quad w(k\beta) = w((k-1)\beta) = w_\beta. \tag{3.2b}$$

The variables and parameters used in the above equations are defined in (Table 3.2):

Variable	Definition
v_{stim}	The stimulus voltage applied to the system, where $v_{\text{stim}} > a$.
w_0	The initial value of the gating variable w at $t = 0$.
k	The index representing the cycle number, where $k = 0, 1, 2, \ldots$.
β	The basic cycle length, representing the period of periodic excitation.
w_β	The value of the gating variable w at the beginning of a cycle, chosen to make the system's solution essentially periodic.

Table 3.2: Definition of Variables

The first set of initial conditions (3.2a), specifies the starting point of the simulation. At $t = 0$, the membrane voltage v is initialized to the stimulus voltage v_{stim}, which is greater than the parameter a, ensuring excitability. Simultaneously, the gating variable w starts from the value w_0, which is determined by the system's dynamics.

The second set of conditions, (3.2b), reflects the periodic excitation of the system. The periodic stimulation resets the membrane voltage v to v_{stim} at the start of each cycle k with a period of β. The gating variable w, however, evolves continuously across cycles, with its value at the beginning of each cycle $(w(k\beta))$ determined by the value at the end of the previous cycle ($w((k-1)\beta)$).

The periodic excitation ensures that the system is modeled over successive intervals of length β. The gating variable w is not reset but instead adapts to the periodic stimulation. The value w_β is chosen so that w achieves a periodic steady-state solution, matching the periodic nature of the stimulation protocol. This periodic behavior replicates the experimental conditions described in (Lachaud et al. 2022).

The equations (3.1) serve as a phenomenological model for the action potential of uncoupled rabbit ventricular myocytes. This periodic setup replicates the stimulation protocol used in the experiments of (Lachaud et al. 2022) and ensures that the system behavior matches the observed experimental dynamics. These conditions and their implementation in the model are further explained and justified in our published paper (Simitev et al. 2023).

The numerical solutions for specific values of a and b in the McKean model produce a generic action potential waveform, as shown in Figure 3.1(a). These waveforms are consistent with those experimentally observed, as demonstrated in Figures 1 and 2 of (Lachaud et al. 2022).

In many cases, the inherent complexity of the McKean model makes obtaining exact analytical solutions impractical. To address this, asymptotic methods are employed, which approximate solutions by simplifying the model. These methods are particularly effective when dealing with systems characterized by distinct timescales or complex parameters, allowing for a clearer understanding of the system's dynamics (Biktashev et al. 2008).

This approach ensures the model remains both computationally efficient and theoretically robust, enabling accurate modeling of the experimental results from (Lachaud et al. 2022).

In the study conducted by Biktashev et al. (Biktashev et al. 2008), the asymptotic approach was successfully applied to the caricature Noble model (Noble 1962). This technique was used to explore the slow and fast manifolds within the system, allowing for a clearer understanding of its dynamic behaviour. The Noble model, like many ionic models, contains parameters that can complicate simulations and analyses. By applying asymptotic methods, these parameters can be effectively reduced or eliminated, thereby simplifying the model and making its behaviour easier to analyse.

3.2.2 Asymptotic approximation of McKean model

Inspired by the success of this approach, I applied a similar asymptotic method to solve the McKean model (McKean Jr 1970). The goal was to reduce the complexity of the model, enabling a more straightforward examination of its properties and dynamics. This method not only facilitates the analysis of the McKean model but also provides insights into its behaviour that might be difficult to obtain through direct analytical or numerical methods. By simplifying the model in this way, the asymptotic approach proves to be a powerful tool in the study of complex systems. Consider the unique asymptotic limit as ε approaches zero from the positive side; $\varepsilon \to 0^+$, in which equations (3.1) are simplified to a fast-time subsystem :

$$\frac{\mathrm{d}v}{\mathrm{d}\tau} = f(v,w), \quad \frac{\mathrm{d}w}{\mathrm{d}\tau} = 0, \tag{3.3}$$

when expressed in terms of the fast-time variable $\tau := \varepsilon^{-1}t$. When written in terms of the original slow-time variable $t = O(1)$, the equations (3.1) reduce to the slow-time subsystem in equation:

$$0 = f(v,w), \quad \frac{\mathrm{d}w}{\mathrm{d}t} = g(v,w). \tag{3.4}$$

The nullcline, denoted as $f(v,w) = 0$, is a simplified representation of a cubic function of v. It is presented as a piece-wise linear graph in Figure 3.1(b).

The nullcline $f(v,w) = 0$ is referred to as the 'critical set' because it corresponds directly to the fixed points of the fast subsystem equation (3.3) and because the trajectories of the slow subsystem equation (3.4) are restricted to follow it. More precisely, the function has local minima and maxima at the coordinates $M_{\min} = (a, -a)$ and $M_{\max} = (a, 1-a)$, respectively,

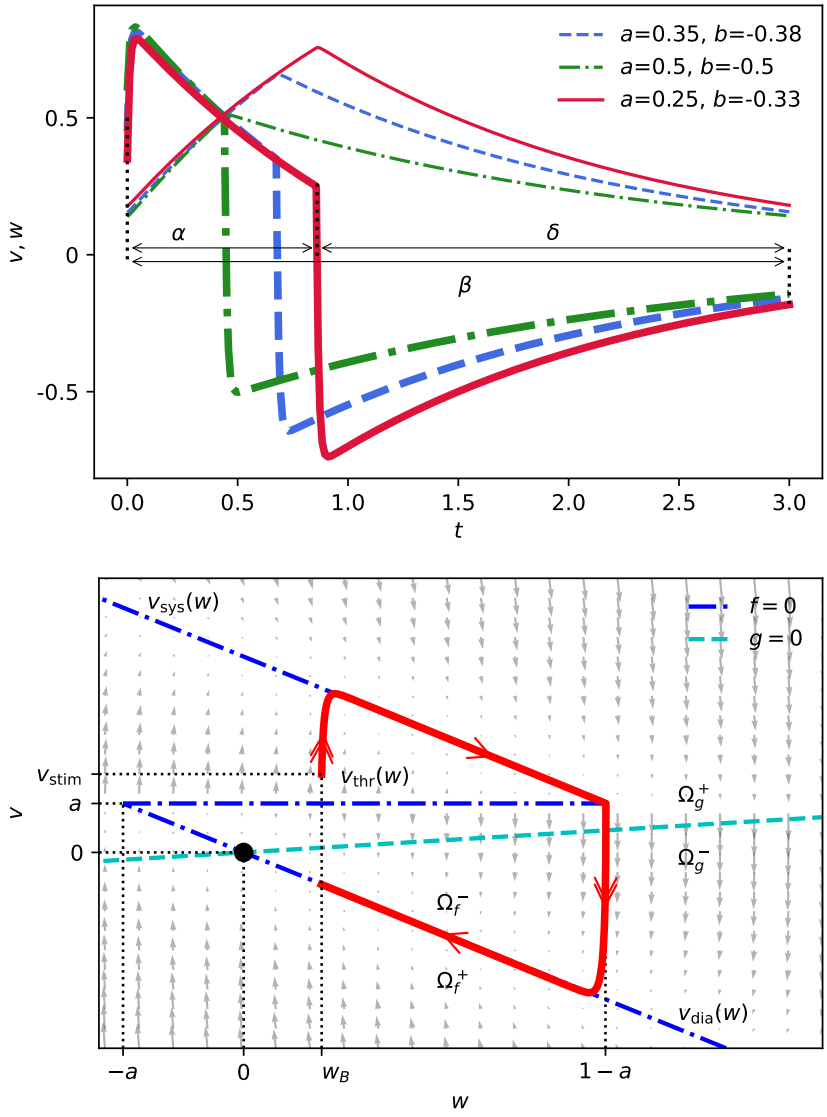

Figure 3.1: (a). Three examples of action potential solutions to the McKean equations (3.1). The 'voltage' $v(t)$ (thick curves) and the effective 'gating variable' $w(t)$ (thin curves) are shown as functions of time for parameter values $\varepsilon = 0.01, \beta = 3$ and randomly selected combinations of a and b as shown in the legend. The action potential duration α, diastolic interval δ, and basic cycle length β are annotated on one of the AP curves. (b). Phase portrait and vector field of the McKean equations (3.3) and associated notation. The nullclines $f = 0$ and $g = 0$ are shown as a dash-dotted blue line and a dashed turquoise line, respectively. The single attracting global equilibrium $(0,0)$ is marked with a black dot marker. A typical trajectory is shown in a solid red line where a double arrow indicates a fast piece and a single arrow indicates a slow piece of the trajectory. Parameter values used are $a = 0.25, b = 0.3, \varepsilon = 0.01$ and correspond to excitable dynamics. The figure is from our published paper (Simitev et al. 2023)

and also contains the roots in:

$$\begin{cases} v_{\text{sys}} = 1 - w & \text{for } w \in (-\infty, -a], \\ v_{\text{thr}} = a, v_{\text{sys}} = 1 - w & \text{for } w \in [-a, 1-a], \\ v_{\text{dia}} = -w & \text{for } w \in [1-a, \infty). \end{cases} \tag{3.5}$$

Since $f(v,w) < 0$ in the region $\Omega_f^- := \{(v,w) \in \mathbb{R}^2 : w > \bar{w} \text{ where } f(v,\bar{w}) = 0\}$, and $f(v,w) > 0$ in the region $\Omega_f^+ := \{(v,w) \in \mathbb{R}^2 : w < \bar{w} \text{ where } f(v,\bar{w}) = 0\}$, the branches $v_{\text{sys}}(w)$ and $v_{\text{dia}}(w)$, called 'systolic' and 'diastolic', respectively, consist of stable attracting fixed points and the 'threshold' branch $v_{\text{thr}}(w)$ consists of unstable repelling fixed points of the fast-subsystem (3.3). The second nullcline $g(v,w) = 0$ is a straight line which partitions the phase plane in two regions $\Omega_g^- := \{(v,w) \in \mathbb{R}^2 : w > \bar{w} \text{ where } g(v,\bar{w}) = 0\}$ where $g(v,w) < 0$, and $\Omega_g^+ := \{(v,w) \in \mathbb{R}^2 : w < \bar{w} \text{ where } g(v,\bar{w}) = 0\}$ where $g(v,w) > 0$ and thus determines the direction of the slow flow of (3.3) along the critical set. These facts are illustrated by the vector field shown in Figure 3.1(b). Thus, in the singular approximations given by (3.3) and (3.4) a typical trajectory of the McKean model (3.1) consists of fast jumps to one of the attracting branches of the critical set followed by slow motions to the end the attracting region or until a globally stable fixed point is reached as illustrated in Figure 3.1(b).

Global fixed points occur at the intersection of the two nullclines and apart from degenerate cases there exists either one single or three distinct fixed points given by:

$$(v_*, w_*) \in \begin{cases} \{(0,0)\} & \text{if } b < a/(1-a), \\ \{(0,0), (a, a/b), (b/(1+b), 1/(1+b))\} & \text{if } b \geqslant a/(1-a). \end{cases} \tag{3.6}$$

Biological excitability refers to the response of a system to an external stimulus, which causes a significant and finite reaction before returning to a single equilibrium state. In McKean's model (3.1), excitability is associated with a single stable attractor positioned between the fold points $M_{\min}$ and $M_{\max}$ on the diastolic branch $v_{\text{sys}}(w)$. This corresponds to a specific parameter space:

$$\Omega_{\text{ex}} = \{(a,b) \in \mathbb{R}^2 : \quad b > -1 \cap b < a/(1-a) \cap a > 0 \cap a < 1\}. \tag{3.7}$$

Region Ω_{ex} is depicted in Figure 3.1(a). In this scenario, beginning from the initial conditions (3.2b) , the trajectory undergoes a rapid jump of an infinitesimally short duration $O(\varepsilon)$, moving from the point $(v_{\text{stim}}, w_\beta)$ to the point $(v_{\text{sys}}(w_\beta), w_\beta)$, as dictated by the fast subsystem (3.3). Following this, the trajectory traces the systolic branch from this point to the point $M_{\max}$, over

a time period determined by integrating the slow subsystem (3.4):

$$\alpha := \int_{w_\beta}^{1-a} \mathrm{d}t = \int_{w_\beta}^{1-a} \frac{\mathrm{d}w}{g\left(v_{\mathrm{sys}}(w), w\right)} = \frac{1}{1+b} \log\left(\frac{1-(1+b)w_\beta}{1-(1+b)(1-a)}\right). \tag{3.8}$$

At the fold point $M_{\max}$ the systolic branch of the critical set v_{sys} terminates and switches to the repelling threshold branch v_{thr} so the trajectory makes another infinitesimally short fast jump over to point $(v_{\mathrm{dia}}(1-a), 1-a)$. Finally, the trajectory follows the attracting diastolic branch $v_{\mathrm{dia}}(w)$ towards the single global stable fixed point $(0,0)$ for period of duration found by integrating the slow subsystem (3.4):

$$\delta := \int_{1-a}^{w_\beta} \mathrm{d}t = \int_{1-a}^{w_\beta} \frac{\mathrm{d}w}{g\left(v_{\mathrm{dia}}(w), w\right)} = \frac{1}{1+b} \log\left(\frac{1-a}{w_\beta}\right). \tag{3.9}$$

This pattern repeats when the system receives its next excitation stimulus at $(v_{\mathrm{stim}}, w_\beta)$, as depicted in Figure 3.1(b). The parameter w_β, introduced in the initial conditions (3.2b), is not an independent variable but is instead determined by the specified basic cycle length β. For the uniqueness and existence of solutions to an initial-value problem, the solutions of equations (3.1) must be identical up to a time shift (i.e., periodic APs) over two consecutive intervals $t \in (k\beta, (k+1)\beta], k \in \mathbb{N}$, requiring that they start from identical initial conditions. This condition implies that a periodic sequence of action potentials can only exist when the sequence $w(k\beta), k = 0, 1, \ldots$ converges to a unique value w_β, possibly after a transient phase involving a finite number of stimuli $k > m$. There may be parameter values, including β, for which the sequence does not converge and instead produces more complex behaviors, such as alternans.

Alternans, specifically APD alternans, is a response in which action potentials alternate between long and short durations despite a constant pacing cycle length. However, a strictly periodic response to external stimulation is assumed. Under this assumption, and using asymptotic approximation, the duration of any fast jumps is considered negligible, of order $O(\varepsilon)$. Consequently, expression (3.8) is identified as the duration of the action potential (APD), and expression (3.9) is identified as the diastolic interval (DI). It is therefore required that the sum

of the APD and DI equals the BCL as in the following equation:

$$\beta = \alpha + \delta = \frac{1}{1+b} \log \left(\frac{\left(1-(1+b)w_\beta\right)(1-a)}{(1-(1+b)(1-a))w_\beta} \right). \tag{3.10}$$

By solving this algebraic equation, one can determine the value of w_β that is required to create a periodic sequence of action potentials (APs) of length:

$$w_\beta = ((1+b) + \exp((1+b)\beta)(1-(1+b)(1-a))/(1-a))^{-1}. \tag{3.11}$$

By substituting equation (3.11) into equation (3.8), we obtain explicit closed-form formulas for the APD and the DI. These expressions are functions of the basic model parameters a and b, s well as the basic cycle length (BCL) parameter β.

The APD and DI are expressed as:

$$\alpha(a,b,\beta) = \frac{1}{\tilde{b}} \log \left(\frac{\exp(\tilde{b}\beta)}{\tilde{a}\tilde{b} + (1-\tilde{a}\tilde{b})\exp(\tilde{b}\beta)} \right), \quad \tilde{a} := 1-a, \tilde{b} := 1+b, \tag{3.12a}$$

$$\delta(a,b,\beta) = \beta - \alpha(a,b,\beta). \tag{3.12b}$$

These asymptotic formulas provide a detailed framework for analyzing the system's dynamics by describing how the action potential duration (APD) and diastolic interval (DI) vary as functions of the model parameters. Figure 3.2 visualises these relationships within the parameter domain Ω_{ex}, offering insights into the interactions between a, b, and β. The red wireframe represents the APD (α), while the blue wireframe illustrates the DI (δ). Additionally, the black wireframe shows the surface where $\beta = \alpha + \delta$, serving as a consistency check and illustrating the excitable dynamics domain Ω_{ex} for the specified values of a, b, and β.

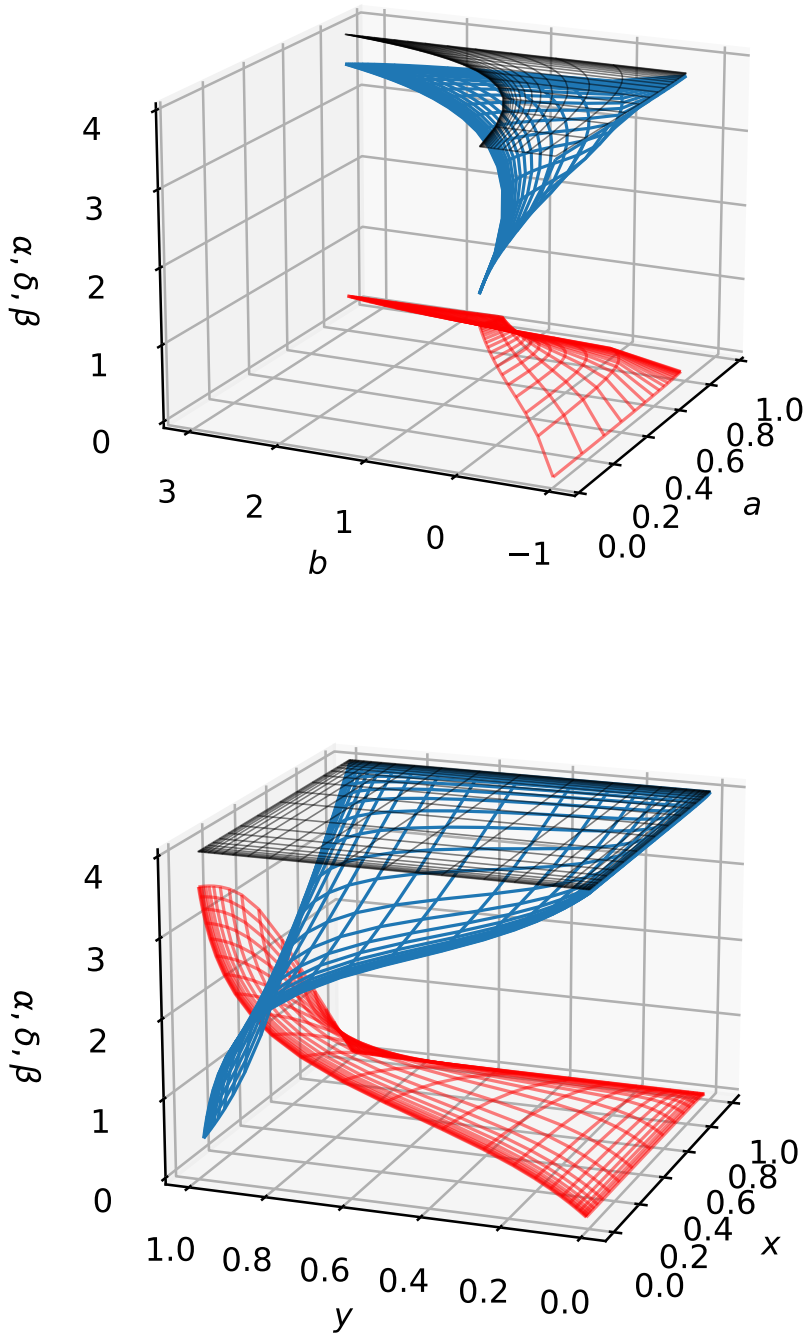

Figure 3.2: Asymptotic expressions (3.12a) and (3.12b) for the action potential duration α (red wire-frame) and diastolic interval δ (blue wire-frame), respectively, as functions of the McKean model parameters a and b in (a), and as functions of the 'rectangular' variables x and y defined in equation equation (3.13) in (b). The value of the basic cycle length is $\beta = 4$ and the surfaces $\beta = \alpha + \delta$ (black wire-frame) are plotted as a test and to illustrate the parameter space Ω_{ex} for excitable dynamics given by equation (3.7). The figure is from our published paper (Simitev et al. 2023)

The transformations $\tilde{a} := 1 - a$ and $\tilde{b} := 1 + b$ simplify the expressions for APD and DI, while the parameter space mapping $(a,b) \to (x,y)$ ensures clarity in visualizing the excitable dynamics domain. These tools, combined with the restitution analysis, provide a comprehensive framework for understanding the dynamics of the McKean model under periodic stimulation.

To simplify the parameter space, a change of variables is introduced:

$$a = x, \quad b = y/(1-x) - 1, \quad x \in (0,1), \quad y \in (0,1), \tag{3.13}$$

This transformation maps the excitable dynamics domain Ω_{ex} into the rectangular domain $(x,y) \in (0,1) \times (0,1)$, , making the parameter space easier to visualize and interpret.

The value of w_β, required for periodic stimulation, is illustrated in Figure 3.3(a). It shows w_β as a function of x and y for a fixed $\beta = 4$ This reveals that for a population of uncoupled McKean models, where each model is characterized by different values of a and b, the initial condition w_β varies between models to maintain a stable periodic response. Channel-blocking drugs, which modify the ratio of open channels, can thus have different effects on individual cells due to variations in w_β across the population.

Figure 3.3(b) presents the restitution curves (α as a function of δ) and their gradients for selected combinations of a and b. These curves display the typical forms observed in experimental data, and the gradients confirm the absence of instabilities for the chosen parameter values.

3.2.3 Mathematical Representation of Ion Channel Block Experiment

We assume that myocytes can be mathematically described by the McKean equations (3.1). Consider the dataset of experimental measurements $\mathscr{D}(B,\Gamma)$, defined as a collection of pairs of action potential duration (APD) values A_i and $(A_i + \Delta A_i)$, measured before and after the application of a drug, respectively. These measurements are taken for each cell $i = 1,\ldots,N$, under a fixed experimental basic cycle length B and drug concentration Γ. For this study,

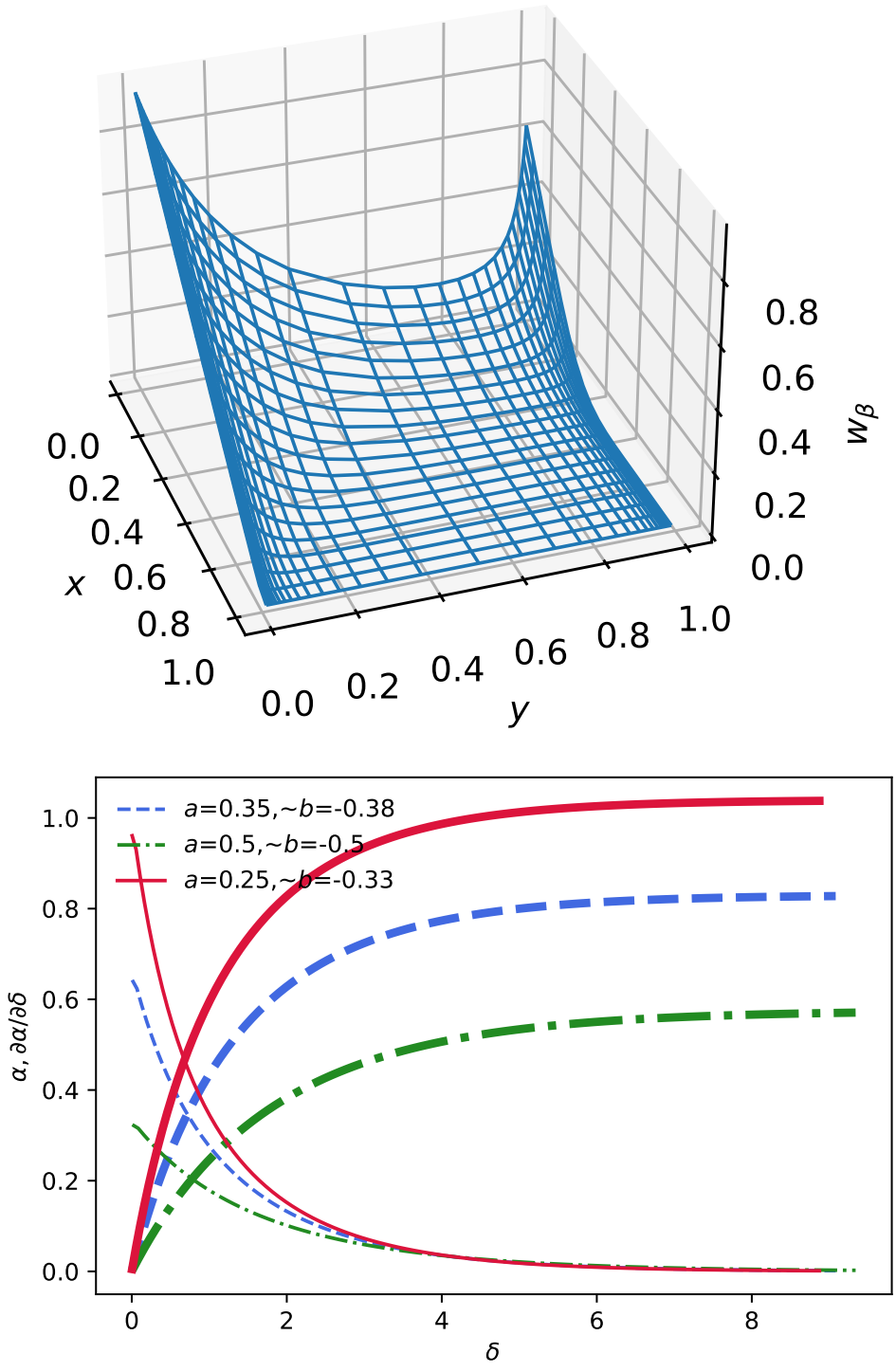

Figure 3.3: (a). The initial condition w_β required for conformance to stimulation with fixed period $\beta = 4$ given by equation (3.11) as a function of the 'rectangular' variables x and y defined in equation (3.13). (b). Examples of asymptotic restitution curves α as a function of δ (thick lines) and their derivatives $\partial_\delta \alpha$ (thin lines) for selected McKean parameter values given in the legend. The figure is from our published paper (Simitev et al. 2023)

$B = 500\ \mathrm{ms}, \Gamma = 1\mu\mathrm{M}$ Nifedipine, and the total number of cells $N = 496$. The dataset is represented as:

$$\mathscr{D}(B,\Gamma) = \{(A_i(B), (A_i(B) + \Delta A_i(B,\Gamma))), \quad i = 1,\ldots,N\}. \tag{3.14}$$

To model these measurements using the McKean equations, we define the set of corresponding McKean model parameters (a_i, b_i) for each cell i as:

$$\mathscr{P}(\beta,\gamma) = \{(a_i, b_i), \quad i = 1,\ldots,N\}, \tag{3.15}$$

Here, β represents the model's basic cycle length parameter, and γ is a parameter introduced to account for the effect of drug action on the McKean model. Specifically:

- β : The basic cycle length in the McKean model, analogous to B in the experimental setup, but expressed in non-dimensional units.

- γ : A factor $(\gamma > 0)$ representing the influence of drug action, which modifies the McKean model parameter a. For instance, $\gamma > 1$ reflects a reduction in the effective conductance associated with ionic currents, as caused by channel-blocking drugs like Nifedipine.

Using these parameters, the relationship between the APD values (before and after drug application) and the McKean model is expressed by the following system of $2N$ non-linear equations

$$A_i/B = \alpha(a_i, b_i, \beta)/\beta, \tag{3.16a}$$

$$(A_i + \Delta A_i)/B = \alpha(\gamma a_i, b_i, \beta)/\beta, \quad i = 1,\ldots,N. \tag{3.16b}$$

The key parameters in the McKean model and their roles in equations (3.16) are summarized in the table below:

Parameter	Definition
α	This represents the asymptotic expression for the action potential duration, as given in equation (3.12a).
β	This is the basic cycle length.
γ	A parameter that represents the effect of drug action within the McKean model ($\gamma > 0$).

The influence of the drug is modeled by incorporating the factor γ into the parameter a in equation (3.16b). While the McKean model is not a detailed electrophysiological model, its parameter a is analogous to the total ionic current conductance in more physiologically detailed models. Specifically:

Parameter	Definition
a	The only parameter on the right-hand side of the McKean 'voltage' equation (3.1a) , which, in physiologically realistic models, represents the total sum of all ionic currents.
b	governs the rate of change of the effective gating variable w via equation (3.1b) and should therefore be interpreted as an effective kinetic parameter.

For the Nifedipine dataset $(\gamma > 1)$ provided in (Lachaud et al. 2022), this framework models the observed reduction in APD due to channel blockade. However, note that $\gamma > 1$ does not imply enhanced channel activity but rather reflects a shift of the v-nullcline upwards along the v-axis in the phase plane.

The other drug considered in (Lachaud et al. 2022) , Dofetilide, is not modeled here due to its more complex effects:

- Although Dofetilide data is provided in (Lachaud et al. 2022), it will not be modeled here. Dofetilide has a more complex effect, as it prolongs the APD in some cells while shortening it in others (see Fig. 3B(iii) in (Lachaud et al. 2022).
- Previous studies have shown that Dofetilide is a multi-channel blocker, which means it affects multiple different ion channels. One of these channels is known as (I_{Kr}) (Crumb Jr et al. 2016). The article by Yang (Yang et al. 2001) has examined the inhibitory effects of Dofetilide on the slow component of the delayed rectifier potassium current, also known as I_{Ks}. Furthermore, (Li et al. 2017) elucidates the impact of Dofetilide on the late sodium current, denoted as (I_{NaL}), in cardiac cells. Therefore, when $\gamma < 1$, which just prolongs the action potential duration (APD), it is inadequate to fully capture the impact of this drug.
- To model Dofetilides effect accurately, two distinct 'effective conductance' parameters (similar to a) would be required: one to shorten and one to prolong the APD. However, the McKean model only includes a single parameter a for this purpose, while the second parameter b functions as an effective kinetic parameter and cannot serve this role.

3.2.4 Application of McKean Asymptotics to Experimental Data

The multiplicative model $\bar{a} = \gamma a$, where a and $\bar{a}$ represent the values of the McKean parameter a before and after drug administration, respectively, is derived from a linear approximation of the more general relationship $\bar{a} = \bar{a}(\Gamma)$, where a is a function of the drug concentration Γ. For sufficiently small values of Γ, the relationship can be approximated as:

$$\bar{a} = \bar{a}(\Gamma) \approx (1 + k\Gamma)a, \quad \text{where} \quad a = \bar{a}(0), \quad \text{and} \quad k = \frac{\partial \bar{a}}{\partial \Gamma}(0),$$

leading to the conclusion that the multiplication factor γ depends linearly on the drug concentration Γ, $\gamma := (1 + k\Gamma)$. The constant k can be eliminated by calibrating with a known value $\gamma^* = (1 + k\Gamma^*)$, resulting in an explicit relationship between the drug concentration Γ and the drug action parameter γ:

$$\Gamma = \Gamma^* \frac{\gamma - 1}{\gamma^* - 1}.$$

This relationship is then applied in equation (3.26), with the calibration values γ^* and Γ^* discussed in the next section. Note that, the multiplicative model shares similarities with the 'conductance-block' model used in realistic cardiac ionic current models. In these models, the ion channel current is expressed as $I_j = g_j^0 O\left(V - E_j\right)$, where g_j^0 represents the maximal conductance of a population of fully open channels of type j, O is the open probability, and E_j is the reversal potential for the ion species flowing through these channels.

To incorporate drug action in these models, the maximal conductance g_j is multiplied by a factor $\gamma_{\text{ion}} = K_d/\left(K_d + \Gamma\right)$ which represents the percentage of channels C/C_0 that remain unbound in the presence of the drug. This expression is derived using a steady-state approximation of the law of mass action for the reaction $C + \Gamma \underset{k_+}{\overset{k_-}{\rightleftharpoons}} B$, where $k_\pm$ are the reaction rates, C and B are the open and bound channels, and $C + B = C_0$ represents the total channel population. The equilibrium constant $K_d := k_-/k_+$ measures the drug's potency and is often approximated by the half-maximal inhibitory concentration (IC50) obtained from experiments.

Although the 'conductance-block' model is commonly employed in numerical studies e.g., (Mirams et al. 2011), it cannot be directly applied here because the McKean parameter a is not an actual ion channel conductance, despite functioning similarly in the model.

3.2.5 Domain of Excitability

The equations in (3.16) are only defined within a specific subset of the excitability domain, denoted as $\Omega_{\text{ex}}^{\gamma} \subset \Omega_{\text{ex}}$, where Ω_{ex} is given by equation (3.7). For a cell to remain excitable after drug application, the parameter a must be confined to the interval $a \in (0, 1/\gamma)$, rather than the original interval $(0,1)$. This is because, after drug administration, the effective conductance is represented as $\bar{a} = \gamma a$. A necessary condition for the validity of equation (3.12a) is that $\bar{a} < 1$. As a result, the equations in (3.16) are limited to the domain defined by (3.17) and illustrated in Figures 3.4(a) and 3.5(b).

$$\Omega_{\text{ex}}^{\gamma} = \left\{(a,b) \in \mathbb{R}^2 : \quad b > -1 \cap b < a/(1-a) \cap a > 0 \cap a < 1/\gamma\right\}. \tag{3.17}$$

The conditions for the existence of solutions to equations (3.16) are now clarified. The system of $2N$ nonlinear algebraic equations decouples into N independent pairs, each corresponding to a single cell. Consider one such pair of equations in the symbolic form in (3.18a) where $\mathbf{F} : S \subset \mathbb{R}^4 \to \mathbb{R}^2$ is a continuous vector-valued function. The components F_1 and F_2 of $\mathbf{F}$ are given by (3.18a);

$$\mathbf{F}(A, \Delta A, a, b) = \mathbf{0}, \tag{3.18a}$$

$$\mathbf{F} = \begin{pmatrix} F_1 \\ F_2 \end{pmatrix} = \begin{pmatrix} A/B - \alpha(a, b, \beta)/\beta \\ (A + \Delta A)/B - \alpha(\gamma a, b, \beta)/\beta \end{pmatrix}. \tag{3.18b}$$

The points in $\mathbb{R}^4$ are represented as $(\mathbf{x}, \mathbf{y})$, where $\mathbf{x} = (A, \Delta A) \in \mathbb{R}^2$ and $\mathbf{y} = (a, b) \in \mathbb{R}^2$. It is important to note that, according to the implicit function theorem, if $(\mathbf{x}_0, \mathbf{y_0}) \in S$ is a point, such that:

$$\mathbf{F}(\mathbf{x_0}, \mathbf{y_0}) = \mathbf{0}, \text{ and } \det\left[\partial_{\mathbf{y}} \mathbf{F}\right]_{(\mathbf{x}_0, \mathbf{y_0})} \neq 0, \tag{3.19}$$

then for every $\mathbf{x}$ in a neighbourhood of $\mathbf{x}_0$, there exists a unique function $\mathbf{f}$ with $\mathbf{f}(\mathbf{x}) = \mathbf{y}$in a neighbourhood of $\mathbf{y}_0$ where $\mathbf{F}(\mathbf{x}, \mathbf{y} = \mathbf{f}(\mathbf{x})) = 0$ holds. The determinant of the Jacobian matrix, denoted by J, in the equation:

$$\det\left[\partial_{\mathbf{y}} \mathbf{F}\right] = J = \det\left(\frac{\partial\left(F_1, F_2\right)}{\partial(a, b)}\right), \tag{3.20}$$

represents the determinant of the matrix formed by taking the partial derivatives of the components of vector $\mathbf{F}$ with respect to the components of vector $\mathbf{y}$. The points $(\mathbf{x}_0, \mathbf{y}_0)$ that meet the first condition in (3.19) are guaranteed to exist. This is because, for any given value of $\mathbf{y}_0$ within the domain $\Omega \mathrm{ex}^{\gamma}$, a corresponding value of $\mathbf{x}_0$ can be found by directly calculating the right-hand side of the equations in (3.16). Additionally, these pairs of points are unique. Calculating the determinant of the Jacobian matrix is a straightforward process, but it results in a complex expression. To check the second condition in (3.19), this determinant was evaluated numerically, and the resulting surface, $J(a, b)$, was plotted over the domain $\Omega_{\mathrm{ex}}^{\gamma}$ as shown in Figure 3.4(a).

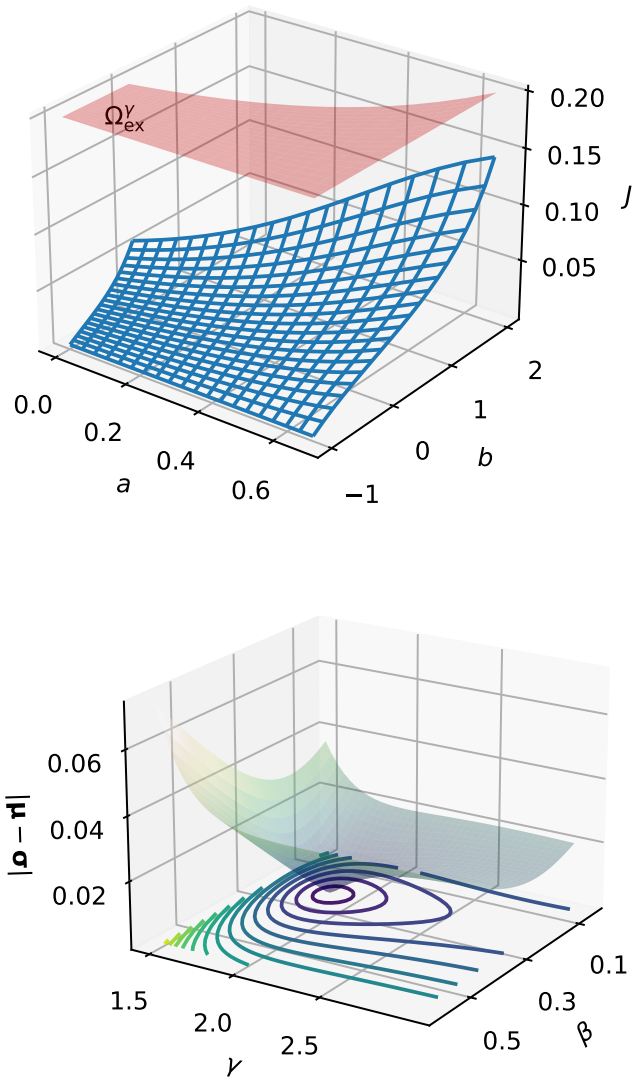

Figure 3.4: (a). The Jacobian determinant $J = \det\left(\partial\left(F_1, F_2\right)/\partial(a,b)\right)$ as a function of parameters a and b for $\beta = 0.3$ and $\gamma = 1.5$ is shown by a blue wire frame, with the grid lines being iso-lines of the rectangular coordinates x and y defined in equation (3.13). The pink transparent region at the top of the axes box is the domain of excitability $\Omega_{\text{ex}}^{\gamma}$. (b). Convexity and optimal calibration of excitability parameters, this plot illustrates the distance $|\mu - \sigma|$ between the center of mass μ of the parameter set $\mathscr{P}(\beta,\gamma)$ and the centroid σ of the excitability domain $\Omega_{\text{ex}}^{\gamma}$. The globally convex surface ensures the existence of a unique global minimum, indicating an optimal calibration of β and γ. This minimization balances mathematical rigor with physiological relevance, as it positions the parameters well within the domain of excitability, avoiding instability near the boundaries and ensuring uniform excitable dynamics across the system. The figure is from our published paper (Simitev et al. 2023)

The plot demonstrates that J is strictly positive across the entire domain, although it approaches 0^{+} as b gets closer to -1. However, the value $b = -1$ is excluded from the open domain $\Omega_{\text{ex}}^{\gamma}$. This is significant because $b = -1$ represents a degenerate case where the w-nullcline and the diastolic branch of the v-nullcline in the McKean model in equation (3.1)

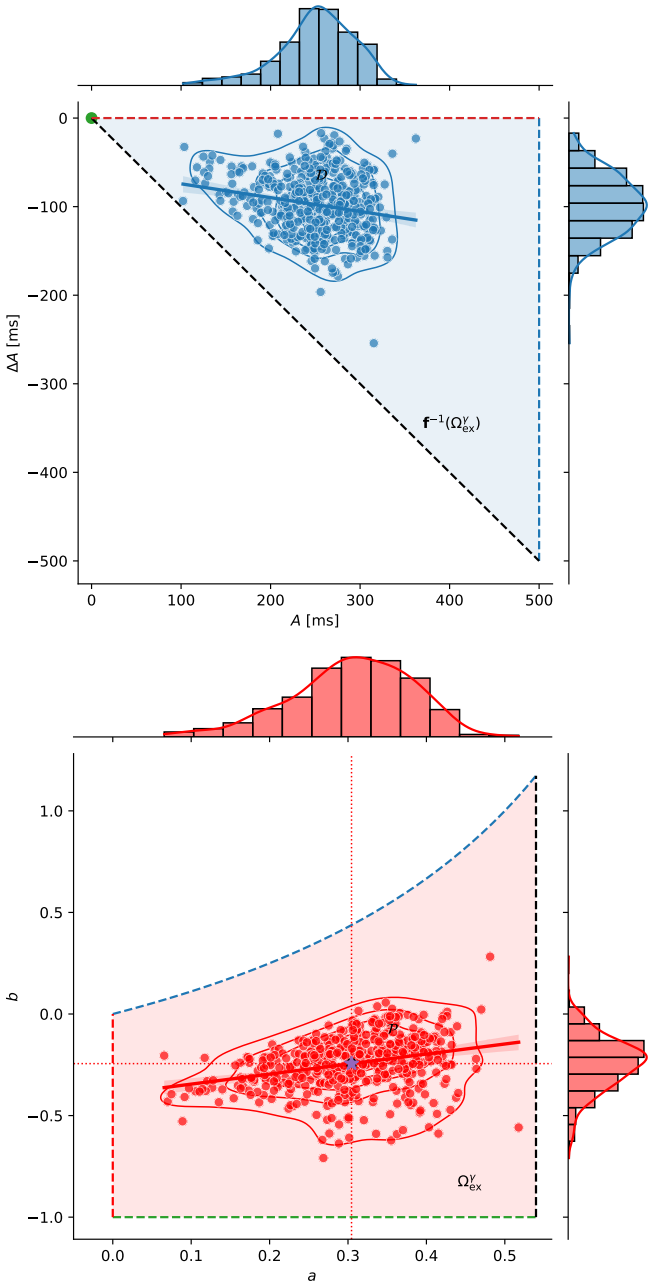

Figure 3.5: (a). Scatter plot of the set $\mathscr{D}(B,\Gamma)$ of 496 experimental measurements at $B = 500$ ms and $\Gamma = 1\mu$M Nifedipine, data due to (Lachaud et al. 2022) c.f. their figure 3C(iii). (b). Scatter plot of the set $\mathscr{P}(\beta^*,\gamma^*)$ of corresponding McKean parameters obtained by numerical solution of the inverse problem (3.16) with calibrated $\beta^* = 0.235$ and $\gamma^* = 1.853$. Thin dotted lines denote the locations of the mean values of a_i and b_i with their intersection being the centre of mass μ of $\mathscr{P}$ and the violet star marker is the centre of mass σ of $\Omega^{\gamma}_{\text{ex}}$. The shaded areas are the parameter region for excitable dynamics $\Omega^{\gamma}_{\text{ex}}$ in (b) and its pre-image in (a). Histogram distributions with Gaussian kernel density estimations and simple data regression lines are also plotted in both panels. The figure is from our published paper (Simitev et al. 2023)

coincide, leading to a non-excitable state. Based on these observations, it can be concluded that a unique solution to equation (3.18) exists within the domain $\Omega^{\gamma}_{\text{ex}}$. This solution can be

expressed as:

$$(a,b) = \mathbf{f}(A,\Delta A) \tag{3.21}$$

Here, the parameters a and b can be determined as functions of the experimental data, denoted by $(A,\Delta A)$. The process of finding a closed-form solution for equation (3.16a) can be simplified to solve for the parameter a as a function of (b,A) alone. The solution is given by:

$$a = 1 - \frac{\exp(\tilde{b}\beta)(\exp(\tilde{b}A\beta/B)-1)}{\tilde{b}(\exp(\tilde{b}\beta)-1)\exp(\tilde{b}A\beta/B)}, \quad \tilde{b} = 1+b \tag{3.22}$$

However, solving equation (3.16b) for b is more challenging and cannot be done as easily. Because of this difficulty, a numerical approach is used to solve both equations (3.16) for the parameters a and b. The numerical method employed is straightforward and efficient. Specifically, the modified Powell hybrid method (Powell 1970), as implemented in the SciPy numerical library (Virtanen et al. 2020), is used to obtain the solutions.

3.2.6 Calibration of Basic Cycle Length and Drug Dose

To accurately analyse the system, it's essential to determine the unknown parameters involved in equations (3.16). These include not only the individual parameters a_i and b_i for each of the N cells but also the basic cycle length (BCL) denoted by β, and the drug dose parameter represented by γ. Given that these characteristics are not fixed, a systematic technique is required to calibrate them. To ensure a meaningful calibration, we impose two primary constraints:

- All solutions (a_i,b_i) for $i = 1,\ldots,N$ must fall within the excitability domain $\Omega_{\text{ex}}^{\gamma}$. This ensures that the system remains physiologically excitable.
- The distribution of these solutions should minimise the distance between their center of mass and the center of mass of the excitability domain $\Omega_{\text{ex}}^{\gamma}$. In other words, solutions should be positioned as close to the centre of the excitability domain as possible, while avoiding to be near the boundaries where the system may lose its ability to be excited.

Based on the above constraints, we define the calibration problem as a minimisation task:

$$(\beta^*, \gamma^*) = \arg\min_{(\beta,\gamma)} |\mu(\beta,\gamma) - \sigma(\beta,\gamma)| \text{ subject to } (a_i(\beta^*,\gamma^*), b_i(\beta^*,\gamma^*)) \in \Omega_{\text{ex}}^{\gamma} \forall i = 1,\ldots,N \tag{3.23a}$$

$$\mu[\mathscr{P}(\beta,\gamma)] := \frac{1}{N}\left(\sum_{i=1}^{N} a_i(\beta,\gamma), \quad \sum_{i=1}^{N} b_i(\beta,\gamma)\right), \tag{3.23b}$$

$$\sigma\left[\Omega_{\text{ex}}^{\gamma}(\beta,\gamma)\right] = \left(\log\frac{\gamma}{\gamma-1} - \frac{1}{\gamma}, \log\frac{\gamma-1}{\gamma} + \frac{1}{2(\gamma-1)}\right) / \log\frac{\gamma}{\gamma-1}. \tag{3.23c}$$

Here:

Parameter	Definition
μ	represents the position vector of the center of mass of the set $\mathscr{P}(\beta,\gamma)$, which comprises the discrete points (a_i, b_i) in the (a,b)-plane. It is computed by the equation (3.23b)
σ	denotes the position vector of the center of mass of the excitability domain $\Omega_{\text{ex}}^{\gamma}$ in the (a,b)-plane, calculated by the equation (3.23c)

The objective is to find the values of β and γ that minimise the distance between μ and σ, ensuring that all parameter pairs (a_i, b_i) remain within the excitability domain $\Omega_{\text{ex}}^{\gamma}$. Minimizing the distance between the center of mass μ of the parameter set $\mathscr{P}(\beta,\gamma)$ and the centroid σ of the excitability domain $\Omega_{\text{ex}}^{\gamma}$ strikes a balance between mathematical rigor and physiological relevance. From a mathematical perspective, this approach ensures that the parameter values are well-centered within the domain, avoiding proximity to the boundaries where excitability may be lost. Physiologically, it reflects the natural variability observed in cardiac cells, ensuring that the calibrated parameters produce robust and uniform excitable behavior across the system. This minimization thus provides a practical framework for optimizing parameters while maintaining consistency with both experimental observations and theoretical constraints.

As solving the minimisation problem analytically is challenging due to its nonlinear nature and the presence of constraints. We tried to gain insights by numerically evaluating the minimisation surface, representing the distance $|\mu - \sigma|$, using experimental measurements $(A_i, \Delta A_i)$ from (Lachaud et al. 2022). Contour lines of this surface were plotted in the (β, γ) plane in Figure 3.4(b). The plot revealed a globally convex surface with a single minimum, suggesting the existence of a unique global minimum. While this doesn't constitute a formal proof, it provides strong evidence supporting the uniqueness of the solution for β and γ.

To robustly identify the optimal values of β and γ, especially given the complexity of the problem, a stochastic optimisation method was employed.This method combines classical and fast-simulated techniques (Tsallis and Stariolo 1996) with a local search strategy at accepted points (Xiang and Gong 2000). It's well-suited for constrained global optimisation problems involving multimodal and multivariate objective functions. The SciPy numerical library's implementation of dual annealing (Virtanen et al. 2020), was utilised to perform the optimisation. The application of this method successfully identified the optimal values of β and γ, ensuring that all parameter pairs (a_i, b_i) reside within the excitability domain while minimizing the distance between their center of mass and that of $\Omega_{\text{ex}}^{\gamma}$.

3.3 Results

Figure 3.5(a) presents the experimentally obtained dataset $\mathscr{D}(B, \Gamma)$, which includes pairs of values $(A_i, \Delta A_i)$ for $i = 1, \ldots, N$, taken from the study by (Lachaud et al. 2022). In contrast, Figure 3.5(b) displays the corresponding solution set $\mathscr{P} = \{(a_i, b_i), i = 1, \ldots, N\}$, derived by solving the problem defined by equations (3.16) and (3.23). This solution set was obtained through numerical methods and visually represents the primary results of the approach described earlier.

The solution process involves several steps. For each pair of parameters β and γ, the domain of excitability $\Omega_{\text{ex}}^{\gamma}$ is constructed based on equation (3.17). The inverse problem, given by equation (3.16), is then solved numerically within this domain. Subsequently, the distance between the respective centers of mass, calculated using equations (3.23b) and (3.23c), is determined. The final step minimises this distance with respect to β and γ as outlined in equation (3.23a).

For the specific experimental dataset under consideration, this calibration process determines the values of the basic cycle length and the drug dose parameter, resulting in $\beta^* = 0.235$ and $\gamma^* = 1.853$. These parameter values ensure that the centers of mass of $\mathscr{P}$ and $\Omega_{\text{ex}}^{\gamma}$ $|\mu - \sigma|$ are positioned at a distance less than 1.2×10^{-9} from each other, specifically at the coordinates $(a^*, b^*) = (0.3045, -0.2442)$.

The domain of excitability, $\Omega_{\text{ex}}^{\gamma}$, is depicted in the (a, b) plane in Figure 3.5(a), while its corresponding pre-image, $\mathbf{f}^{-1}\left(\Omega_{\text{ex}}^{\gamma}\right)$, is shown in the $(A, \Delta A)$ plane in Figure 3.5(b), as defined by equation (3.21). The size and shape of $\Omega_{\text{ex}}^{\gamma}$ are influenced by the drug dose parameter γ. In Figure 3.5, the boundaries of both the image and pre-image are color-coded in panels (a) and (b), respectively, to clearly demonstrate how they correspond to each other.

A notable feature is that the curve defined by $b = -1$ in the (a, b) plane is mapped to a single point $(0, 0)$ in the $(A, \Delta A)$ plane. This mapping indicates that solving the inverse problem numerically is particularly challenging near this point, as evidenced by the plot of the Jacobian determinant values shown in Figure 3.4(a).

The transformation $\mathbf{f}^{-1}$, which acts as a change of variables, maps specific curves in the (a, b) plane to straight lines in the $(A, \Delta A)$ plane. For example, the curve $a = 0, b = a/(1-a)$ maps to the line $\Delta A = 0$, while the curve $a = 1/\gamma$ maps to the line $\Delta A = -A$. Consequently, the pre-image $\mathbf{f}^{-1}\left(\Omega_{\text{ex}}^{\gamma}\right)$ has a triangular shape in the $(A, \Delta A)$ plane, independent of the parameters β and γ. This finding is consistent with the analysis by Lachaud et al. where this region was empirically identified as shown in Figure 3C(iii) of their paper (Lachaud et al. 2022).

The triangular shape identified in $\mathbf{f}^{-1}\left(\Omega_{\text{ex}}^{\gamma}\right)$ mirrors the boundaries observed experimentally, emphasizing the robustness of the transformation in capturing the structural organization of myocyte responses. (Lachaud et al. 2022) suggested that this triangular region reflects the underlying variability in cellular electrophysiology, which is now theoretically explained through the interplay between the (a, b) parameters and the $(A, \Delta A)$ experimental data.

Additionally, the consistency of this triangular shape across different values of β and γ reinforces the fundamental relationship between the physiological characteristics of cardiomyocytes and their observable responses to drugs. The agreement between the mapped boundaries of the excitability domain and the empirically observed distributions highlights the predictive accuracy of the McKean model. This consistency provides further evidence that the heterogeneity observed by Lachaud et al., such as differences in the extent of APD changes across myocytes, can be systematically attributed to variations in the underlying model parameters.

The mapping also supports the conclusion that these parameter variations are essential for maintaining stable repolarization while allowing distinct cellular responses to pharmacological interventions.

Moreover, this framework not only aligns with but also extends the work of Lachaud et al. by demonstrating how these distributions can be quantitatively analyzed and predicted using the McKean model. The model offers additional insights, such as predicting how drug dose and pacing frequency influence the overall distribution of $(A, \Delta A)$, which Lachaud et al. observed qualitatively. This strengthens the conclusion that the electrophysiological heterogeneity documented in their study is a natural consequence of the structural and functional diversity captured within the excitability domain $\Omega_{\text{ex}}^{\gamma}$.

In addition to these visualisations, Figure 3.5 also includes histograms, Gaussian kernel density estimations, and simple regression lines for both the experimental dataset $\mathscr{D}$ and the solution set $\mathscr{P}$. These statistical tools are commonly employed in the analysis of experimental data and can be compared to similar analyses, such as Figure 3C(iii) in (Lachaud et al. 2022).

The mapping function $\mathbf{f}$, which is a calibrated solution to equations (3.16), and its inverse $\mathbf{f}^{-1}$, are both vector-valued functions with two inputs:

$$\mathbb{R}^2 \ni (A, \Delta A) \underset{\mathbf{f}^{-1}}{\overset{\mathbf{f}}{\rightleftarrows}} (a, b) \in \mathbb{R}^2. \tag{3.24}$$

This means that $\mathbf{f}$ and $\mathbf{f}^{-1}$ each take two arguments and return two outputs, corresponding to the $(A, \Delta A)$ and (a, b) planes. As a result, Figure 3.5 alone does not provide a clear graphical representation of how experimental data points in the $(A, \Delta A)$ plane correspond to parameter values in the (a, b) plane. To better visualise this relationship, Figure 3.6 separately plots the two components of $\mathbf{f} = (f_1, f_2)$, where $a = f_1(A, \Delta A)$ and $b = f_2(A, \Delta A)$. This approach allows for directly mapping physiological measurements to the corresponding model parameters. Specifically, it helps identify the value of a_i associated with a given data point $(A_i, \Delta A_i)$ in panel (a) and the value of b_i corresponding to the same data point in panel (b).

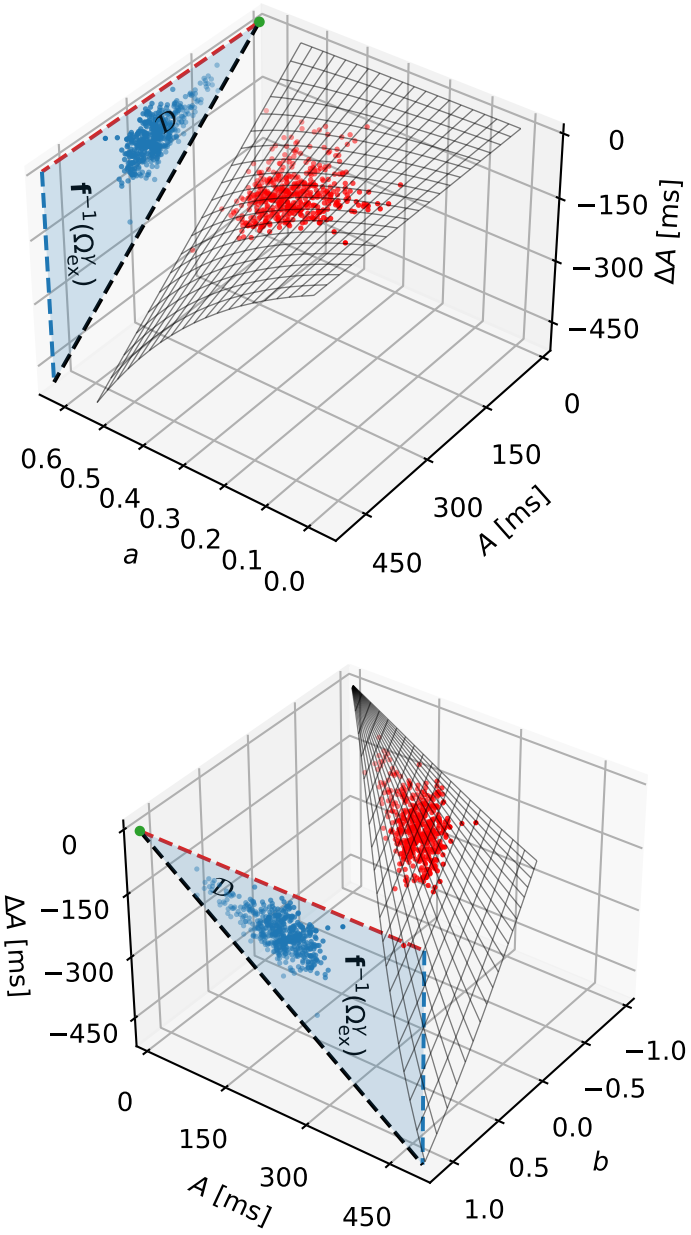

Figure 3.6: McKean model parameters a and b as functions of A and ΔA are shown as wire-frame surfaces in panels (a) and (b), respectively. The scatter plot of the experimental data $\mathscr{D}$ of (Lachaud et al. 2022) is shown as blue dots and its projections onto the surfaces $a(A, \Delta A)$ and $b(A, \Delta A)$ are shown as red dots. The figure is from our published paper (Simitev et al. 2023)

In Figure 3.6, the surfaces $a(A, \Delta A)$ and $b(A, \Delta A)$ are depicted as wireframes with grid lines representing iso-lines of the rectangular coordinates x and y, as defined in equation (3.13) from earlier sections. This visualisation emphasises a key point: an experimentally measured value of action potential duration A does not uniquely determine the cellular properties of a myocyte. Instead, a single value of A corresponds to a range of possible values for the parameters a and b, as shown in panels (a) and (b).

3.3.1 Parameter Interrelationships

The study conducted by (Lachaud et al. 2022) primarily concluded that the morphology of the action potential (AP) is preserved through specific relationships linking various ionic conductances, and that these interrelationships are crucial for maintaining stable repolarisation, despite significant inter-cell variability in individual conductances. This variability, they argued, also explains the differing sensitivities to ion channel blockers across cells.

To verify these conclusions and to explicitly determine these interrelationships, consider the curves:

$$\begin{aligned} &\mathscr{C}_a = (A, \Delta A)|_{(a=\text{ const },b)}, \quad \mathscr{C}_b = (A, \Delta A)|_{(a,b=\text{ const })}, \\ &\mathscr{C}_A = (a, b)|_{(A=\text{ const },\Delta A)}, \quad \mathscr{C}_\Delta A = (a, b)|_{(A,\Delta A=\text{ const })}; \end{aligned} \tag{3.25}$$

We have plotted a series of curves-depicting the first set in Figure 3.7(a) and the second set in Figure 3.7(b). These curves are designed to illustrate the necessary relationships among the internal model parameters that must be satisfied to keep the AP duration (APD) constant. For instance, a curve of the type $\mathscr{C}_A$ represents the specific interrelationship required among the parameters for a constant APD, with similar logic applied to the other types of curves. Upon examination, it becomes evident that the situation is more complex than (Lachaud et al. 2022) initially suggested. The interrelationship represented by $\mathscr{C}_A$ varies not only with the parameters but also with the particular APD value. For example, when $A = 0$ ms or for small values of A, the dependence on a is minimal, and there is an approximately linear relationship between a and b. However, as A increases, the relationship evolves and approaches $b = \frac{1}{1-a}$, which corresponds to the boundary of the excitability domain $\Omega_{\text{ex}}^{\gamma}$. Similar observations apply to the other grid lines depicted in Figure 3.7.

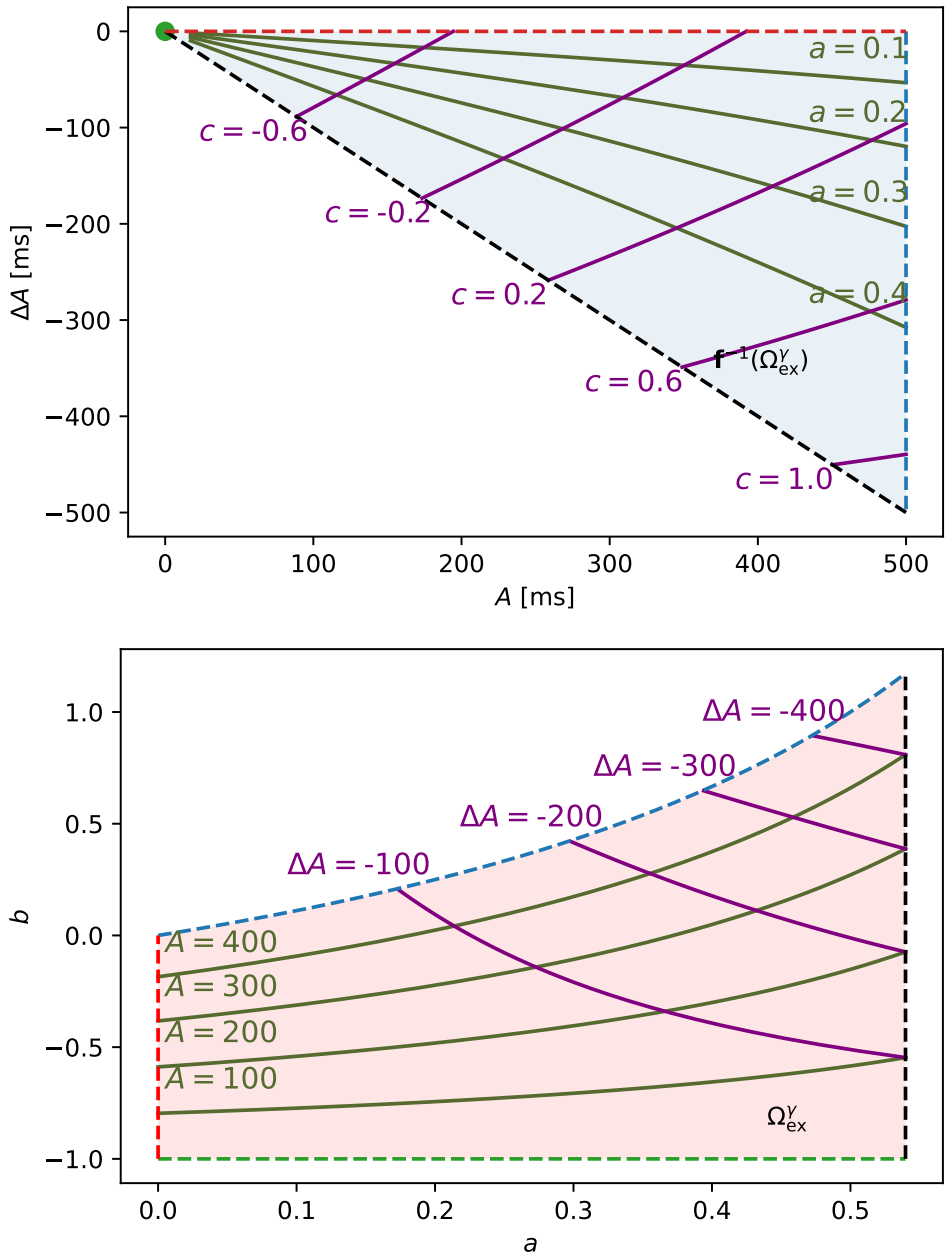

Figure 3.7: (a). Lines in the $(A, \Delta A)$ plane are obtained at constant values of a (olive green) and at constant values of b (purple) as labeled in the vicinity of each curve. (b). Lines in the (a, b) plane are obtained at constant values of A (olive green) and at constant values of ΔA (purple) as indicated in the vicinity of each curve. In both panels $\beta = 0.235$ and $\gamma = 1.853$. Other elements of the plot are similar to those described in the caption of Figure 3.5. The figure is from our published paper (Simitev et al. 2023)

It is worth noting that some of these interrelationships have already been derived in closed form in the earlier sections of this work. Specifically, the grid lines $\mathscr{C}_a$ and $\mathscr{C}_b$ shown in Figure 3.7(a) can be expressed using the general formula provided in equation (3.12a). Likewise, the curves $\mathscr{C}_A$ and $\mathscr{C}_{\Delta A}$ are derived from equation (3.22), which outlines the conditions necessary for solving the problem defined by equation (3.16) when evaluated for specific values of A and ΔA.

3.3.2 Dependence on Drug Concentration and Basic Cycle Length

The McKean model (McKean Jr 1970), while not closely aligned with the electrophysiological structures of myocytes, as acknowledged throughout this chapter, still offers significant advantages. One key strength of this approach lies in its ability to provide theoretical insights and make simple, yet effective, predictions. These predictions can be both economically generated and practically tested through experimental measurements. Figure 3.8(a) & (b), illustrate these predictions by showing how the experimental myocyte scatter cloud, denoted as $\mathscr{D}$, changes in response to variations in drug concentration Γ and basic cycle length B, respectively. To generate these predictions, it is assumed that a preliminary reference experiment has been conducted at fixed values of BCL and drug concentration, denoted as B^* and Γ^*, respectively. Using this reference data, the corresponding set of McKean model parameter values, $\mathscr{P}$, is estimated by solving equations (3.16) and (3.23). The reference values β^* and γ^* are determined simultaneously, as described in previous sections. For instance, the study continues to use the data from (Lachaud et al. 2022), where $B^* = 500$ ms and $\Gamma^* = 1\mu$M of Nifedipine, resulting in calibration values of $\beta^* = 0.235$ and $\gamma^* = 1.853$.

The calculated cell-specific values (a_i, b_i) for $i = 1, \ldots, N$ are then applied to the asymptotic expressions for APD and $\triangle$ APD. These are essentially the expressions from equation (3.16), but now with varying values of β and γ away from their reference values β^* and γ^*. The results are then converted to dimensional units using the scaling transformations:

$$\Gamma = \Gamma^* \frac{\gamma - 1}{\gamma^* - 1}, \quad B = B^* \frac{\beta}{\beta^*}. \tag{3.26}$$

As the drug dose decreases, the expected reduction in action potential duration also decreases. Conversely, when the drug dose Γ increases, the myocyte scatter cloud extends downward to increasingly negative values of ΔA, indicating that the drug progressively shortens the APD. Importantly, the pre-image of the excitability domain does not depend on Γ. Eventually, as the drug dose increases, a portion of the myocyte population drifts outside the excitability domain, making them non-excitable. The proportion of non-excitable cells can be

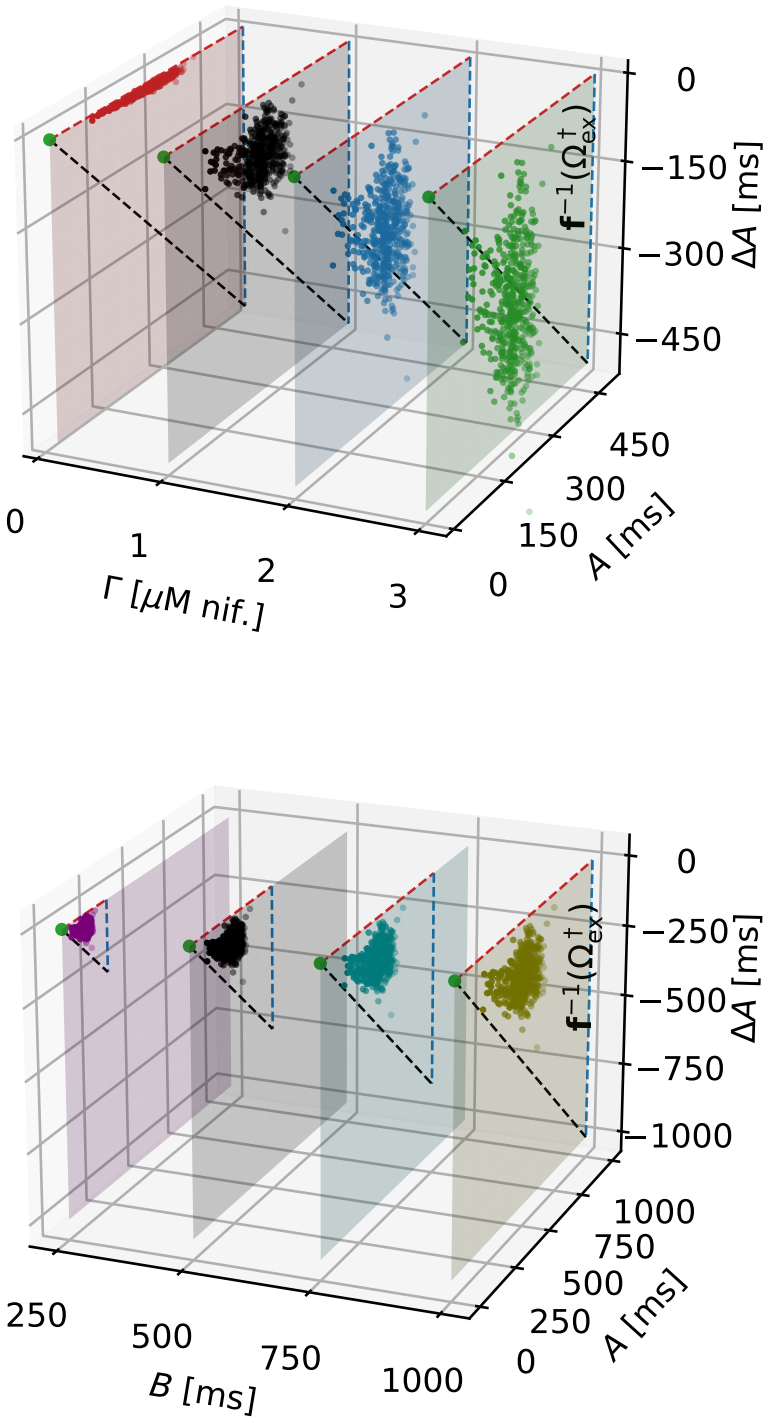

Figure 3.8: Prediction for the spread of the experimental data-point distribution $\mathscr{D}$ of (Lachaud et al. 2022) (black cloud) with the variation of the drug concentration Γ in (a), and the basic cycle length B in (b). The figure is from our published paper (Simitev et al. 2023)

estimated relative to the reference experiment using the following expression:

$$L = 1 - \frac{\int_{\Omega_{ex}^{\gamma}} \mathrm{d}S}{\int_{\Omega_{ex}^{\gamma^*}} \mathrm{d}S} = 1 - \frac{\log((\gamma-1)/\gamma)}{\log((\gamma^*-1)/\gamma^*)}, \tag{3.27}$$

Here, it is assumed that cell properties are uniformly distributed within their excitability domains. The "coefficient of loss" L represents the ratio of the planar area of $\Omega_{\text{ex}}^{\gamma}$ at drug concentration γ to the planar area of $\Omega_{\text{ex}}^{\gamma^*}$ at the reference concentration γ^*. Equation (3.27) can be reformulated in terms of drug concentration Γ by applying the change of variables described in equation (3.26).

When the basic cycle length B varies, the myocyte scatter cloud undergoes what appears to be a shape-preserving scaling transformation. As B increases, the cloud enlarges, and as B decreases, the cloud shrinks, while maintaining its overall shape, as shown in Figure 3.8(b). The preimage $\mathbf{f}^{-1}\left(\Omega_{\text{ex}}^{\gamma}\right)$ similarly changes size in response to B. The myocyte scatter cloud scales nonlinearly, as determined by equation (3.12a), and as illustrated in the restitution curve in Figure 3.3(b). This non-linear scaling leads to "saturation" for values of B larger than those shown in Figure 3.8(b).

3.3.3 Dose-response curves

From a control and medical intervention perspective, one of the most crucial challenges is determining the appropriate target drug concentration, denoted as Γ_T, that should be administered to a population of myocytes. The goal is to ensure that all myocytes in the population respond with an identical, "healthy" action potential under periodic stimulation. This desired action potential duration is referred to as A_T. Importantly, the target concentration Γ_T will vary for each cell within the population due to individual cellular differences.

To calculate Γ_T, we begin by assuming that a preliminary reference experiment has been conducted at fixed values of B^* and Γ^*. During this experiment, the parameters β^* and γ^* were calibrated, and the McKean model parameters were determined. Using this information, the target drug concentration Γ_T can be expressed as follows:

$$\Gamma_T = \frac{\Gamma^*}{\gamma^* - 1}\left(\frac{1}{a} - \frac{\exp\left(\tilde{b}\beta^*\right)\left(\exp\left(\tilde{b}A_T\beta^*/B^*\right) - 1\right)}{a\tilde{b}\left(\exp\left(\tilde{b}\beta^*\right) - 1\right)\exp\left(\tilde{b}A_T\beta^*/B^*\right)} - 1\right), \quad \tilde{b} = 1 + b \tag{3.28}$$

Note that the expression $\tilde{b} = 1 + b$ is essentially the same as equation (3.22), where the target value of the McKean "conductance" parameter is linked to the reference experiment's value by the relationship $a_T = \gamma_T a$. Additionally, scaling (3.26). is applied to convert these values to dimensional units.

However, the values of γ_T obtained from this expression must also satisfy two important constraints:

- $\gamma_T > 1$, which implies that $\Gamma_T > 0\mu$M (the minimal drug concentration that can be administered is $0\mu\mathrm{M}$),
- $\gamma_T < \frac{1}{a}$, ensuring that $a\gamma_T < 1$, a condition necessary for the cell to remain excitable.

Figure 3.9(a) illustrates these results by showing the target drug concentration values for Nifedipine, expressed in μM, with β^* and γ^* calibrated based on the data from Lachaud et al. (2022). The surface Γ_T is logarithmically transformed for better visualisation and is plotted as a function of the experimental biomarkers $(A, \Delta A)$ from the controlled experiment.

Figure 3.9(b) presents more conventional dose-response curves, which are computed using equation (3.16b) for each cell in the population, as well as for the "mean cell" within the population-defined as the cell with parameter values given before

$$(a^*, b^*) = (0.3045, -0.2442).$$

These predicted dose-response curves are compared with experimental data from (Himmel et al. 2012), which measured the dose-response to the same drug Nifedipine by observing changes in action potentials and field potentials in thin slices of rabbit ventricular tissue and rabbit Purkinje fibers.

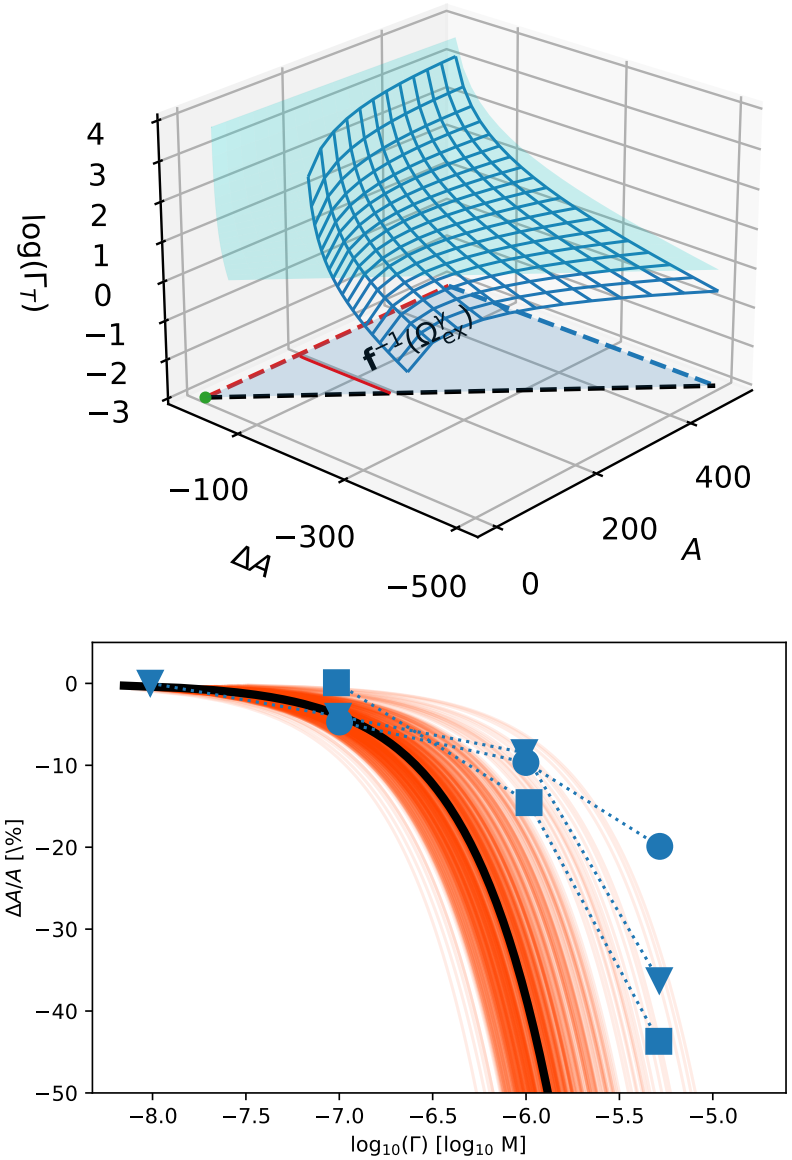

Figure 3.9: (a). Values Γ_T of the drug concentration (Nifedipine in μM) necessary to elicit action potentials with a prescribed duration $A_T = 180$ ms in a heterogeneous population of myocytes (blue wireframe surface). The solid red line is a projection of the line $\Gamma_T = 0\mu$M and the transparent aquamarine surface is $\Gamma_T = \Gamma^*(1-a)/(\gamma^*-1)/a$, both constraining the acceptable values Γ_T can take. (b). Dose-response curve of Nifedipine was computed using equation (3.16b). Thin semi-transparent lines are dose-response curves for individual cells in the myocyte population of (Lachaud et al. 2022), with the solid black line corresponding to the 'mean cell' with parameter values $(a^*, b^*) = (0.305, -0.244)$. Experimental data (blue dotted lines) from rabbit Purkinje fibre action potentials (triangles down) and ventricular action potentials (circles) and field potentials (squares) in thin-slice tissue preparations is also shown (data from Fig. 6B of (Himmel et al. 2012)). In both panels, McKean parameters (a, b) are calibrated to experimental data of (Lachaud et al. 2022) using $B^* = 500$ ms, $\Gamma^* = 1\mu$M nif. and $\beta^* = 0.235$ and $\gamma^* = 1.853$. The figure is from our published paper (Simitev et al. 2023)

Despite the significant differences between Himmel (Himmel et al. 2012) and Lachaud (Lachaud et al. 2022) experimental setups, the results demonstrate a remarkable agreement between the predicted and experimental dose-response curves. These differences include the following:

- The use of tissue slices in Himmel's experiments, as opposed to uncoupled cells in Lachaud's experiments. This variation in methodology is crucial, as it impacts how cellular responses are measured and interpreted.
- The types of measurements employed, with some cases involving field potentials. This difference in measurement technique can lead to variations in the observed data, yet the agreement between the results remains strong.
- The inherent variability in cellular properties, such as the comparison between Purkinje fibers and ventricular myocytes. This variation is significant because these different cell types can exhibit distinct responses to the same experimental conditions.
- Differences across animal populations, which introduce another layer of variability, as different animals may respond differently to the same stimuli.

This evident cellular heterogeneity has been a key motivation for our work in this PhD, particularly Chapters 3 and 5, driving the exploration of how different experimental conditions can still lead to consistent and reliable results.

Chapter 4

Regression Methods for Estimation of Parameters in Cardiac Ionic Current Models.

4.1 Introduction

4.1.1 Motivation

The motivation for this chapter arises from the need to enhance the accuracy and efficiency of parameter sensitivity analysis in cardiac electrophysiology models. Traditional approaches often rely on linear regression techniques, which may not fully capture the complexity of the relationships between ion channel conductances and physiological outputs like APD and calcium transients. However, by incorporating nonlinear transformations of input variables, such as squaring them, it is possible to better represent these complex relationships while still using a linear regression framework. This approach offers a more detailed understanding of model sensitivities without the increased computational burden associated with fully nonlinear regression techniques. Given the importance of accurate modelling for understanding cardiac arrhythmias and predicting drug responses, this work seeks to address these challenges by refining the methods used in parameter sensitivity analysis.

4.1.2 Aim

The aim of this chapter is to carry out a sensitivity analysis of cardiac electrophysiology models by employing linear regression techniques that include nonlinear transformations of input variables. This approach seeks to enhance the predictive power and accuracy of the models by better capturing the complex relationships between ion channel conductances and key physiological biomarkers. Additionally, this method will be applied to assess drug responses, thereby demonstrating its utility in predicting the effects of pharmacological interventions and contributing to the development of more effective treatments for cardiac conditions.

4.2 Method

4.2.1 Baseline Cardiac Action potential Model from Luo and Rudy (1991)

Several models of the AP ventricular myocytes have been developed and extensively discussed in the literature. The LR1 (Luo and Rudy 1991), developed to simulate the action potential of ventricular myocytes in guinea pigs. It has been a foundational contribution to the field of cardiac electrophysiology. It is known for its comprehensive representation of the depolarisation and repolarisation phases of the cardiac AP. This model incorporates several key ionic currents, including fast sodium (Na^+), L-type calcium (Ca^{2+}), and various potassium (K^+) currents such as the inward rectifier K^+ current and the delayed rectifier K^+ currents. It also accounts for the $\mathrm{Na}^+ - \mathrm{K}^+$ pump, the $\mathrm{Na}^+ - \mathrm{Ca}^{2+}$ exchanger, and background Na^+, Ca^{2+}, and K^+ currents.

LR1 model is characterised by its ability to replicate key aspects of ventricular myocyte electrophysiology, such as action potential duration, shape, and the ionic basis of these phenomena. With a focus on the interaction between depolarisation and repolarisation processes, the model uses a series of differential equations to describe the time-dependent and voltage-dependent behaviour of ionic currents and concentrations. This model's rigorous structure and detailed biophysical basis make it particularly valuable for simulating the effects of pharmaco-

logical agents and for studying the mechanisms of arrhythmogenesis (Luo and Rudy 1991). Its balance between complexity and computational efficiency has made it a widely used tool for exploring the fundamental dynamics of cardiac APs, making it an essential reference in both theoretical and applied cardiac electrophysiology research.

4.2.2 Model Inputs and Outputs

In this chapter, we utilised LR1 model (Luo and Rudy 1991) to investigate the effects of varying specific ionic conductances on AP characteristics of ventricular myocytes in guinea pigs. Six key ionic conductances were selected, and a population of models was generated by randomly varying these conductances. Importantly, all other parameters in the LR1 model, apart from those listed in Table 4.1, were left unchanged from the values specified in the original LR1 publication (Luo and Rudy 1991). This ensures that the only modifications to the reference model are the changes in conductances as described in this section. The baseline conductance values were scaled using multiplicative factors, where each factor was randomly selected from a log-normal distribution with a median of 1. This distribution ensured that the likelihood of a conductance being doubled was the same as the likelihood of it being halved.

The scaling of conductances can be expressed mathematically as:

$$G_i' = p_i \cdot G_{i,\text{baseline}}, \tag{4.1}$$

where:

- G_i' is the scaled conductance for the i^{th} ionic current,
- p_i is the scale factor for the i^{th} conductance, selected from a log-normal distribution,
- $G_{i,\text{baseline}}$ is the baseline value of the i^{th} conductance from the original LR1 model.

For simplicity, we will use the symbols P_{Na}, P_{si}, P_{K1}, P_{K}, P_{Kp}, and P_{B} to represent the scaled conductances for sodium (G_{Na}), slow inward calcium (G_{si}), inward rectifier potassium (G_{K1}), delayed rectifier potassium (G_{K}), plateau potassium (G_{Kp}), and background currents (G_{B}), respectively. The scale factors p_i denote the multiplicative adjustment applied to each baseline conductance value. A comprehensive list of the varied conductances and their baseline values, as provided in the original published model (Luo and Rudy 1991), is presented in Table 4.1. For each set of conductances, we simulated the resulting APs. The simulations were

Parameter	Definition	Baseline value
G_{Na}	Maximal Na^+conductance	$16\mathrm{mS/cm^2}$
G_{si}	Maximal slow-inward $\left(\mathrm{Ca}^{2+}\right)$ conductance	$0.09\mathrm{mS/cm^2}$
G_{K1}	Inward rectifier current	$0.6047\mathrm{mS/cm^2}$
G_{K}	Delayed rectifier current	$0.282\mathrm{mS/cm^2}$
G_{Kp}	Maximal plateau K^+conductance	$0.0183\mathrm{mS/cm^2}$
G_{B}	Background conductance	$0.03921\mathrm{mS/cm^2}$

Table 4.1: List of ionic conductances scaled in the LR1 model simulations in this chapter. All other parameters are unchanged from their baseline values in the original publication (Luo and Rudy 1991).

conducted using the (LR1) model using MATLAB (R2019B, The MathWorks, Inc., USA), with code obtained from the CellML repository (www.cellml.org) (Miller et al. 2010). Throughout these simulations, the following key biomarkers were recorded:

- **Resting Membrane Potential (Vrest)**: The voltage of the cell membrane when it is not generating an AP.
- **Peak Voltage (Vpeak)**: The maximum voltage reached during the AP.
- **Action Potential Duration (APD90)**: The time interval between the beginning of an AP and 90% repolarisation from the maximum voltage (Vpeak).

These biomarkers were chosen as they provide critical insights into the electrical behaviour of the cell under different conditions of ionic conductance, allowing for a deeper understanding of the mechanisms driving cardiac APs.

Simulations were conducted with a large number of sets of randomly generated parameters to create input and output matrices. Each input matrix, denoted as $\mathbf{X}$, is a numerical representation of the scaled ionic conductances. It has dimensions $n \times q$, where n represents the number of randomly generated parameter sets (or models), and q denotes the number of varied scaling factors (six in this case). Specifically, the entry X_{ij} of $\mathbf{X}$ corresponds to the scaled value of the j^{th} conductance for the i^{th} model.

The output matrix, denoted as $\mathbf{Y}$, contains the key biomarkers recorded from the simulations. It has dimensions $n \times m$, where n is the number of models, and m corresponds to the number of output variables recorded (three: V_{rest}, V_{peak}, and APD90). Specifically, the entry Y_{ij} of $\mathbf{Y}$ represents the j^{th} biomarker value (e.g., V_{rest}, V_{peak}, or APD90) recorded for the i^{th} model.

4.2.3 Performing OLS Regression

Ordinary least squares (OLS) regression was employed to analyze the relationship between the input conductances and the output biomarkers. The regression was performed using the 'LinearRegression' implementation from the 'scikitlearn' library. The objective of the OLS procedure was to compute a $q \times m$ matrix of regression coefficients, $\mathbf{B}$, that enables prediction of outputs for new input sets. Specifically, OLS determines $\mathbf{B}$ such that the predicted output matrix $\mathbf{Y}_{\text{predicted}} = \mathbf{XB}$ closely approximates the actual output matrix $\mathbf{Y}$.

The regression coefficients $\mathbf{B}$ are calculated using the standard closed-form formula:

$$\mathbf{B} = \left(\mathbf{X^T X}\right)^{-1} \mathbf{X^T Y}, \tag{4.2}$$

where:

- $\mathbf{X^T}$ is the transpose of the input matrix $\mathbf{X}$.

- $\mathbf{X^T X}$ is a $q \times q$ matrix representing the pairwise correlations between the input variables (conductances).

- $\left(\mathbf{X^T X}\right)^{-1}$ is the inverse of this square matrix, which exists if $\mathbf{X}$ has full rank.

For this study, the parameters were varied independently, and a large number of simulations were conducted to ensure robust estimation of $\mathbf{B}$. Since the number of simulations, n, exceeded the number of input variables, q, the input matrix $\mathbf{X}$ had full rank. This guaranteed that $\mathbf{X^T X}$ was invertible, avoiding issues of multicollinearity and ensuring reliable computation of the regression coefficients.

The dimensionality of the matrices is as follows:

- $\mathbf{X}$: An $n \times q$ matrix, where n is the number of simulations and q is the number of input variables.

- $\mathbf{Y}$: An $n \times m$ matrix, where m is the number of output variables.

- $\mathbf{X^T X}$: A $q \times q$ matrix, representing the correlations among input variables.

- $\mathbf{B}$: A $q \times m$ matrix, containing the regression coefficients that describe how the inputs influence each output.

This approach ensures a rigorous and interpretable estimation of the relationship between ionic conductances and cardiac action potential biomarkers. By leveraging the robustness of OLS regression and the large number of simulations, the results provide a reliable framework for sensitivity analysis.

4.2.4 Standardisation of Data for Regression Analysis

Before conducting the regression analysis, the values in both the input and output matrices were mean-centred and normalised using their respective standard deviations. Specifically, each element in the matrices was transformed according to the formula:

$$x_{\text{new}} = \frac{x_{\text{orig}} - \mu_x}{\sigma_x}, \tag{4.3}$$

where x_{orig} represents the original value, μ_x is the mean, and σ_x is the standard deviation of each column. This standardisation process ensured that the variables were on a comparable scale, which is essential for accurate regression analysis.

Given that the random scale factors in the input matrices followed a log-normal distribution, most of these values were log-transformed prior to calculating the mean (μ) and standard deviation (σ). This transformation was necessary to approximate a normal distribution, facilitating better regression performance.

In the output matrix, the Action Potential Duration (APD90) distribution was right-skewed. The histograms showing the distributions of the three output variables APD90, Vrest, and Vpeak are shown in Figure 4.1. These visualisations provide insight into the initial data distributions and the effects of the applied transformations. To address this skewness, APD90 values were log-transformed before the regression analysis and then re-transformed back into their original units for clarity when displaying the results in figures. By contrast, Vrest and Vpeak were approximately normally distributed, as confirmed by visual inspection of their histograms. Consequently, these variables were not log-transformed but were simply standardised by mean-centring and scaling.

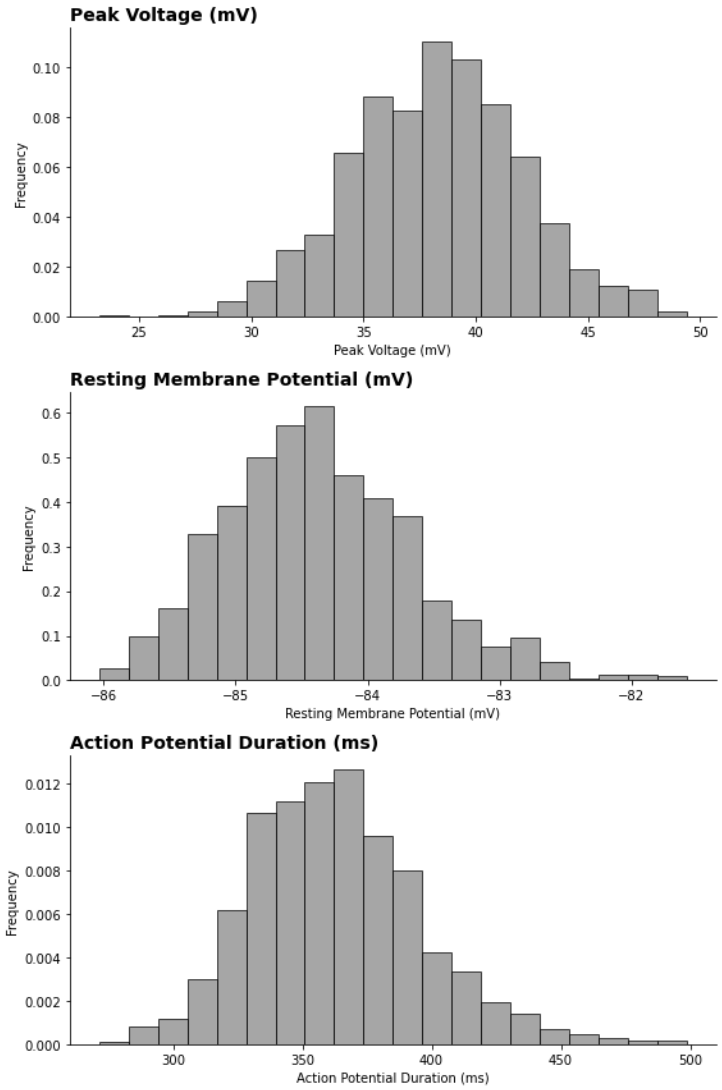

Figure 4.1: This figure presents histograms illustrating the distributions of the three output variables: APD90, Vrest, and Vpeak. The APD90 distribution shows right-skewness, addressed through log transformation prior to regression analysis, while Vrest and Vpeak follow approximately normal distributions and were only standardised without log transformation. These histograms offer a visual representation of the initial data distributions and the effects of the transformations applied to the variables.

4.3 Results

4.3.1 Action Potential Variability

Figure 4.2 presents the time series of AP traces generated by randomly varying the six maximum ionic conductances in LR1 model. The scaling factors for these conductances (P_{Na}, P_{si}, P_{K1}, P_{K}, P_{Kp}, and P_{B}) were applied to the baseline values of the conductances (G_{Na}, G_{si}, G_{K1}, G_{K}, G_{Kp}, and G_{B}). The scaling factors were standardised to ensure they followed a consistent range for comparison. Random variations in these conductances resulted in changes

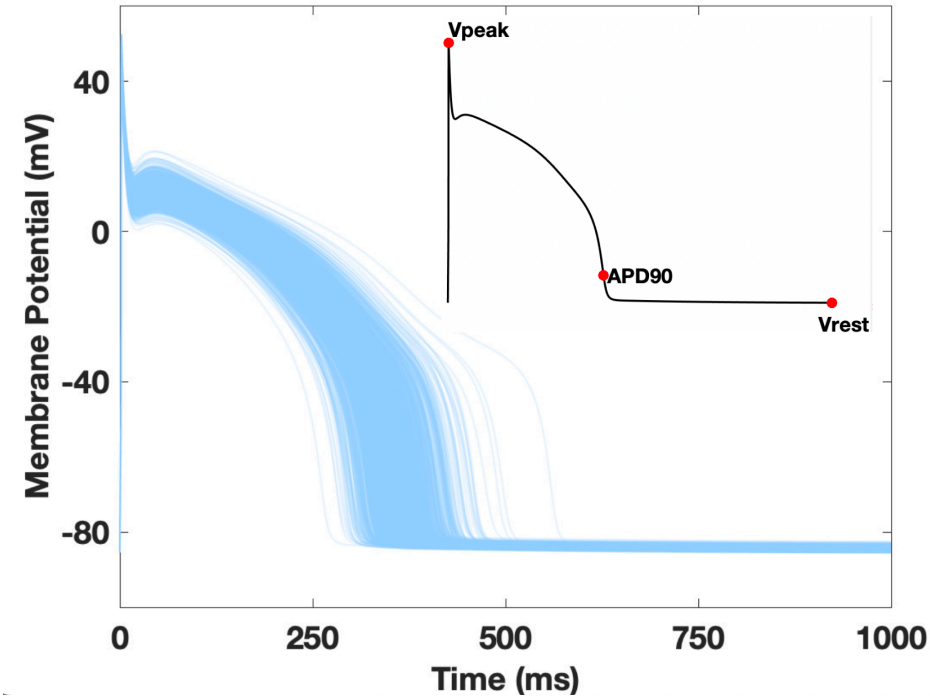

Figure 4.2: Time series of action potentials generated from the initial population of 1000 models based on the LR1 model (Luo and Rudy 1991). The figure illustrates the variation in APs across the population, showcasing the diversity in AP behaviour among the model variants. In the top right corner, the baseline model's AP trace is highlighted, with key outputs marked, including APD90, Vrest, and Vpeak.

to APD90, Vrest, and Vpeak. Depending on the specific combination of conductance values in each trial, these outputs could increase or decrease. This process was repeated multiple times, generating input and output matrices with $n = 1000$ rows (representing the number of trials), $q = 6$ columns for the six varied conductances, and $m = 3$ columns for the three output variables (APD90, Vrest, and Vpeak).

4.3.2 Regression and Predictive Model

The OLS regression was performed on the input matrix $\mathbf{X}$ and the output matrix $\mathbf{Y}$. This regression produced a 6×3 matrix of regression coefficients, from 6 inputs (scaled conductances) and 3 outputs (biomarkers). This matrix is denoted as $\mathbf{B}$, and provides an empirical model for predicting the outputs based on new input parameters. The predicted output, $\mathbf{Y}_{\text{predicted}}$, can be obtained using the equation:

$$\mathbf{Y}_{\text{predicted}} = \mathbf{X} \times \mathbf{B}, \tag{4.4}$$

Figure 4.3 displays scatterplots comparing the 'actual' outputs (calculated by numerically integrating the LR1 model differential equations) against the predicted outputs obtained from the OLS regression model. The plots show that the empirical model performs highly accurately, with R^2 values ranging from 0.97 to 0.99 across the three output variables. These results demonstrate that, despite the underlying nonlinearities of the LR1 model, the simplified linear model based on OLS regression is a reliable predictor of the outputs.

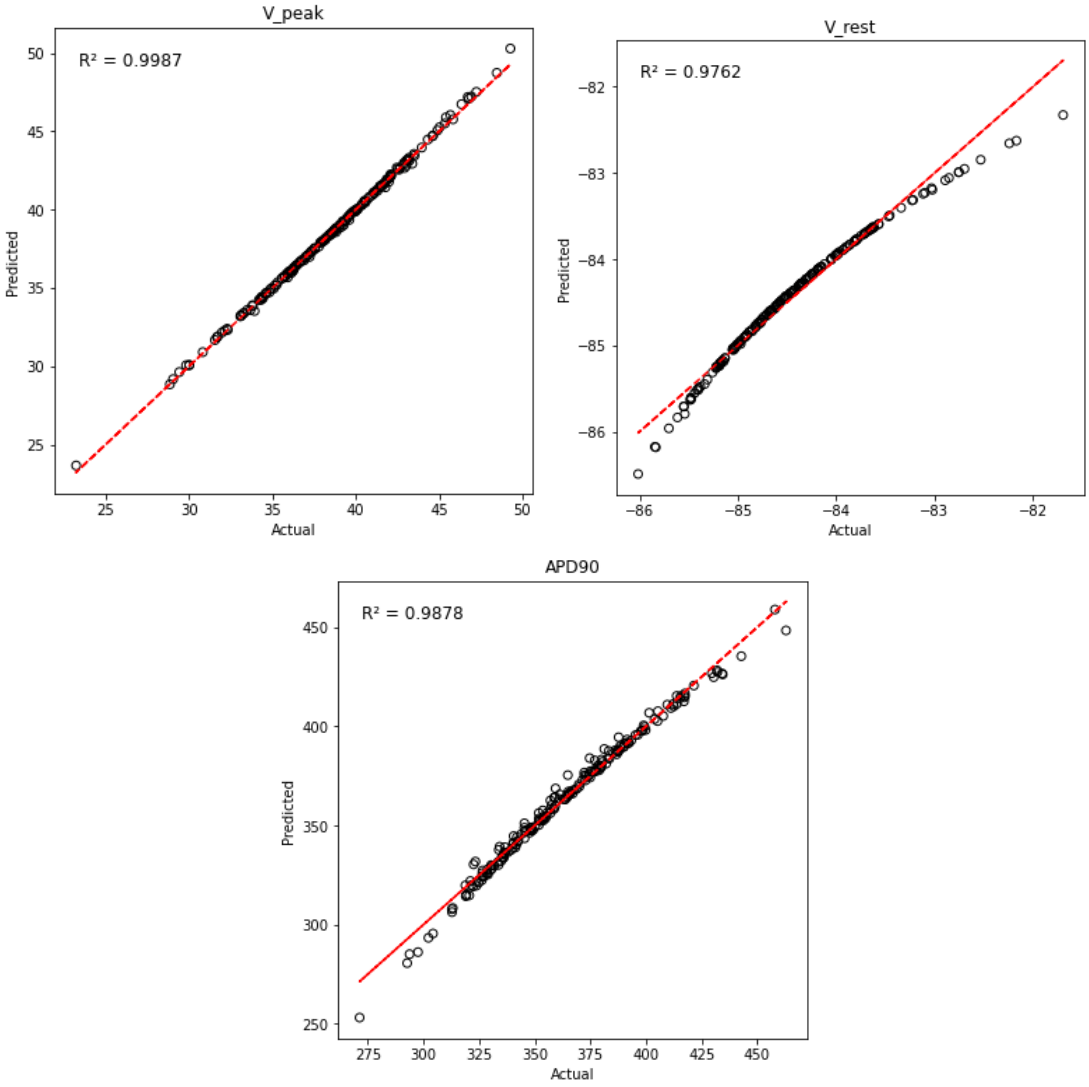

Figure 4.3: This figure shows scatterplots comparing the actual outputscalculated by numerically integrating the LR1 model's differential equationswith the predicted outputs generated from the OLS regression model. The close alignment of data points along the 45-degree line, together with R^2 values between (0.97 and 0.99), indicates a strong agreement between the actual and predicted values for the three output variables (a) Vpeak, (b) Vrest, and (c) APD90, respectively. Despite the nonlinearity inherent in the LR1 model, the OLS regression model serves as a highly accurate predictor of the outputs.

4.3.3 Interpretation of Regression Coefficients

The regression coefficients in the $\mathbf{B}$ matrix provide insights into how variations in the six input conductances affect the three output variables. Each column of the matrix corresponds to a specific output (APD90, Vrest, or Vpeak), while each row represents the influence of a particular conductance. Analysing these coefficients allows for an understanding of the relative contributions of each conductance to the outputs.

Figure 4.4 illustrates the values of the $\mathbf{B}$ matrix, highlighting how changes in each ionic conductance impact the three output variables. This plot is analogous to Figure 3A in the study by Sobie, published in (Sobie 2009), where Sobie used Partial Least Squares (PLS) regression with the NIPALS algorithm (Geladi and Kowalski 1986). The visualisation of the regression coefficients provides a compact and intuitive representation of the sensitivity of the outputs to variations in the conductances. Although the effects of varying each ionic conductance could be determined by adjusting parameters one at a time, It is inefficient for complex models involving many ion-transport mechanisms. In contrast, the OLS regression technique allows for rapid and systematic evaluation of how changes in multiple parameters affect the model outputs simultaneously. Additionally, the procedure provides a straightforward graphical representation of the relative effects of each parameter, enabling a clear understanding of which conductances have the greatest influence on the outputs. This is particularly useful in models such as LR1, where numerous mechanisms interact to influence the overall behaviour of the AP.

4.4 Application I: Using OLS regression to Predict Drug Response

The OLS regression is employed in this study to create an empirical model that predicts how the output biomarkers, particularly APD90, change in response to modifications in ionic conductances, both before and after the application of a drug. To evaluate the accuracy of this empirical model, we compare the predictions to direct simulation results.

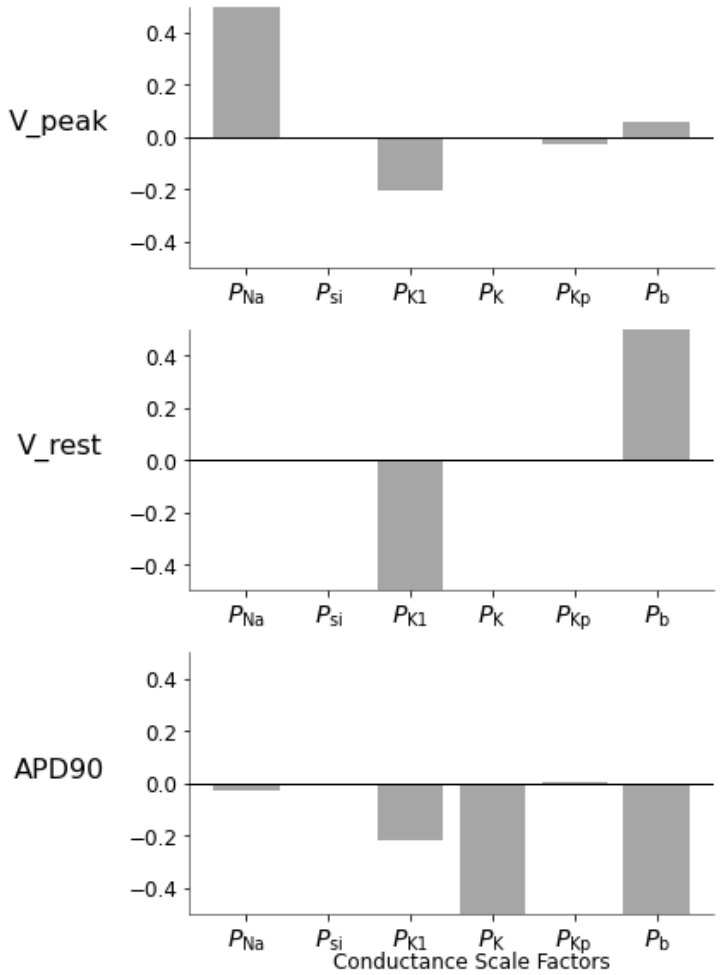

Figure 4.4: This figure shows the values of the $\mathbf{B}$ matrix, representing the regression coefficients that quantify how changes in each ionic conductance affect the three output variables. This figure mirrors Figure 3A in (Sobie 2009), which used Partial Least Squares (PLS) regression, but here OLS regression is applied. The chart offers a clear visualisation of how sensitive the outputs are to variations in different conductances, providing an intuitive representation of the model's behaviour. The y-axis values are unitless because they represent the regression coefficients from the linear regression model. The regression coefficients are derived from relationships between unitless standardized variables; inputs and outputs, thus the y-axis does not carry any physical units. This is consistent with the mathematical properties of standardized regression.

4.4.1 Method

We begin with the assumption that the output biomarkers, such as APD90, are functions of the ionic conductances (represented by scaling factors $\mathbf{P}$) in the LR1 model. The relationship between $\mathbf{P}$ and the outputs $\mathbf{A}$ can be expressed as:

$$\mathbf{A} = f(\mathbf{P}), \tag{4.5}$$

where:

- $\mathbf{A}$ is the matrix of output biomarkers (e.g., APD90)
- $\mathbf{P}$ is the matrix of the scaling factors of the six conductances such as G_{Na}, G_{K}, etc.).
- f represents the function that maps the conductances to the biomarkers, which in the LR1 model is a set of nonlinear differential equations.

Next, we investigate the effects of altering ionic conductances on AP dynamics in a population of 1000 cells simulated using the LR1 model. Specifically, this study focuses on how reducing the conductance of G_{K} (potassium conductance) by 30% influences APD90. Potassium currents, in general, play a crucial role in the repolarization phase of the AP. By reducing G_{K} the model investigates how a decrease in the overall potassium conductance affects the repolarization process and APD90. Since potassium currents are responsible for returning the cell membrane potential back to its resting state, any reduction would slow down this process, leading to AP prolongation. Reducing G_{K} affects multiple potassium currents, which can cause delayed repolarization and extend APD90 (Maleckar et al. 2009). Since APD90 is a key marker of electrical activity in the heart, modifying G_{K} is a straightforward way to study changes in repolarization dynamics and simulate drug effects that target potassium channels. Many experimental studies and clinical trials have shown that I_{Kr} blockers (such as Dofetilide, and others) affect cardiac repolarization by reducing the potassium current, making it a common target in cardiac models. The reduction of by 30% is chosen to reflect the drug's pharmacological effect observed in these studies in particular the study in (Lachaud et al. 2022).

4.4.1.1 Applying the Drug's Effect

The drug effect is assumed to act on the potassium current G_{K} which we aim to reduce by 30%. This action was implemented by multiplying the scaling factors of G_{K} in the matrix of conductances $\mathbf{P}$ by 0.7, representing a 30% reduction in the potassium current.

4.4.1.2 Construct the Drug Action Matrix

The drug's action is mathematically represented by a matrix Γ that modifies the conductance of G_{K}, while keeping other conductances unchanged. The matrix Γ is constructed as follows:

$$\Gamma = \begin{pmatrix} 1 & 0 & 0 & 0 & 0 & 0 \\ 0 & 1 & 0 & 0 & 0 & 0 \\ 0 & 0 & 1 & 0 & 0 & 0 \\ 0 & 0 & 0 & 1+\gamma & 0 & 0 \\ 0 & 0 & 0 & 0 & 1 & 0 \\ 0 & 0 & 0 & 0 & 0 & 1 \end{pmatrix}, \tag{4.6}$$

where $\gamma = -0.3$ represents a 30% reduction in G_{K}. The notation γ in this chapter differs from its use in Chapter 3. In Chapter 3, γ represents a multiplicative factor applied to the McKean model parameter a, capturing the effect of drug action in a simplified mathematical framework. In Chapter 4, γ denotes a relative change (-30%) in the potassium conductance G_{K}, directly modeling the pharmacological impact on ionic currents in the LR1 model.

4.4.1.3 Modify the Conductance Vector $\mathbf{P}$

To apply the drug's effect, the matrix $\mathbf{P}$ is multiplied by the drug action matrix Γ, leading to a new vector of scaling factors $\mathbf{P}^D$, where the conductance G_{K} is reduced by 30% :

$$\mathbf{P}^D = \Gamma\mathbf{P} = \begin{pmatrix} \mathbf{P}_{\mathrm{Na}} \\ \mathbf{P}_{\mathrm{si}} \\ \mathbf{P}_{\mathrm{K1}} \\ (1+\gamma)\mathbf{P}_{\mathrm{K}} \\ \mathbf{P}_{\mathrm{Kp}} \\ \mathbf{P}_{\mathrm{B}} \end{pmatrix} = \begin{pmatrix} \mathbf{P}_{\mathrm{Na}} \\ \mathbf{P}_{\mathrm{si}} \\ \mathbf{P}_{\mathrm{K1}} \\ 0.7\mathbf{P}_{\mathrm{K}} \\ \mathbf{P}_{\mathrm{Kp}} \\ \mathbf{P}_{\mathrm{B}} \end{pmatrix}. \tag{4.7}$$

The new matrix $\mathbf{P}^D$, which contains the drug-modified conductances.

4.4.1.4 Simulate the Drug's Effect

After modifying the conductances, the APs are simulated using the new conductance values $\mathbf{P}^D$ for 1000 cells. The simulation generates new APs for all cells in the population, reflecting the impact of the drug on the electrical activity of the heart cells.

4.4.1.5 Obtain the New APD90

We carried out a protocol to simulate the effects of reducing G_{K} by 30% on the AP in a population of 1000 virtual cardiac cells using the LR1 model. The protocol generates 30 action potentials per cell, extracts the last two APs, and records them for further analysis. In this simulation protocol, the basic cycle length (BCL) is set to 1000 milliseconds (ms), meaning that the time between consecutive stimuli is 1000 ms, equivalent to a heart rate of 1 Hz (i.e., 60 beats per minute). The protocol involves delivering a total of 30 stimuli to each virtual cardiac cell over a period of 30 seconds. Each stimulus elicits an action potential (AP), and the simulation records the behaviour of the membrane voltage and other variables in response to each stimulus. The LR1 model functions are obtained from CellML repository (www.cellml.org), (Miller et al. 2010). These functions calculate voltage, states, and other variables using a differential equation solver (ODE) across the time course of the simulations. From the the AP traces we calculate APD90, by determining the time it takes for the membrane potential to repolarize to 90% of the difference between the peak voltage and the resting membrane potential. This value was measured for each model variant to assess the effects of reducing potassium conductance on APD90.

4.4.1.6 Data Splitting and Regression

The data was split into 80% training data and 20% test data. The training data was used to fit the OLS regression model. The same regression techniques, used in the previous section, were applied. In OLS regression, the goal is to find a linear relationship between the conductances and the biomarkers. This can be written as:

$$\mathbf{A} = \mathbf{PB}. \tag{4.8}$$

The regression coefficient matrix $\mathbf{B}$ represents the effect each conductance has on the output biomarkers. The OLS regression algorithm calculates the regression coefficient matrix $\mathbf{B}$, which minimises the difference between the predicted and actual biomarker values by minimising the sum of squared residuals. Mathematically, OLS solves the following optimisation problem:

$$\min_{\mathbf{B}} \|\mathbf{A} - \mathbf{PB}\|^2, \tag{4.9}$$

where $\|\cdot\|$ represents the Euclidean norm.

4.4.1.7 Predicting the Biomarkers After Drug Application

After the drug is applied, we modify the conductances of the potassium current (G_{K}) by 30% reduction. This results in a new matrix of conductances $\mathbf{P}^D$, where the values of G_{K} have been scaled by 0.7:

$$\mathbf{P}^D = \Gamma\mathbf{P}. \tag{4.10}$$

The OLS regression model is then used to predict the new biomarker values $\mathbf{A}^D$ after the drug application. The prediction is made using the previously calculated regression coefficients B :

$$\mathbf{A}^D_{\text{pred}} = \mathbf{P}^D\mathbf{B}. \tag{4.11}$$

This gives us the predicted values for APD90, after the drug has been applied. By applying these steps, we simulate the drugs effect on the LR1 model and assess the changes in APD90.

4.4.1.8 Evaluating the Model's Accuracy

The predicted values $\mathbf{A}^D_{\text{pred}}$ are compared against $\mathbf{A}^D_{\text{sim}}$; the actual values obtained from the LR1 model simulations after the drug application. This is done using scatter plots, where the predicted APD90 values are plotted against the actual APD90 values, along with a 45-degree line (indicating perfect prediction). In addition, the R-squared values are used to assess how well the linear OLS regression model approximates the changes induced by the drug in the more complex nonlinear LR1 model.

4.4.2 Results

4.4.2.1 Effects of the Drug on Action Potentials

The application of the drug resulted in significant changes in APD90 across the population of simulated cells. Figure 4.5 shows the AP traces for 500 randomly selected cells before and after the drug was applied. The blue traces represent the APs prior to the drug application, while the red traces represent the APs after the 30% reduction in G_{K}. The figure clearly illustrates that the majority of cells exhibited a significant prolongation of APD90, which corresponds to delayed repolarisation. However, a subset of very few cells displayed different behaviour, failing to fully repolarise and experiencing a plateau in their AP. Also, a small group of cells showed a decrease in APD90, indicating varying responses to the drug. This variation in response aligns with observations from an experimental study in (Lachaud et al. 2022), where drugs targeting potassium currents caused heterogeneous effects within a population which suggests that the drug's effects might depend on the specific ionic conductance profile of each cell. Figure 4.6 presents a scatter plot comparing the baseline APD90 values (before drug ap-

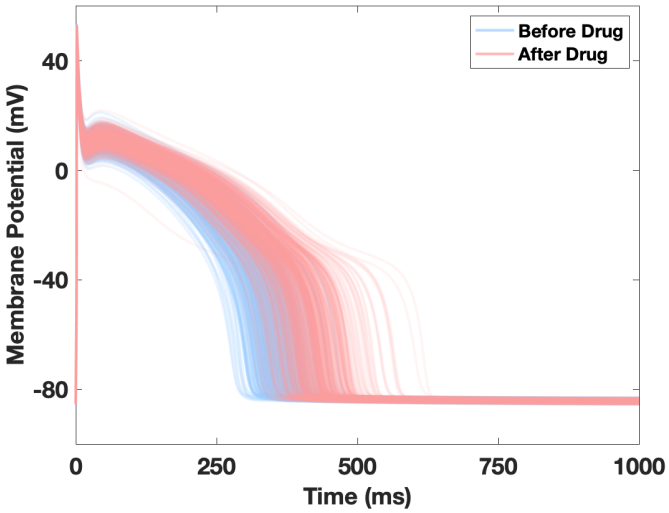

Figure 4.5: This figure displays AP traces of 500 randomly selected cells before and after the drug application. The blue traces represent the APs before the drug application, while the red traces show the APs after reducing G_{K} by 30%. As observed, the drug caused a significant prolongation of APD90 in the majority of the cells, although some cells showed plateauing and failed to repolarise. Some cells exhibited a slight decrease in APD90, indicating varying responses within the population. This result is consistent with different drug responses observed in experimental studies such as (Lachaud et al. 2022).

plication) with the change in APD90, denoted as ΔAPD90, which represents the difference in APD90 before and after the drug application. The scatter plot demonstrates that for most cells, APD90 increased following the reduction in G_{K}, consistent with the AP prolongation observed in the traces.

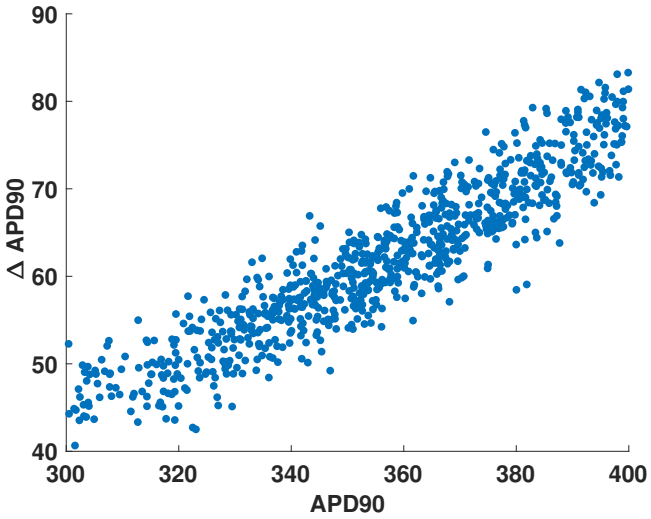

Figure 4.6: This figure illustrates the scatter plot of APD90 before the drug application against Δ APD90 (the difference in APD90 before and after the drug). The data points show that, for the majority of cells, APD90 increased significantly following the reduction in G_{K}. However, the cells exhibited different behaviour are excluded from this figure.

4.4.2.2 Predicting Drug-Induced APD90 Changes

To evaluate the performance of the OLS regression model in predicting the drug-induced changes in APD90, we compared the predicted APD90 values to the actual values obtained from direct LR1 model simulations after the drug was applied. Figure 4.7 presents a scatter plot comparing the simulated APD90 values to the predicted APD90 values. The 45-degree line in the plot indicates good agreement between the simulation and prediction.

4.5 Application II: OLS Regression Analysis with Nonlinear Interactions

The primary aim of this study is to establish the relationship between various ionic conductance parameters and a set of cardiac biomarkers using OLS linear regression models that incorporate nonlinear terms. We focus on modelling the relationships between multiple ionic conductances, such as sodium, potassium, and calcium conductances, and key cardiac biomark-

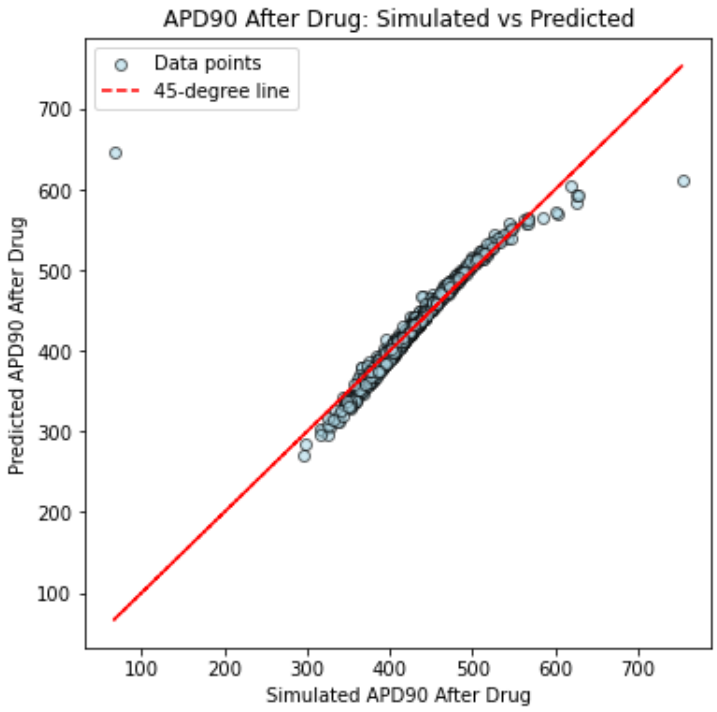

Figure 4.7: This figure compares the APD90 values obtained from direct LR1 model simulations after drug application calculated by numerically integrating the LR1 model differential equations vs the predicted APD90 values from the OLS regression model. Each data point represents a cell, and the 45-degree line indicates perfect agreement between simulation and prediction. The close alignment of the data points along this line demonstrates the high accuracy of the OLS regression model in predicting the drug-induced changes in APD90. Despite the underlying non-linearities in the LR1 model, the linear regression model effectively captured the relationship between conductance changes and APD90.

ers. These biomarkers are critical indicators of cardiac electrophysiology, providing insight into the function and behaviour of cardiac cells. By constructing regression models for each conductance, we aim to identify the most important factors influencing them and explore how nonlinear interactions between these biomarkers enhance the explanation of the underlying physiological processes. The use of stepwise regression allows us to refine these models by selecting the most significant predictor variables, providing a comprehensive understanding of how various ionic conductances are regulated and interact with key cardiac biomarkers.

4.5.1 Nonlinear Terms in a Regression Model

Incorporating nonlinear terms - such as squared predictor, square root of a predictor, or interaction terms (multiplication of 2 predictors) - into a regression model can provide several key benefits, especially when dealing with complex real-world data. One of the primary advantages is the ability to capture complex relationships. In many cases, the relationship between

an independent variable and the dependent variable is not strictly linear; it may be curved or change at different levels. By including nonlinear terms like squares of the inputs, the model can better represent these dynamics, offering a more accurate depiction of how changes in the predictor affect the outcome.

Nonlinear terms also improve the overall model fit. By accounting for these complex relationships, the model reduces bias, leading to lower residuals, a smaller root mean square error (RMSE), and a higher R^2 value. This means the model can explain more of the variation in the dependent variable. Additionally, nonlinear terms allow for the uncovering of interactions between variables and can significantly enhance the model's accuracy. Nonlinear relationships between variables are common in biological systems, and by capturing these interactions, the model becomes more robust and reliable for making predictions (Trayanova et al. 2023). For instance, in cardiac physiology, an increase in a biomarker might have a strong effect up to a point, after which the effect tapers off, which can be captured with nonlinear terms (Trayanova 2011).

An example of this is the relationship between calcium transient amplitude (CaTa) and L-type calcium current permeability (G_{CaL}). As CaTa (a biomarker of calcium dynamics) increases, the effect on G_{CaL} (maximal L-type calcium current permeability) might be strong initially. For small increases in CaTa, the corresponding increase in G_{CaL} could be substantial because of the strong dependence of calcium dynamics on the permeability of calcium channels. However, beyond a certain CaTa threshold, further increases result in a smaller increase of G_{CaL}. This indicates a concave-down (or saturating) relationship between CaTa and G_{CaL}. To model such a nonlinear relationship, we consider incorporating a squared term like CaTa^2 which is effective when combined with a linear term.

$$G_{\mathrm{CaL}} = \alpha \cdot CaTa + \beta \cdot \mathrm{CaTa}^2, \tag{4.12}$$

where α is the linear effect of CaTa on G_{CaL} and β is the quadratic effect. β is negative as it responds to the slow increase of G_{CaL} as CaTa increses which follows the concave-down graph shape. So, for low CaTa values, $\alpha \cdot CaTa$ dominates, resulting in a strong increase in G_{CaL}. Whereas for higher CaTa values, the negative $\beta \cdot \mathrm{CaTa}^2$ outweighs the linear term, causing the increase in G_{CaL} to slow down.

4.5.2 Baseline Cardiac Action Potential Model from Tusscher et al. (2004)

In this study, we employed the Ten Tusscher NobleNoblePanfilov (TNNP) model (Tusscher et al. 2004), which is one of the most widely used human ventricular cell models in cardiac electrophysiology. The TNNP model was developed to simulate the electrical activity of human ventricular cells and provides three distinct sets of parameters to represent the three major cell types found in the ventricular myocardium: epicardial, endocardial, and M cells. These cells differ in their AP profiles due to their unique ion channel properties and are located in different layers of the ventricular wall, with M cells situated between the endocardial and epicardial layers.

The model consists of 12 gating variables that govern the opening and closing of ion channels, controlling the flow of ions such as sodium $\left(\mathrm{Na}^{+}\right)$, potassium $\left(\mathrm{K}^{+}\right)$, and calcium $\left(\mathrm{Ca}^{2+}\right)$ across the cell membrane. In addition to the gating variables, the TNNP model simulates the intracellular concentrations of $\mathrm{Na}^{+}, \mathrm{K}^{+}$, and Ca^{2+}, which are crucial for generating APs and regulating cardiac excitability and contractility.

The TNNP model consists of a system of differential equations, including the voltage equation, which describes the change in membrane potential over time in response to ionic currents. This allows the model to capture the dynamic behaviour of a single ventricular cell in response to electrical stimuli. The TNNP model has since been used extensively in cardiac research, offering insights into the mechanisms of arrhythmias, drug interactions, and the overall electrophysiological function of the heart (Ten Tusscher and Panfilov 2006). For a detailed description

of the voltage equation and all the associated variables governing ionic currents and gating mechanisms, refer to the original publication by (Tusscher et al. 2004). We chose this model because the work by (Sarkar and Sobie 2010) was based on the TNNP model, and this study aims to explore whether the regression can be further improved.

4.5.3 Sampling and Generating a Population of Models

To generate a population of cardiac models with varying ionic conductances, we utilised the Latin hypercube sampling (LHS) method (McKay et al. 2000). It is a statistical approach commonly employed for constructing computer experiments and ensuring efficient parameter randomisation across a given range of distributions. In essence, the method divides each parameters function into equal partitions, with the number of divisions determined by the number of sample points desired. For our study, we applied LHS to the 16 ionic conductances associated with cardiac cellular electrophysiology, allowing us to create a set of 500 unique models. Each of these models represented different combinations of conductance parameters, drawn from a distribution that varied by approximately 70% from the baseline values. Parameters were set to vary between 0.1 and nearly double their original values to ensure a wide range of physiological behaviours while still maintaining realistic conditions. Table 4.2 contains all the conductances we used in the TNNP simulation. After generating these 500 variants of the TNNP model (Tusscher et al. 2004), we simulated APs and calcium transients to extract key biomarkers. These biomarkers include:

- Vmax (Vpeak): The maximum or peak voltage value of the membrane potential following a stimulus.
- APD90 and APD30: The time from the beginning of the stimulus to the point where the membrane potential reaches 90% or 30% respectively, of full repolarisation, defined by the difference between the peak and resting membrane potentials.
- CaTa (Δ Ca): The calcium transient amplitude, calculated as the difference between the peak and diastolic levels of intracellular calcium $\left(\mathrm{Ca}^{2+}\right)$.
- CaTrest: The calcium transient at rest, representing the baseline calcium level between beats.

conductances	Definition	Baseline value
G_{Na}	Maximal Na^+ conductance	$14.838 nS/pF$
G_{Nab}	Background Na^+ conductance	$2.9 \times 10^{-4} nS/pF$
G_{CaL}	Maximal L-type Ca $^{2+}$ current permeability	1.75×10^{-4} cm3/μF.s
G_{Cab}	Background Ca^{2+} conductance	$5.92 \times 10^{-4} nS/pF$
G_{to}	Maximal transient outward K^+ conductance	$0.294 nS/pF$
G_{Kr}	Rapid delayed rectifier K^+ current scaling factor	$0.096 nS/pF$
G_{Ks}	Maximal slow delayed rectifier K^+ conductance	$0.245 nS/pF$
G_{K1}	Maximal inward rectifier K^+ conductance	$5.405 nS/pF$
G_{pK}	Maximal plateau K^+ conductance	$0.0146 nS/pF$
I_{NaK}	Maximal $Na^+ - K^+$ pump current	$1.362 pA/pF$
k_{NaCa}	Maximal $Na^+ - Ca^{2+}$ exchange current	$1000 pA/pF$
a_{rel}	SR Ca $^{2+}$ release scaling factor	$16.464 \mu M ms^{-1}$
c_{rel}	SR Ca^{2+} release scaling factor	$8.232 \mu M ms^{-1}$
V_{leak}	Passive SR Ca $^{2+}$ leak scaling factor	8×10^{-5} ms^{-1}
I_{up}	Maximal rate of SR Ca^{2+} uptake (SERCA)	$0.425 \mu M/ms$
G_{pCa}	Maximal sarcolemmal Ca $^{2+}$ pump current	$0.825 pA/pF$

Table 4.2: This table lists the baseline values for 16 parameters in the TNNP model, which include ionic conductances and related scaling factors regulating ionic currents or intracellular processes. All other parameters in the TNNP model were kept unchanged, ensuring that the observed variability in outputs was solely due to the variation of the parameters listed here. Baseline values are consistent with those reported in (Tusscher et al. 2004) and (Sarkar and Sobie 2010).While parameters such as G_{Na} and G_{Kr} represent true ionic conductances, others, like a_{rel} and $V_{leak,}$, are scaling factors related to calcium dynamics or transport processes. The term "conductance" is used broadly to encompass all these parameters. These parameters were varied by up to $\pm 70\%$ of their baseline values using Latin Hypercube Sampling (LHS) to generate a population of 500 models for sensitivity analysis.

- CaT90: The time interval at which the calcium transient reaches 90% of its recovery to the resting state after an AP.

By combining these variations in conductances with physiological outputs, we created a robust dataset for regression analysis.

4.5.4 Method

We started by constructing a dataset in which the dependent variable is G_{CaL}, the maximal L-type calcium current permeability. This is the key variable we aim to predict or explain using a set of biomarkers derived from simulations. The dataset includes values for six key biomarkers, as described previously, along with the squared terms for each of these biomarkers. By incorporating both linear and squared terms, we ensure the model can capture both simple

and more complex nonlinear relationships between the biomarkers and G_{CaL}. Now we have two different sets of predictor variables in our regression analysis: linear and nonlinear terms. The linear terms include Vmax, APD90, APD30, CaTa, CaTrest, and CaT90, while the nonlinear terms consist of the squared values of each, such as Vmax^2, $\mathrm{APD90}^2$, $\mathrm{APD30}^2$, CaTa^2, $\mathrm{CaTrest}^2$, $\mathrm{CaT90}^2$.

We then constructed two separate models for OLS regression analysis. The first one we called it the the Full Model, which included both the linear and nonlinear squared terms of all six biomarkers. This allowed us to examine potential nonlinear relationships between the biomarkers and the dependent variable, G_{CaL}. The second one is the Reduced Model, which included only the linear terms, omitting the squared terms. By comparing the two models, we aimed to determine how much explanatory power was lost when the nonlinear effects were removed, thereby assessing the importance of the nonlinear relationships in the data.

Then we applied stepwise regression using the backward selection method for both the full and reduced models. The process began with the Full Model that included all predictors, and then iteratively removed the least significant predictor based on the Akaike Information Criterion (AIC) until the optimal subset of variables was identified. To ensure robustness and avoid overfitting in the regression models we implemented several techniques:

- We used 0-fold cross-validation which is a process that is repeated 10 times and divides the data into 10 subsets, trains the model on 9 subsets, and validates on the remaining one.
- We performed stepwise regression with backward selection, which starts with a full model and iteratively removes less significant predictors. This reduces model complexity by keeping only the most relevant variables, helping to prevent overfitting.
- We specified the maximum number of predictors to consider to ensure that only the most important variables are retained in the model, balancing simplicity and predictive accuracy.

4.5.5 Results

The plot 4.8 presents a comparison of model performance for both linear and nonlinear models in predicting G_{CaL} the maximal L-type calcium current permeability. It depicts how the Root Mean Square Error (RMSE) and R^2 values change as the number of variables (n) in the model increases, for both linear and nonlinear models. The x-axis represents the number of variables included in the model, while the y-axis represents both RMSE and R^2 values.

The blue line shows the RMSE values for the nonlinear models, while the green line shows RMSE values for the linear models. RMSE measures the average difference between the observed and predicted values, with lower values indicating better model performance. As expected, we observe a general decrease in RMSE as the number of variables increases, indicating improved model fit with more predictors. The red line represents the R^2 values for the nonlinear models, and the black line represents the R^2 values for the linear models. R^2 measures the proportion of variance in the dependent variable that is explained by the model, with higher values indicating a better fit. We see that the R^2 values increase as the number of variables increases, meaning the models explain more of the variation in G_{CaL} as additional predictors are added. This plot is critical for evaluating the trade-off between model complexity and predictive accuracy. It demonstrates how adding both linear and nonlinear terms to the model affects its performance. By comparing RMSE and R^2 for linear and nonlinear models across varying numbers of predictors, we can assess how much explanatory power is gained by including nonlinear terms. Notably, nonlinear models tend to have higher R^2 values and lower RMSE than their linear counterparts, indicating that the inclusion of nonlinear terms improves the overall model fit. Also, from this plot, we can decide the optimal number of variables to include in the model. Adding too many variables could lead to overfitting, while too few variables might result in an underfitted model that doesn't capture the relationships well. This visualisation helps balance model complexity with predictive accuracy, guiding the selection of the best subset of predictors.

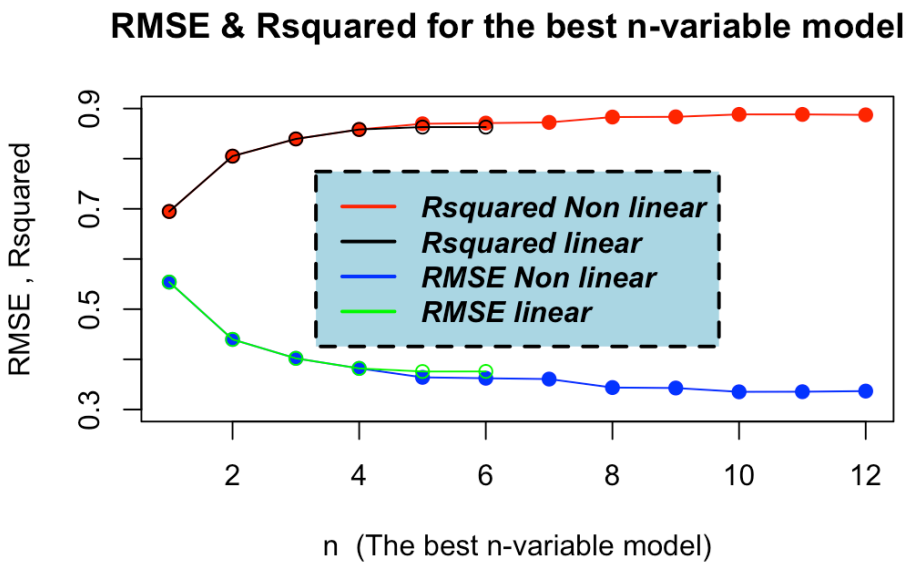

Figure 4.8: The plot compares the Root Mean Square Error (RMSE) and R-squared R^2 values for the best linear and nonlinear models across different numbers of predictors (n). The red and black lines represent the R^2 values for nonlinear and linear models, respectively, while the blue and green lines depict the RMSE values. The graph demonstrates that nonlinear models consistently achieve higher R^2 and lower RMSE values, indicating better fit and predictive accuracy compared to linear models. The x-axis shows the number of variables included in the model, with both linear and nonlinear models improving as more predictors are added.

The optimal model for predicting G_{CaL} appears to be the nonlinear model with 6 variables, as it provides both a high R^2 value and a low RMSE, indicating strong predictive accuracy and minimal error without overfitting.

The bar graph in Figure 4.9 illustrates the regression coefficients for both the linear and nonlinear models used to predict G_{CaL}, the maximal L-type calcium current permeability. The blue bars represent the coefficients from the linear model, while the green bars represent the additional coefficients from the nonlinear model, which includes squared terms. Each predictor (such as Vmax, APD90 and APD30) is listed on the x-axis, along with their squared terms. The height of each bar reflects the strength and direction (positive or negative) of each predictor's contribution to the model. For instance, APD30 shows a large positive impact in both the linear and nonlinear models, while other predictors like $CaTa^2$ exhibit a minor negative contribution. This visualization highlights how both linear and nonlinear terms influence the model and allows for comparison of the relative importance of each predictor in determining G_{CaL}. The

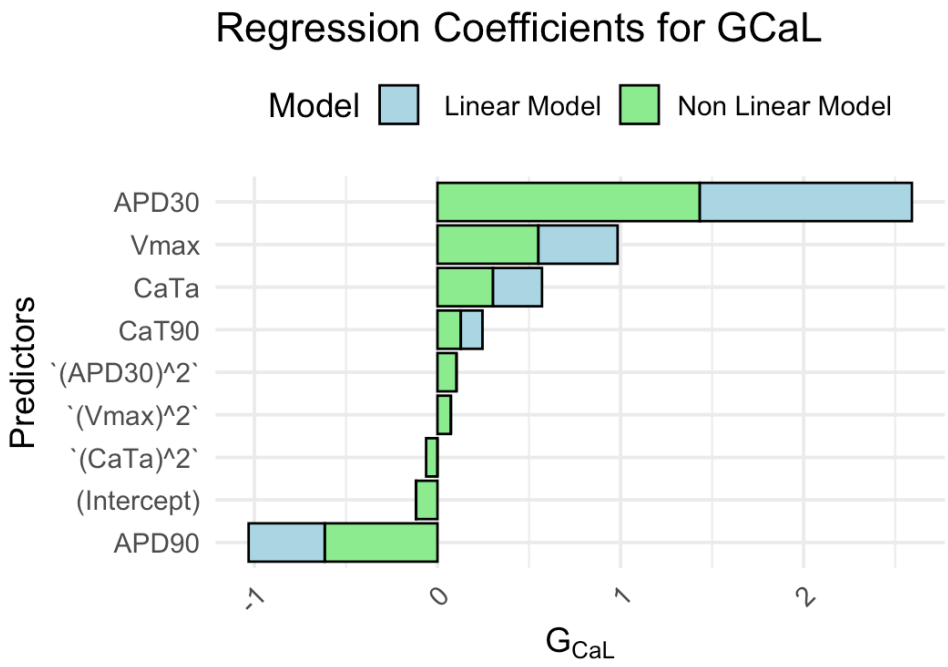

Figure 4.9: This figure illustrates the regression coefficients for both the linear and nonlinear terms used to predict G_{CaL}, the maximal L-type calcium current permeability. The blue bars represent the coefficients from the linear model, while the green bars represent the additional coefficients from the nonlinear model, which includes squared terms. Each predictor (such as Vmax, APD90 and APD30) is listed on the x-axis, along with their squared terms. The height of each bar reflects the strength and direction (positive or negative) of each predictor's contribution to the model. For instance, APD30 shows a large positive impact in both the linear and nonlinear models, while other predictors like CaTa^2 exhibit a minor negative contribution. This visualisation highlights how both linear and nonlinear terms influence the model and allows for comparison of the relative importance of each predictor in determining G_{CaL}.

predictors APD30 and APD90 seem to have the strongest influence on G_{CaL} as indicated by their large coefficients, both in the linear and nonlinear models. These variables show a positive contribution, meaning that the increases in APD30 and APD90 are related to the increase in G_{CaL}. The squared terms, represented by the green bars, show that the nonlinear model introduces additional contributions for variables like Vmax^2, $\mathrm{APD30}^2$, CaTa^2. These nonlinear terms help capture more complex relationships between these predictors and G_{CaL} particularly when the effect of a predictor changes at higher or lower levels. For instance, Vmax^2 has a small but positive contribution in the nonlinear model, suggesting that higher values of Vmax amplify its effect on G_{CaL}.

4.6 Discussion

In our analysis using stepwise regression, we found that only 9 out of the 16 conductances involved square terms in the optimal model, while the remaining 7 conductances did not exhibit any significant nonlinear relationships through squared terms as shown in Figure 4.10. This suggests that while the stepwise regression approach, incorporating both linear and nonlinear terms, is a useful tool for exploring relationships between variables, it may not fully capture the complexity of the underlying nonlinear interactions in the data. The method is effective in identifying key linear relationships and has the advantage of being easy to interpret. However, the limited inclusion of nonlinear terms suggests that this approach may fall short in situations where more intricate, nonlinear dynamics govern the behaviour of the system. In such cases, relying solely on polynomial regression or stepwise selection may overlook important nonlinear patterns.

Another reason could be that stepwise regression has a localized approach when it comes to capturing nonlinear relationships. In real-world data, especially in biological systems like cardiac modeling, the relationship between conductances and biomarkers may vary across different ranges of the data. For instance: In one range of a biomarker (e.g., low values of APD90) the relationship with conductance might be best described by a quadratic form. While in another range (e.g., higher values of APD90) the relationship could become more cubic or exhibit entirely different nonlinear dynamics.

In the regression process, we typically include specific nonlinear terms that apply globally to the entire data range. However, this means that the relationship between variables is constrained to be of a particular form across all values of the predictors. This limitation can make it difficult for the regression technique to capture more complex relationships that may change across different ranges of data.

To further improve the model's ability to capture the nonlinear interactions among conductances and biomarkers, we will explore more advanced techniques in the next chapter. We investigated Gaussian process regression, which is considered an excellent choice for capturing nonlinear interactions among conductances and biomarkers (Kennedy and O'Hagan 2001). The Gaussian process is a non-parametric, probabilistic model that is particularly effective in handling complex and nonlinear relationships in data. They are often used in scenarios where standard regression models fail to capture the underlying complexity, as they provide a flexible and robust way to model uncertainty in predictions and nonlinearity.

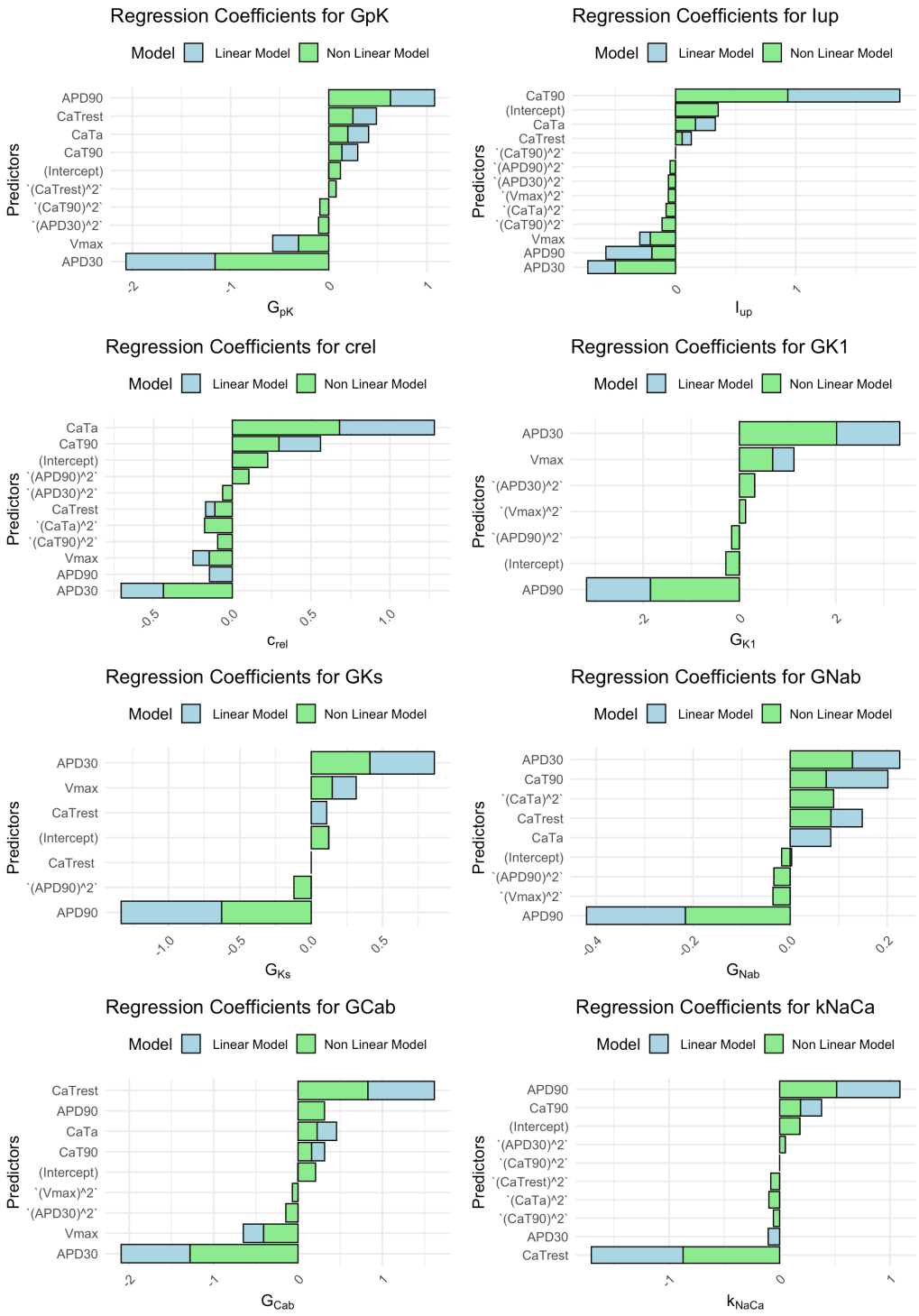

Figure 4.10: Regression Coefficients for Conductances and their Nonlinear Terms. The figure shows the contributions of linear and nonlinear terms in predicting GCaL. Nonlinear terms were included for 9 of the 16 conductances, while the remaining 7 did not exhibit significant nonlinear relationships.

Chapter 5

Rejection Sampling Using Gaussian Process on Cardiac Single Cell Models

5.1 Introduction

5.1.1 Motivation

Variability is an inherent characteristic of all biological systems, including cardiac electrophysiology (Trayanova et al. 2023). Historically, this variability has often been overlooked in research and computational analyses (McEntire et al. 2021). Even cardiomyocytes derived from genetically similar and healthy animal models exhibit considerable heterogeneity in their characteristics among individual cells (Lachaud et al. 2022). Recent studies have documented significant variations in ion channel expression between cells (Clark et al. 2023), highlighting the importance of understanding this variability, though it remains a substantial challenge (Muszkiewicz et al. 2016).

Traditional computational modelling approaches typically generate a single representative cardiomyocyte, which fails to capture the true diversity observed in individual cells. To address this limitation, the population of models approach has gained popularity in electrophysiology modelling, enabling the exploration of mechanisms underlying physiological variability in cardiac electrophysiology. Recent studies have employed this approach, demonstrating its potential to better understand the variability in cardiac function (Sarkar et al. 2012; Britton et al. 2013; Whittaker et al. 2020).

5.1.2 Aim

This chapter seeks to enhance our understanding of cardiac models and myocytes by investigating the factors contributing to variability in action potential duration (APD). To achieve this, we employ a statistical technique known as an emulator to estimate the parameter values of cardiac action potential (AP) models, which are essential in defining the internal physiological state of the cell. In a recent study (Lachaud et al. 2022), a large set of models was generated by systematically varying the maximal conductances of eight ion channels. These models were subsequently evaluated using a simulator that effectively replicated the responses observed in ICa(L) and IK(r) block experiments. Our objective is to generate populations of cell models that precisely replicate the observed variability in APD, with the aim of determining whether this variability can be linked to specific variations in the relative expression of ion channels across different cells.

5.2 Methods

5.2.1 Baseline Cardiac Model from Shannon Model (2004)

Several models of the action potential in rabbit ventricular myocytes have been developed and extensively discussed in the literature, including those by (Mahajan et al. 2008) and (Luo and Rudy 1994). For the current study, the Shannon model (Shannon et al. 2004) was selected, as it was specifically designed using data derived from rabbit ventricular cells. This model was chosen for its ability to accurately represent the action potential of rabbit ventricular myocytes, making it particularly relevant for clinical applications.

This model incorporates 14 transmembrane currents, including fast Na^+, L-type Ca^{2+}, the rapid and slow components of the delayed rectifier K^+, inward rectifier K^+, fast and slow transient outward K^+, Ca^{2+}-activated Cl^-, $\mathrm{Na}^+ - \mathrm{Ca}^{2+}$ exchanger, $\mathrm{Na}^+ - \mathrm{K}^+$ pump, sarcolemmal Ca^{2+} pump, and background Na^+, K^+, and Cl^- currents. The model uses a total of 45 variables to replicate some experimental observations, such as action potential morphology, action potential duration, and restitution curves. The model's relative computational simplicity makes it well-suited for exploring the dynamics of cardiac electrophysiology.

5.2.2 Model Inputs and Outputs

The membrane voltage (V) in a cardiac cell is typically described by the following ordinary differential equation (ODE):

$$\frac{dV}{dt} = -\frac{1}{C_m}\left(I_{\text{ion}} + I_{\text{stim}}\right), \tag{5.1}$$

where:

- V is the membrane voltage,
- C_m is the membrane capacitance,
- I_{ion} represents the total ionic current across the membrane,
- I_{stim} is an external stimulus current.

Equation (5.1) captures the rate of change of the membrane voltage as a function of the total ionic currents and any external stimulus applied to the cell. The total ionic current across the membrane, I_{ion} , is typically represented as the sum of all individual ionic currents flowing through various ion channels, pumps, and exchangers in the cell membrane. The equation can be written as:

$$I_{\text{ion}} = I_{\text{Na}} + I_{\text{Kr}} + I_{\text{to}} + I_{\text{NaCa}} + I_{\text{Clb}} + I_{\text{CaL}} + I_{\text{NaK}} + I_{\text{Ks}} + \cdots \tag{5.2}$$

Each term represents a different ionic current, contributing to the overall ionic current I_{ion} that influences the membrane voltage. Additional currents may be included depending on the specific model or the types of ionic channels, exchangers, and pumps considered. Each current in the Shannon model for rabbit ventricular myocytes is typically described by an equation, for instance, the equation for the sodium current (I_{Na}) is:

$$I_{\text{Na}} = G_{\text{Na}} m^3 h j \left(V - E_{\text{Na}}\right), \tag{5.3}$$

where:

- G_{Na} is the maximum sodium conductance,
- m, h, and j are gating variables that represent the activation and inactivation states of the sodium channel,
- E_{Na} is the equilibrium (Nernst) potential for sodium.

In this study, eight ionic conductances were selected for random variation by modifying the baseline conductance with a scale factor p. These scale factors are referred to as inputs. For instance, the modified conductance for G_{Kr} can be expressed as:

$$G'_{\text{Kr}} = p \cdot G_{\text{Kr,baseline}} \tag{5.4}$$

Table 5.1 lists currents and pumps in the Shannon model (Shannon et al. 2004), whose conductances were varied to construct populations of models. The eight conductances are chosen based on a preliminary parameter sensitivity analysis, which showed that the conductance of eight ionic currents had the most significant impact on repolarisation (Romero et al. 2009). The selection of these conductances was also informed by prior investigations by Lachaud (Lachaud et al. 2022), where simulation techniques were used to analyse the impact of each conductance on the action potential. A population of models was generated by applying these modifications to the baseline conductances. The Shannon model (Shannon et al. 2004) was simulated using MATLAB (R2019B, The MathWorks, Inc., USA), with code obtained from the

Ionic currents	Description
INaK	Sodium-potassium pump current
IKr	Rapid delayed rectifier potassium current
Itos	Slow transient outward potassium current
IK1	Inward rectifying potassium current
INaCa	Sodium-calcium exchanger current
IClb	Background chloride current
ICaL	L-type calcium current
IKs	Slow delayed rectifier potassium current

Table 5.1: List of ionic currents and pumps in the Shannon model (Shannon et al. 2004), whose conductances were varied to construct populations of models.

CellML repository (www.cellml.org) (Miller et al. 2010). The simulation focused on measuring three key model biomarkers: action potential duration at 90%, 50%, and 30% repolarisation (APD90, APD50, and APD30, respectively), all derived directly from the action potential. These biomarkers are referred to as outputs in this context.

5.2.3 Gaussian Process Emulators

Statistical emulators, such as Gaussian Processes (GPs), have been widely applied across various fields of research. These applications range from predicting scalar values in cardiac electrophysiology (Coveney and Clayton 2020), to musculoskeletal modelling (Benemerito et al. 2022), time series analysis in finance (Han et al. 2016), and weather forecasting (Roberts et al. 2013). A GP is a powerful regression tool commonly used in machine learning, well-suited for handling uncertainty and variability. GP emulators, which comprise mean and variance components, provide a probabilistic estimate of the output, making them invaluable for sensitivity and uncertainty analysis.

The Gaussian Process emulator is particularly effective in clarifying the input-output relationships in complex, nonlinear systems. The model is initially trained on a set of design data that includes both inputs and corresponding outputs. Once trained, a GP emulator can swiftly predict the required output for new inputs that were not part of the original training set. In a study by (Chang et al. 2015), GP emulators were used to manage uncertainty and variability in a cardiac cell model, offering significant advantages over traditional methods such as Monte

Carlo simulations, which require a large number of simulator runs to achieve similar results (Melis et al. 2017). Various methodologies can be employed to construct an emulator for a complex model. Recent studies have utilised partial least squares (PLS) regression to develop emulators that are particularly effective for sensitivity analysis (Sobie 2009; Sarkar et al. 2012).

5.2.4 Constructing a Gaussian Process Emulator

A Gaussian Process (GP), as defined by Rasmussen(Williams and Rasmussen 2006), is a powerful statistical tool that models a collection of random variables, with the defining property that any finite subset of these variables has a joint Gaussian distribution. This characteristic allows GPs to flexibly capture complex relationships in data. In the context of this study, GPs are parametrised by two essential functions: a mean function and a covariance function. The mean function represents the central trend or expected value of the process across the input space, while the covariance function (also known as the kernel function) describes the degree of correlation or similarity between function values at different input points.

In constructing GP emulators for this research, we employed the scikit-learn library, which provides robust tools for implementing and optimising GPs. Each emulator developed is characterised by a GP with a linear mean function, which captures the general trend of the data, and a Gaussian covariance function, which effectively models the relationships and dependencies between different inputs. The hyperparameters of these emulators, which control the behaviour of the mean and covariance functions, were optimised through training on a set of design data. This training process assumed a uniform prior distribution, allowing the emulator to generalise well to new data while maintaining flexibility in modelling complex patterns. The result is a set of GP emulators that are both accurate and computationally efficient, capable of providing reliable predictions and insights into the underlying processes being studied.

The validation of the emulators was conducted by generating an additional set of test data, which included both inputs and corresponding outputs derived from simulator runs. This test data served as a benchmark to assess the accuracy and reliability of the emulators. For each set of inputs in the test data, the outputs predicted by the emulator were directly compared to the outputs generated by the action potential (AP) simulator model.

To rigorously evaluate the differences between the outputs produced by the emulator and those from the AP simulator, the Bland-Altman test (Bland and Altman 1986) was employed. The Bland-Altman test is a widely recognised method for assessing agreement between two different measurement techniques. It involves plotting the differences between the two methods against their mean, allowing for the identification of any systematic biases and the assessment of the limits of agreement. By applying this statistical test, we were able to quantify the degree of accuracy of the emulator in replicating the simulator outputs, ensuring that the emulator provides a reliable approximation of the AP simulator model across the range of tested inputs. This validation step is crucial for confirming that the emulator can be confidently used as a surrogate for the more computationally intensive simulator in further analyses.

5.2.5 Rejection Sampling

Rejection sampling is a statistical inference technique used to generate random values from a target distribution. This method is rooted in the Monte Carlo approach, which involves generating random samples from a proposal distribution and subsequently rejecting those that do not satisfy a specific acceptance criterion. The acceptance of a sample is determined through a rigorous comparison of the ratio between the target density and the proposal density. Specifically, each sample is evaluated against this ratio, and only those that meet the required threshold are accepted. The accepted samples are then distributed according to the desired target density, ensuring that they accurately represent the underlying distribution of interest.

This technique is particularly useful in scenarios where direct sampling from the target distribution is challenging or computationally expensive. By carefully selecting the proposal distribution and applying the rejection criterion, rejection sampling allows for the efficient generation of samples that conform to the desired distribution. For a more detailed discussion on the implementation and application of rejection sampling, including its initial development and various adaptations, please refer to the foundational works by (Gilks and Wild 1992; Robert et al. 1999; Gilks et al. 1994; Künsch 2005). These references provide a comprehensive overview of the methodology and its practical applications in statistical inference.

The fundamental principle of rejection sampling is that the proposal density must fully encompass the target density. In practical terms, this requires that the target distribution be completely covered by a scaled version of the proposal distribution. The aim is to ensure that the ratio of the target density to the proposal density does not exceed a certain scaling factor, which is greater than one. This condition ensures that the method efficiently selects samples that accurately represent the target distribution.

Let $f(x)$ be the target density and let $g(x)$ be the proposal density, then the ration $f(x)/g(x)$ must not exceed a particular scaling factor k, where k is greater than 1. For a given value of k, we have the condition that $0 < f(x)/k^{\star}g(x) < 1$. To optimise efficiency, it is preferable to minimise the value of the scaling factor k, as larger values result in the rejection of a significant number of samples.

The Algorithm

Once the condition is met and the constant k is determined, the rejection sampling procedure can proceed. The following algorithm provides a clear, step-by-step guide for efficiently generating samples from the target distribution f, as successfully demonstrated in the work by (Ridley and Forget 2021):

- Simulate $U \sim \mathrm{Unif}(0, 1)$.

- Simulate a candidate $X \sim g$ from the proposal density.
- If $U \leq \frac{f(X)}{kg(X)}$, then "accept" the candidate X.
- Otherwise, "reject" X and go back to the beginning.
- Repeat until the desired number of samples from the target density f has been accepted.

The rejection sampling algorithm is characterised by the property that the number of attempts required to accept a candidate sample follows a geometric distribution, where the probability of success on each attempt is the reciprocal of the scaling factor; $\frac{1}{k}$.

To achieve our objective of replicating the variation observed in experimental measurements, we have chosen to utilise Gaussian process emulators as our modelling approach. These emulators are advantageous due to their ease of sampling and their ability to be trained using design data that closely approximates the underlying characteristics of the target distribution, which in this case corresponds to the ion block experiments conducted by Lachaud et al. (Lachaud et al. 2022).

5.2.6 Design Data

Before constructing and running the Gaussian process emulator, we generated a design dataset that includes sets of parameter inputs and their corresponding output values from simulations. These design data are used to build and fit the GP emulator and can then be used to evaluate any dataset of inputs.

5.2.7 Simulation and Calibration of the Population of Models

In order to construct a GP emulator, it is vital to create a design dataset comprising a set of parameter inputs and the corresponding simulator outputs. To capture the variability in action potential duration (APD) between cells, a population of 6000 variants was created. These variants were constructed by sampling random values for the conductances from uniform distributions using Latin hypercube sampling (McKay et al. 2000). We apply a log-normally distributed

random scale factor to adjust the baseline value of each parameter for every individual. We selected these components to span a range of values from 0 to 2, so that the minimum value of the input parameter became 0, the maximum became 2, and the baseline value 1. This set of inputs is designed to cover a wide range of possible values for the input parameter. This will allow the emulator to accurately replicate the model over this actual range of values.

In order to ensure that emulators are trained well, it is important to use design data that covers the whole input space evenly. Therefore, we have opted to utilise Latin Hypercube sampling (McKay et al. 2000). The processing cost remains low regardless of the number of altered parameters, allowing for the investigation of a complex parameter space without incurring additional costs. Due to the complex structure of most cardiac cell models, it is not viable to computationally sample every potential combination of parameter values. The majority of studies examining experimentally-calibrated populations of models in cardiac electrophysiology, such as (Britton et al. 2014) utilised Latin Hypercube sampling.

The population of candidate models generated in the preceding stage is now subjected to simulation and calibration in order to identify the models that exhibit electrophysiological characteristics within the same range as those observed in experimental data. Firstly, each model in the population was integrated in time with a relative tolerance of 0.2×10^{-6} employing an adaptive-step, adaptive-order method for systems of stiff ordinary differential equations based on numerical differentiation formulas, implemented in MATLAB (R2019B, The MathWorks, Inc., USA). Then each model variant was stimulated by a constant current pulse at 2 Hz, a train of 1000 APs was computed, where the last two APs were recorded for APD values extraction and further analysis. The established protocols are utilised to quantify a set of three outputs, APD90, APD50, and APD30 where $APDxx$ is the action potential duration at $xx\%$ repolarisation.

Model runs were excluded from the design data if there was any evidence of unphysiological behaviour in the model outputs. Model variants were rejected from the population if they failed to depolarise above 0 mV or if they had a resting $V_m > -65\mathrm{mV}$. An experimental calibration process is conducted to define the range of values for model outputs. This is done by computing the minimum and maximum values received from experimental measurements. Extreme outliers are frequently eliminated to exclude any abnormalities. The biomarkers were APD90, APD50, and APD30 along with their calibration ranges are shown in Table 5.2.

Biomarker (Nifedipine Drug)	APD90	APD50	APD30
Min range (ms)	30.6	20.3	14.1
Max range (ms)	333.2	273.3	229.9
Biomarker (Dofetilide Drug)	APD90	APD50	APD30
Min range (ms)	90.9	75.5	46.1
Max range (ms)	376.5	323.2	263.5

Table 5.2: The calibration of the population of models for the drugs Nifedipine and Dofetilide involved determining the experimental ranges of selected biomarkers. Calibration ranges taken from (Lachaud et al. 2022).

5.2.8 Fitting GP Emulators

Cardiac cell models function as simulators that generate a vector of outputs, denoted as A_s, based on a vector of input parameters, denoted as G. This relationship can be expressed mathematically as $A_s = f_s(G)$. To construct and fit the emulator, approximately 80% of the available design data, referred to as the training dataset, is utilised. These emulators are subsequently evaluated using a test dataset, which is generated independently from simulator runs and is not involved in the fitting process. Our approach to constructing Gaussian process emulators follows methodologies established in recent research (Chang et al. 2015). Separate emulators were developed for each model output.

Generally, an emulator is a statistical model that approximates a simulator, often referred to as a surrogate model. The emulator models the relationship as $A_e = f_e(G)$, where the emulator's output approximates the simulator's output, such that $A_e \approx A_s$ for a given input G. In this study, the emulator is defined as a Gaussian process, with its hyperparameters optimised using a set of simulator runs known as design data. Once the Gaussian process is trained, it can provide posterior predictions A_e for a new input G^*, even if the simulator has not been run for

that specific input. This posterior prediction is represented as a probability distribution that includes both an expected value and a variance. The variance of the prediction A_e quantifies the uncertainty associated with predicting the simulator's behaviour at G^* (Coveney and Clayton 2020).

5.2.9 Conducting Rejection Sampling

In this chapter, our objective is to accurately replicate the variations observed in experiments to analyse the conductances. To achieve this, rejection sampling is used to reproduce APDs matching the experimental ones. We used Gaussian process emulators as the proposed density as these emulators are easily obtainable for sampling and are trained using design data that roughly equals the target density, which corresponds to the ion block study conducted by Lachaud et al. (Lachaud et al. 2022). This experimental data we use to demonstrate our techniques consists of APD values measured from rabbit ventricular cells.

5.3 Results

In this section, we will focus exclusively on presenting the findings related to the output APD90. All other outputs, as well as the results involving the drug Dofetilide, will be discussed in detail in Chapter 6.

For each model variant in the population, the simulator was used to generate both the design (training) and test datasets, with the resulting action potentials serving as the basis for deriving the outputs. Figure 5.1 shows the time series of action potentials from the initial population, which were utilised to measure the APD biomarkers. The APD outputs, directly measured from these action potentials, are depicted in Figure 5.2, where APDxx is the time intervals between the beginning of an AP and $xx\%$ repolarisation from maximum voltage (Vpeak). After the simulation, we carried out a filtering process to evaluate each model variant to ensure it successfully generated a valid action potential (AP). In the context of cardiac electrophysiology, a valid action potential refers to a waveform that accurately reflects the physiological characteristics of a cardiac cell's electrical activity, including the proper initiation, depolarisation, plateau phase, and repolarization of the cell membrane. All AP phases are explained in details in

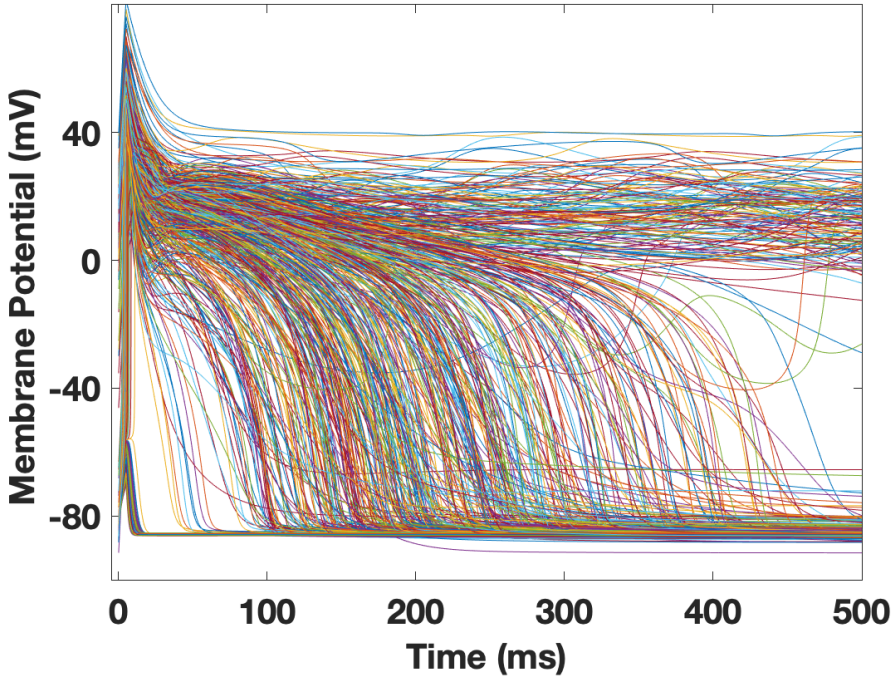

Figure 5.1: Time series of action potentials generated from the initial population of rabbit Shannon models (Shannon et al. 2004) using the simulator. These time series were used to derive key APD biomarkers, forming the basis for both the design (training) and test datasets. The figure visually represents the variation in action potentials across different model variants, highlighting the diversity within the population and providing a foundation for subsequent analysis of the APD measurements

Chapter 2. This valid waveform is crucial because it represents the cell's ability to respond to electrical stimuli and propagate an electrical signal, which is essential for coordinated heart function. Models that failed to produce a valid action potentialdue to issues such as incorrect ion channel behaviour, abnormal resting potentials, or incomplete repolarizationwere excluded from further analysis. Only those model variants that generated realistic and physiologically plausible action potentials were retained, ensuring that subsequent analyses were based on accurate and meaningful data. This step was critical in maintaining the scientific validity of our study and ensuring that the conclusions drawn reflect true biological processes. Figure 5.3 provides a visual representation of several model variants, specifically highlighting the APD90 values which is a critical metric in cardiac electrophysiology, reflecting the normal rhythm and function of cardiac cells. In examining the figure, we observe that while some models successfully produced valid action potentials with APD90 values within the expected physiological range of 100 to 400 milliseconds, there are notable exceptions. Some models exhibited APD90

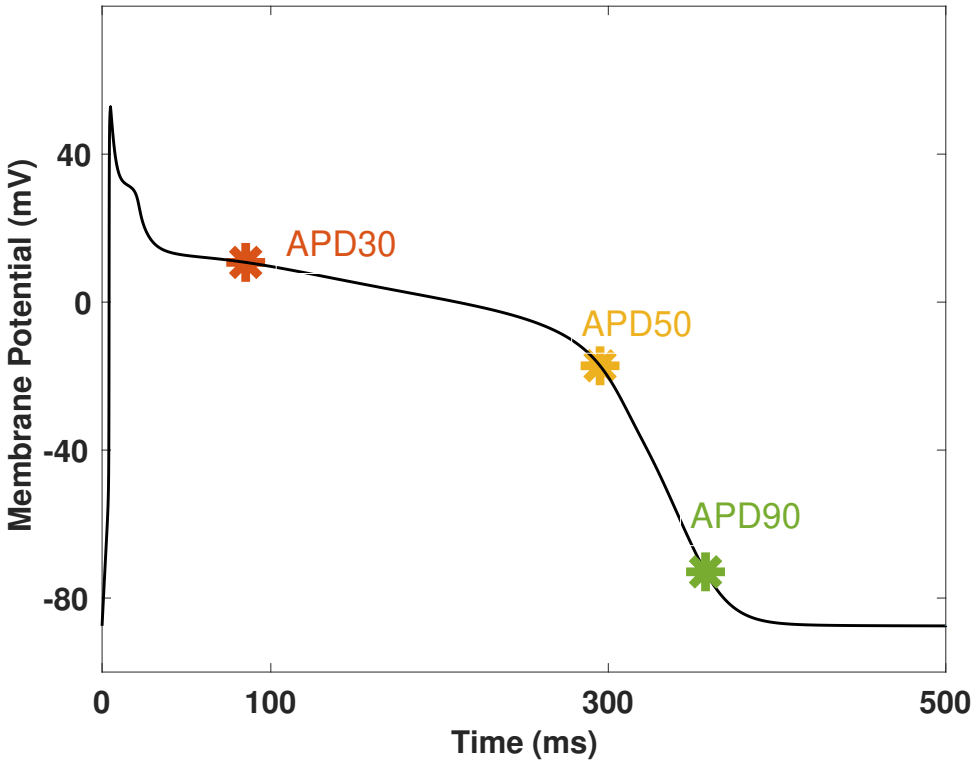

Figure 5.2: Action potential recorded biomarkers. APDxx values are the time intervals between the beginning of an AP and $xx\%$ repolarisation from maximum voltage (Vpeak)

values outside this range, particularly those falling below 100 milliseconds or exceeding 400 milliseconds. These outliers likely correspond to models that failed to produce a valid action potential. We conclude that models with APD90 values outside the typical range often indicate non-physiological or unstable behaviours, making them unsuitable for further analysis.

5.3.1 Validation of GP Emulators

Figure 5.4 provides a comprehensive analysis of the accuracy and reliability of the APD90 GP emulator by comparing its outputs directly against those generated by the traditional simulator across a wide range of test data points. The figure utilises a Bland-Altman plot, a statistical method commonly employed to assess the agreement between two different measurement techniques. In this plot, the x-axis represents the average of the APD90 values obtained from the simulator and the GP emulator, calculated as:

$$\text{Average APD90} = \frac{\text{APD90}_{\text{sim}} + \text{APD90}_{\text{emu}}}{2} \tag{5.5}$$

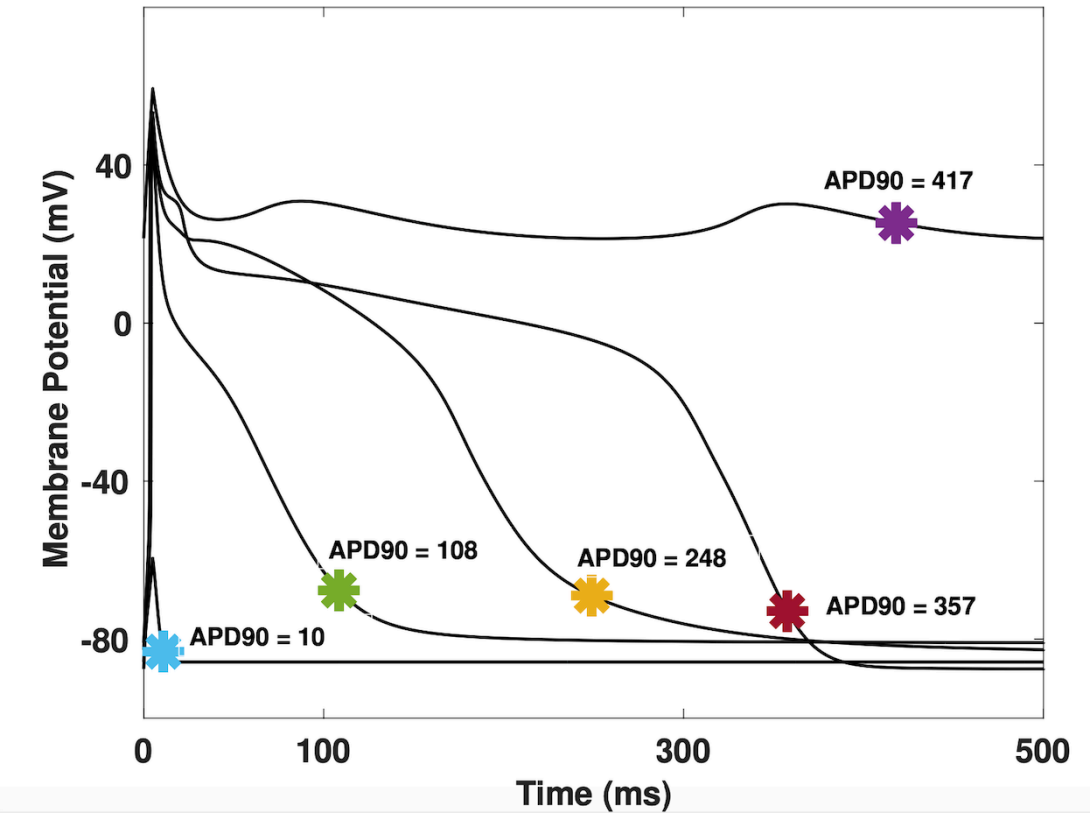

Figure 5.3: A procedure of elimination was conducted to exclude any action potential (AP) when the APDxx falls outside of an acceptable range. Here are some different values of APD90 with the corresponding AP traces.

The y-axis represents the difference between the APD90 values predicted by the emulator and those calculated by the simulator, expressed as:

$$\text{Difference in APD90} = \text{APD90}_{\text{emu}} - \text{APD90}_{\text{sim}} \tag{5.6}$$

Each point on the plot corresponds to a specific input, showing the difference between the APD90 values predicted by the emulator and those produced by the simulator plotted against the average of these two values. The dashed lines in the plot are particularly significant as they represent the mean difference between the two methods, ∓ 1.96 standard deviations. These boundaries encompass approximately 95% of the differences between the emulator and simulator outputs, providing a clear indication of the expected range of variation, or "limits of agreement", between the two methods.

The placement of data points within these limits is crucial for evaluating the emulator's performance. Points that lie within the dashed lines suggest that the emulator's predictions are generally consistent with the simulator's results, indicating that the emulator is a reliable alternative to the simulator in those instances. Conversely, points falling outside these bounds highlight areas where the emulator's predictions significantly diverge from the simulator, signaling potential discrepancies that may require further investigation.

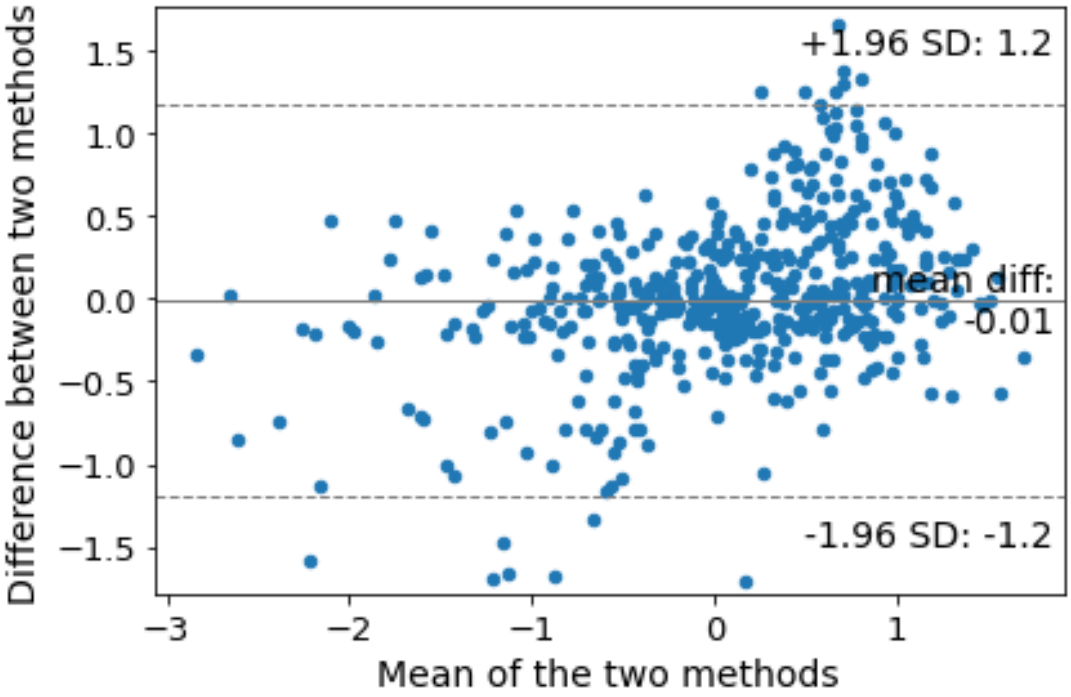

Figure 5.4: Bland-Altman plot comparing the APD90 measurements obtained from the Simulator and Emulator methods. The x-axis represents the average of the APD90 values from both methods, calculated as Average in (5.5). The y-axis shows the difference between the APD90 values produced by the Emulator and the Simulator, expressed as Difference in (5.6). The dashed lines represent the limits of agreement (± 1.96 standard deviations), providing a visual assessment of the consistency between the two methods and highlighting any potential bias.

For the given values $\text{APD90}_{\text{sim}} = 249$ and $\text{APD90}_{\text{emu}} = 248$, the Average APD90 is 248.5 and the difference in APD90 is -1. The calculate the percentage difference relative to $\text{APD90}_{\text{emu}}$ is:

$$\text{Percentage Difference} = \left(\frac{\text{Difference in APD90}}{\text{APD90}_{\text{emu}}} \right) \times 100 \approx -0.4032\% \tag{5.7}$$

The calculated percentage difference between the emulator and simulator APD90 values is approximately -0.40%. This result indicates that the APD90 value predicted by the emulator is slightly lower than that of the simulator by 0.40%. The small magnitude of this difference suggests that the emulator is highly accurate and closely approximates the simulator's performance, thus providing reliable predictions.

5.3.2 Visualisations of Experimental Data

In the study by Lachaud et al. (Lachaud et al. 2022), the drug Dofetilide was administered at a concentration of 30 nM to induce a blockade of the hERG channels. This inhibition of the rapid delayed rectifier potassium current (IKr) resulted in a prolonged action potential duration (APD). In contrast to the effects of Dofetilide, the inhibition of L-type calcium channels by 1 μM Nifedipine led to a shortening of the APD. Figure 5.5 shows the distribution of action potential duration in the experiments conducted by (Lachaud et al. 2022). The histograms illustrate the impact of both drugs on the measurements of APD biomarkers before and after the application of drugs. To ensure the effectiveness of rejection sampling, it is crucial that the kernel density estimate (KDE) generated by the Gaussian Process (GP) emulator fully encompasses the KDE derived from the experimental data. If this condition is not met, the rejection sampling method will fail to properly filter out models that produce unphysical results. This requirement guarantees that the sampled models align closely with the distribution of biomarkers observed in the experimental data, thereby maintaining the validity of the model population. However, as illustrated in Figure 5.6, there were instances where the KDE of the APD90 measurements did not fully overlap between the GP emulator and the experimental data, both before and after drug inhibition.

To address this issue, it is necessary to introduce a scaling factor, denoted as k, which ensures that the scaled GP emulator's KDE fully encompasses the target KDE from the experimental observations. This scaling factor k, as explained in the methods section, is determined by the maximum ratio between the GP emulator's density and the experimental data density. By scaling the proposal distribution (GP emulator) with this factor, we adjust the distribution so that it reliably covers the entire range of the target distribution. For each case examined, we

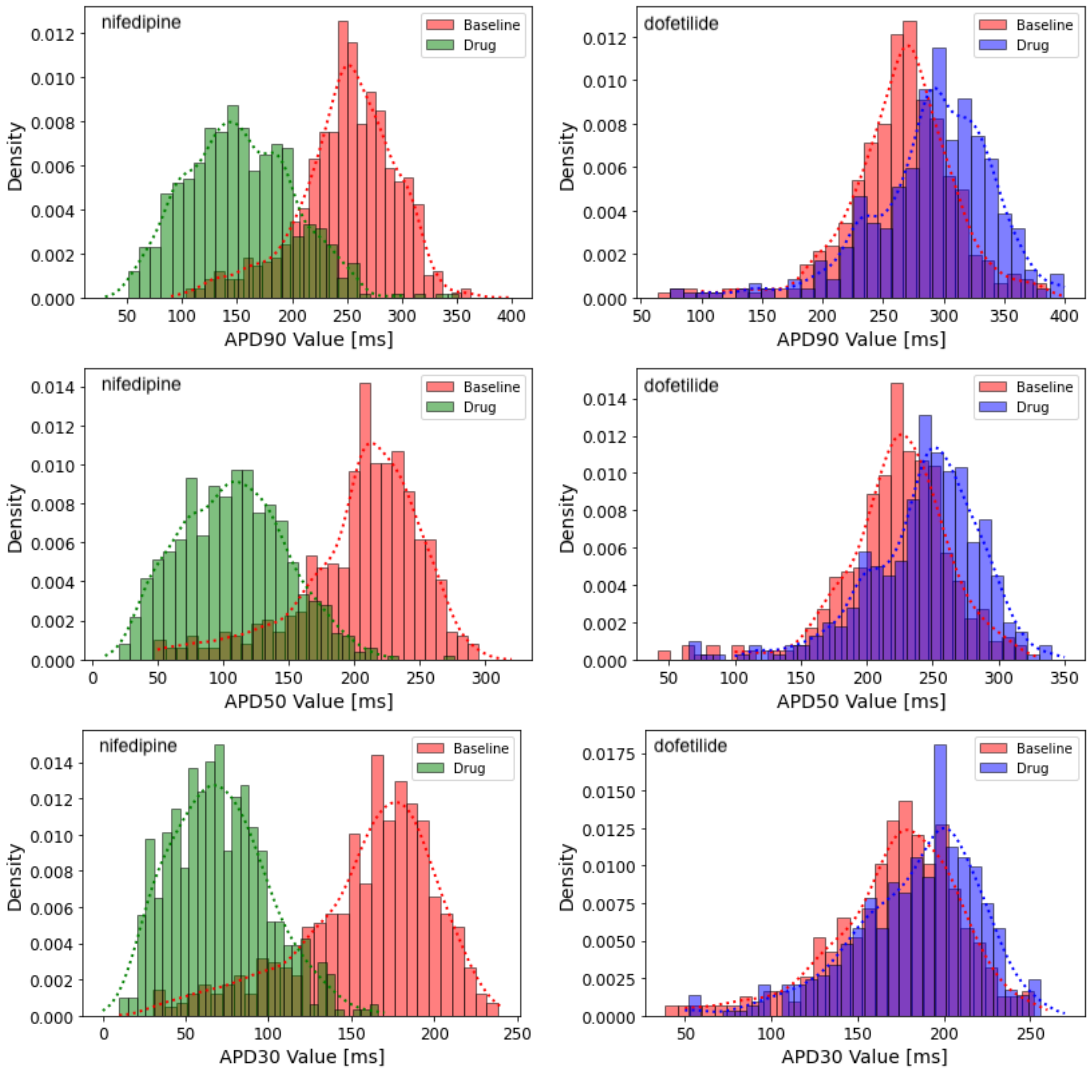

Figure 5.5: Histograms illustrating the distribution of action potential duration (APD) biomarkersAPD90, APD50, and APD30both at before drug and after drug application in the study by Lachaud et al. (Lachaud et al. 2022). The figure comprises a total of 12 histograms, with datasets representing the experimental measurements before and after the administration of two drugs: 1 μM Nifedipine, which inhibits L-type calcium channels and results in a shortening of the APD, and 30 nM Dofetilide, which blocks hERG channels and leads to a prolonged APD. Each set of histograms compares the changes in APD90, APD50, and APD30, providing a detailed visual representation of the drug's effects on the action potential duration across different biomarkers.

calculated the appropriate value of k and applied it to scale the GP emulator. We then provided an additional visualisation, shown in Figure 5.7, to confirm that the scaled proposal distribution consistently exceeds the target distribution, thereby ensuring the effectiveness of the rejection sampling process.

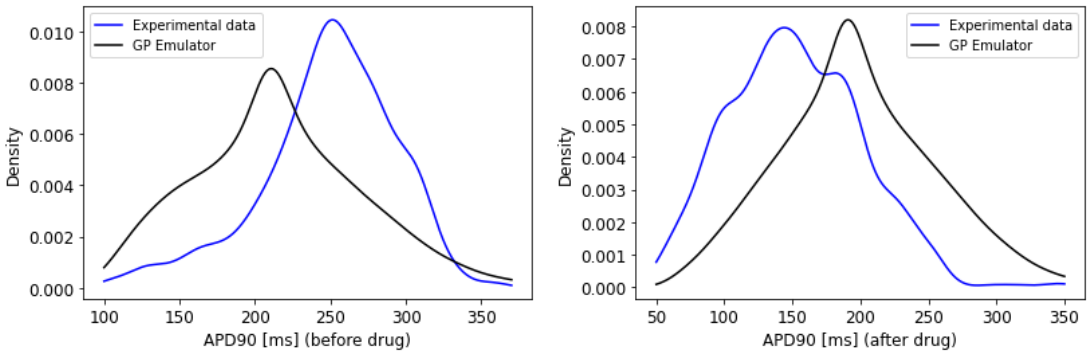

Figure 5.6: This plot illustrates the Kernel Density Estimates (KDE) for APD90 measurements generated by the Gaussian Process (GP) emulator compared to those derived from experimental data, both before and after drug inhibition. The figure highlights instances where the KDEs do not fully overlap, indicating differences between the emulator's predictions and the observed experimental distributions.

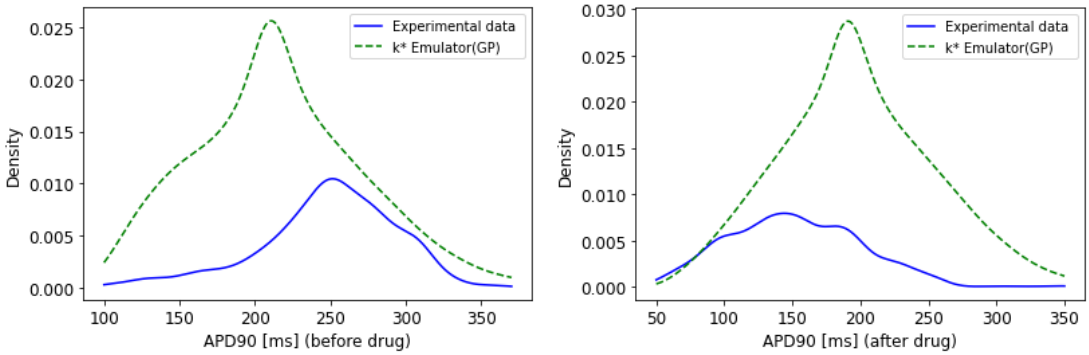

Figure 5.7: This figure shows the scaled Kernel Density Estimate (KDE) of the GP emulator for APD90 after multiplying by the scaling factor k to ensure that the KDE of the GP emulator does fully encompass the experimental KDE. This visualisation confirms that the scaled distribution consistently exceeds the target distribution, thereby enhancing the effectiveness of the rejection sampling process.

5.3.3 Biomarker Distributions in each Model Population

We utilised one million iterations to initialise our rejection sampling procedure, yielding a population of 10,000 acceptable models before and after the drug. However, it is important to emphasise that these choicesone million iterations and 10,000 modelsshould not be interpreted as measures of the method's efficiency but they reflect the specific parameters chosen for this study and the stringent criteria used to ensure that only models closely matching the desired characteristics were retained. In Figure 5.8, the APD90 distributions from the Nifedipine dataset are represented in blue, while the distributions from the sampled models generated through the rejection sampling method are shown in red. The rejection sampling approach effectively produced model populations that closely mirror the variability observed in

the experimental data. This successful alignment indicates that using rejection sampling with GP emulators for distributional calibration significantly enhances the accuracy of the model populations in reflecting the characteristics of the experimental datasets. Until recently, the

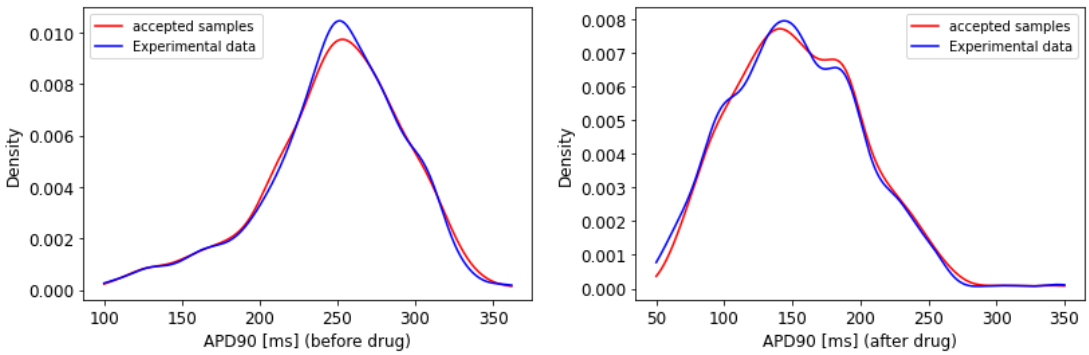

Figure 5.8: The left subplot shows the distribution of APD90 from the experimental data (blue) and the sampled data (red) before Nifedipine administration, while the right subplot illustrates the same distributions after the drug application. The alignment of these distributions indicates the accuracy of the rejection sampling method in capturing the effects of Nifedipine on APD90.

calibration of model populations has largely involved excluding any simulated models that produce outputs inconsistent with the observed values in the dataset (Muszkiewicz et al. 2016). In two recent studies in cardiac electrophysiology (Lancaster and Sobie 2016 and Tixier et al. 2017), parameter values were selected to ensure that the models collectively exhibited the appropriate mean and standard deviation for the experimental measurements of interest. One approach, as described in the study by (Lawson et al. 2018), involved randomly scaling cellular parameters to generate variability in ion-channel expression using the sequential Monte Carlo (SMC) algorithm. In the work by (Lachaud et al. 2022), a more straightforward method was employed, in which they generated 3,425 Shannon models that were accepted into the control population by fitting the distribution of the models to the experimental data.

The rejection sampling procedure in this chapter effectively generated a population of models that accurately captures the distribution of outputs for the two ion channel block datasets, both of which exhibit significant variability among individual cells. Table 5.3 demonstrates a perfect match, with identical mean values for APD outputs across the model populations from our study and the experimental data (Lachaud et al. 2022).

Setting	Mean	APD90	APD50	APD30
Basline Nif.	Experiment	249	204	159
	Population	248	203	159
Drug Nif.	Experiment	152	107	70
	Population	154	109	69
Basline Dof.	Experiment	264	221	171
	Population	264	221	171
Drug Dof.	Experiment	289	242	183
	Population	289	241	180

Table 5.3: All biomarkers show a perfect agreement with identical mean values in the model distribution and experiments by (Lachaud et al. 2022)

5.3.4 Statistical Analysis

To assess the effectiveness of our technique, we utilised a statistical tool known as the Quantile-Quantile (QQ) plot. This graphical method is particularly useful for comparing two datasets to determine if they originate from the same distribution, and it is commonly employed to check the assumption of normality in statistical analyses. The QQ plot functions by plotting the quantiles of one dataset against the corresponding quantiles of another. If the datasets share the same distribution, the points on the QQ plot will approximately align along a 45-degree line through the origin. Deviations from this line suggest differences between the distributions; for instance, an S-shaped curve may indicate that the data has heavier tails than the reference distribution.

We generated a QQ plot to compare the quantiles of the experimental distribution (plotted on the x-axis) with those of the sampled data obtained through rejection sampling (plotted on the y-axis). As shown in Figure 5.9, the majority of data points closely align with the diagonal line, indicating a strong agreement between the sampled and experimental distributions. This alignment suggests that our rejection sampling technique effectively captures the overall distribution of the experimental data.

The QQ plot is particularly valuable as it not only allows for the evaluation of overall similarity between distributions but also facilitates the identification of specific deviations due to variations in the data. This capability is crucial for diagnosing assumptions in statistical models, such as the normality assumption in linear regression. Despite the strong overall agreement, our analysis also revealed that each model population exhibited notable variations compared to the experimental dataset for different model outputs, highlighting the inherent variability within the models.

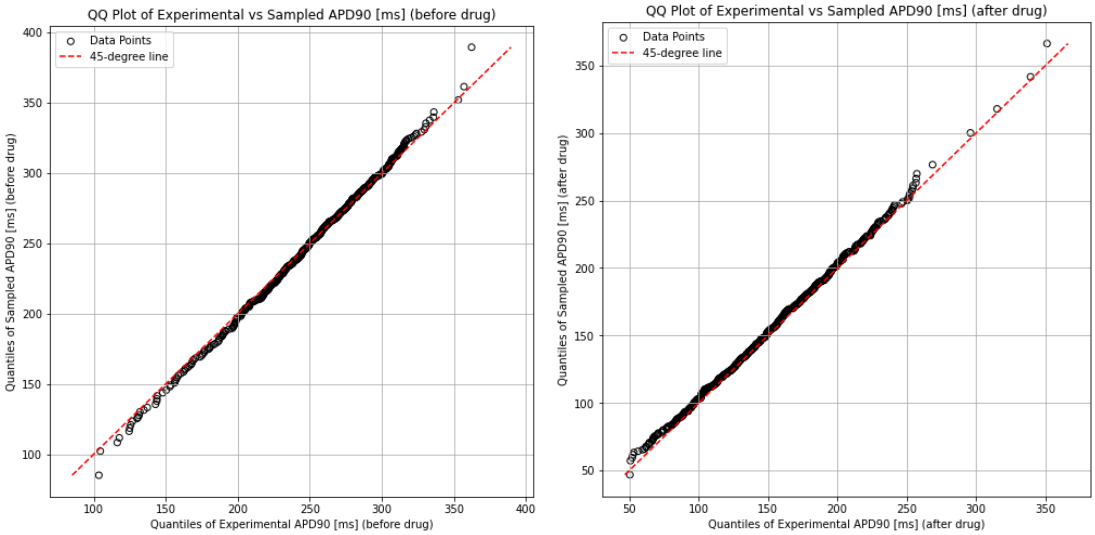

Figure 5.9: QQ plot. On the x-axis are the quantiles of the experimental distribution and on the y-axis are the quantiles of the sampled data, where the left plot corresponds to before drug and the after drug is on the right.

5.3.5 Distributions of Ion Channel Conductances in the Sampled Population of Models

The aim of this chapter is to identify the distributions of ion channel conductance values that accurately reflect the variability in electrophysiological characteristics observed across a large population of cells. We employed rejection sampling with Gaussian Process (GP) emulators to generate a population of models, which were then used to quantitatively predict the range of responses to two ion channel blocks. Our methodology was applied to the rabbit action potential (AP) model proposed by Shannon (Shannon et al. 2004) to evaluate the accuracy of the cell models in predicting drug effects. We also investigated and compared the variability in parameter distributions within the accepted model population for each AP model.

The data presented in Figure 5.10 shows that the majority of conductance values span the entire sampling range (0.12 times the baseline value for each conductance). This highlights the robustness of the Shannon rabbit action potential model to variations in conductance values. In both the before drug and drug-affected populations of APD90, the median conductance values generally align with the baseline value of 1, with the exceptions of gCaL and gNaCa.

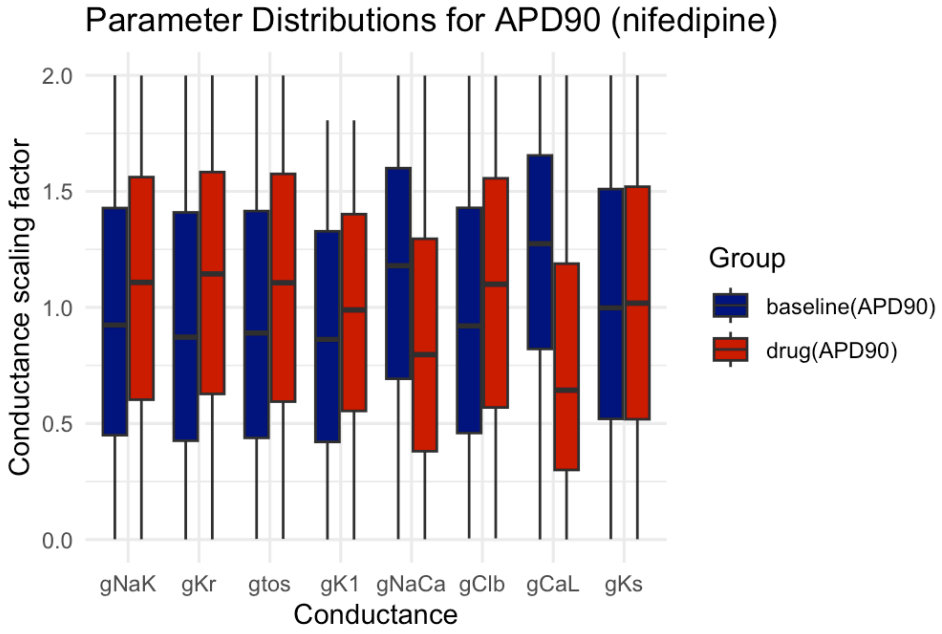

Figure 5.10: Box plot of selected parameter distributions in the Shannon model population for both before drug and drug response APD90. The lower and upper box boundaries are the 25^{th} and 75^{th} percentiles, respectively. The median is denoted by a solid black line inside the box

5.3.6 Partial Correlation Coefficient for Model Biomarkers

Ionic currents display consistent behaviour across different phases of the action potential, with some currents being particularly sensitive to changes, potentially leading to alterations in the shape of the action potential. We investigated whether there were any relationships between the parameter values in the models of each population and the APD biomarkers. To explore these relationships, we used the partial correlation coefficient (PCC) plot, which illustrates the relationship between a biomarker and the corresponding conductances within the population, while controlling for the influence of other variables. The PCC plot is invaluable for understanding the unique relationships between variables, as it isolates the direct effects by removing the confounding influence of other factors.

In Figure 5.11, the PCC plot demonstrates how each conductance variable is related to APD90 after accounting for the effects of the other conductance variables, thereby clarifying the direct relationship between APD90 and each specific conductance. Notably, the conductance variables gCaL and gNaCa show a direct correlation, where an increase in these conductances is associated with an increase in APD90 when other variables are controlled for. Conversely, gNaCa, gKr, gtos, and gClb exhibit an inverse correlation, where an increase in any of these conductances is associated with a decrease in APD90, again controlling for other variables. Interestingly, in the Nifedipine drug population models, the conductance gK1 demonstrates a negative correlation with APD90, yet it shows a weaker relationship with APD90 in other populations.

In Figure (5.11), the PCC plot shows how each conductance variable is related to APD90 after accounting for the effects of the other conductance variables, which helps in understanding the direct relationship between APD90 and each conductance variable. Clearly, gCaL and gNaCa have a direct relationship, where an increase in these conductance variables is associated with

an increase in APD90 when controlling for other variables. While, all of gNaK, gKr, and gtos exhibit an inverse correlation, wherein an increase in any of this conductance is associated with a drop in APD90 while controlling for other variables. Notably, after application of the drug Nifedipine, the conductance gK1 established a negative correlation with APD90.

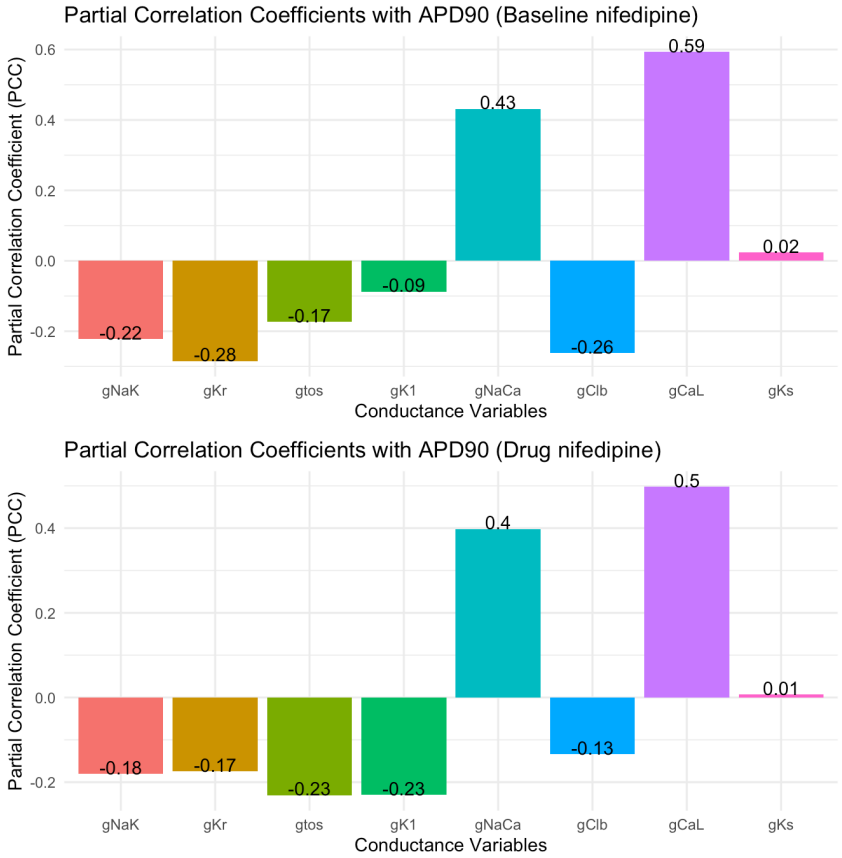

Figure 5.11: Partial correlation coefficient (PCC) plot for APD90 and the corresponding conductances in before drug (top) and after drug population (Nifedipine) (bottom)

5.3.7 Correlation Between Ion Conductances of Model Populations

We generated 2D density plots to visualise the distributions of specific pairs of ionic conductances within the populations of the Shannon model. The KDE approach allows us to identify regions of high and low density within the data. These plots reveal that most conductance parameters span nearly the entire range, extending up to $\mp 100\%$ of their original values from the baseline model. The only notable exception is g_{CaL}, which occupies the upper half of the sampled g_{CaL} range, as shown in Figure 5.12 for the baseline population. This distribution suggests a consistent tendency for g_{CaL} to remain near its upper limit in the sampled populations, which may have significant implications for the overall electrophysiological behaviour of the model.

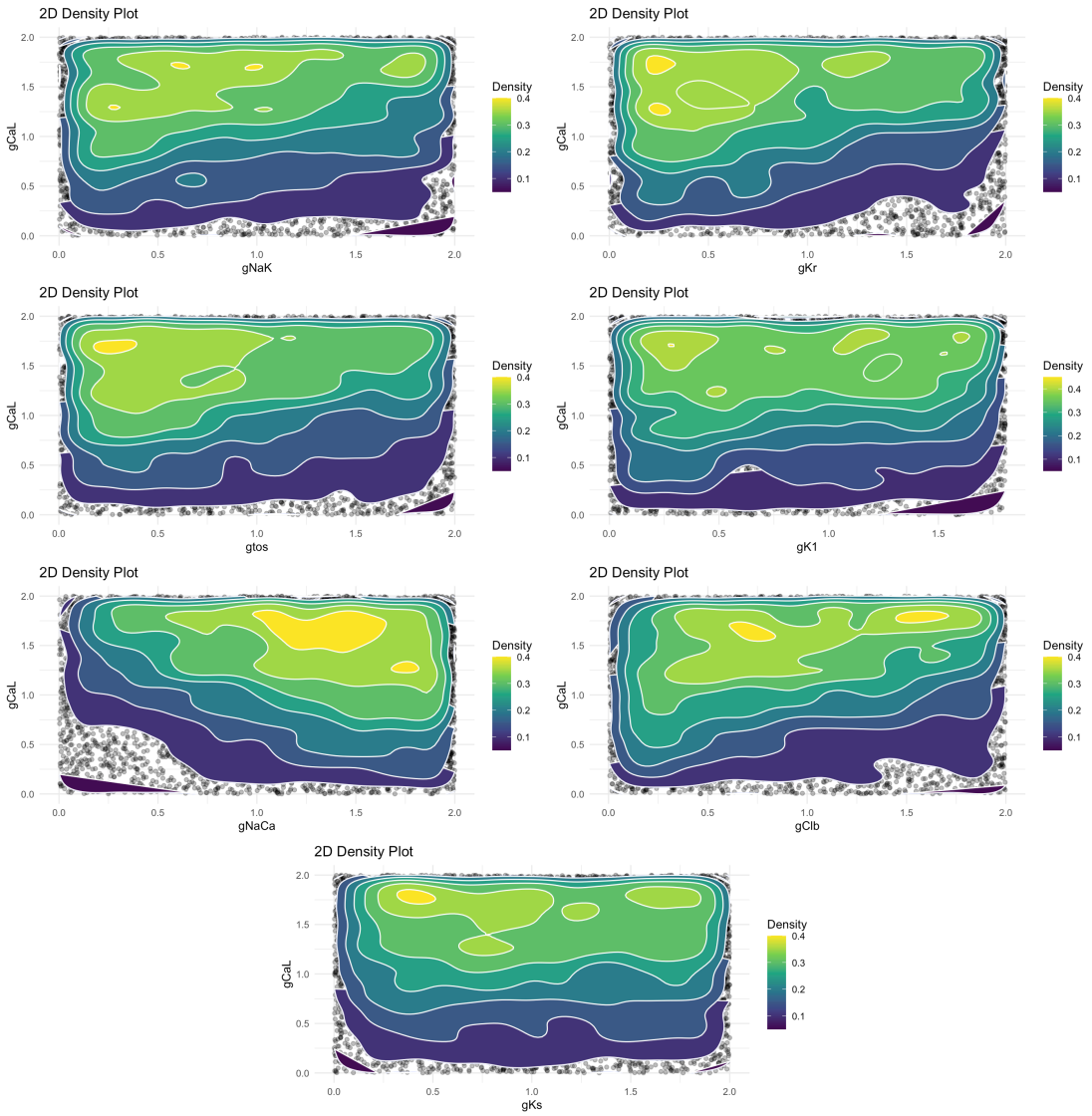

Figure 5.12: The figure presents a series of seven 2D density plots, each visualising the relationship between the calcium current conductance g_{CaL} and one of the other ionic conductances within the Shannon model populations. The plots were generated to illustrate how g_{CaL} correlates with g_{NaK}, g_{Kr}, g_{Ktos}, g_{K1}, g_{NaCa}, g_{Clb}, and g_{Ks}. Each plot was created using kernel density estimation (KDE) to capture the density of the data points, with g_{CaL} plotted on the y-axis and the corresponding conductance on the x-axis.

Additionally, pair plots were created to visually summarise the correlations between the same pairs of conductances in the populations both before and after the application of the drug, as illustrated in Figure 5.13. The plot consists of three key elements: the upper diagonal shows the correlation coefficients, providing a quantitative measure of the strength and direction of the relationships between each pair of conductances; the diagonal presents the Kernel Density Estimates (KDE) for each conductance, illustrating the distribution of values within the population; and the lower diagonal features scatter plots, visually representing the relationship between each pair of conductances.

This comprehensive visualisation highlights how the application of the drug influences the correlations and distributions of the ion conductances in the model population.

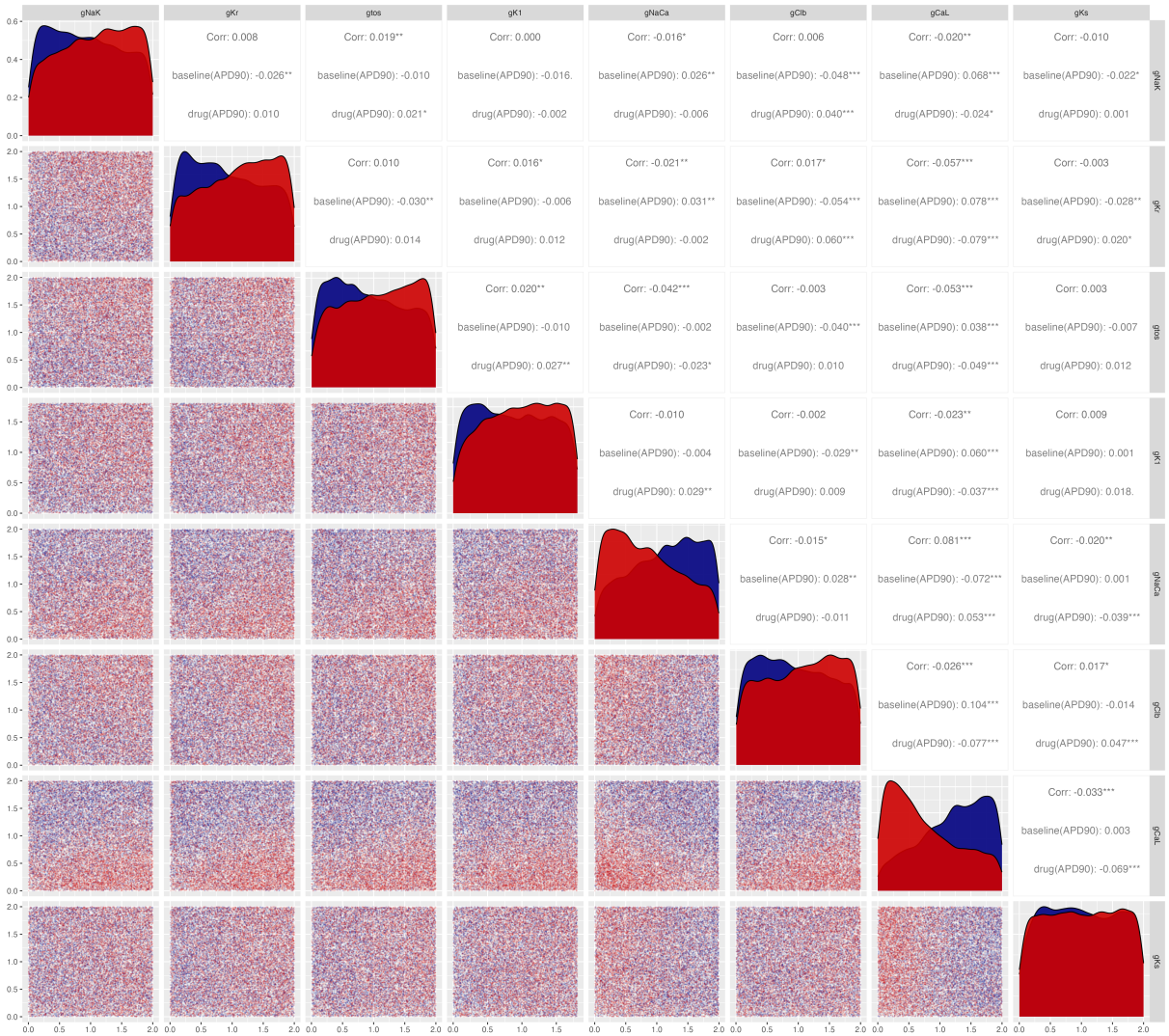

Figure 5.13: Pair plot visualising the relationships between conductances in the sampled APD90 population before and after Nifedipine administration. The navy colour represents the conductances before the drug, while the red colour represents the conductances after the drug application. The plot includes three key elements: the upper diagonal shows the correlation coefficients, indicating the strength and direction of relationships between conductance pairs; the diagonal displays the Kernel Density Estimates (KDE) for each conductance, illustrating the distribution of values within the population; and the lower diagonal presents scatter plots that provide a visual representation of the relationships between conductance pairs. This comprehensive visualisation effectively demonstrates the impact of Nifedipine on the correlations and distributions of ion conductances within the model population.

To assess the effect of particular ion channels on the duration of the action potential (APD) through pharmacological reactions, we undertake an investigation to precisely determine the change in the distribution of specific conductance before and after the application of the drug. We perform an analysis to examine the distribution of ionic conductances in the population before and after administering the drug Nifedipine. We begin with two datasets that represent the values of the conductances corresponding to APD90 before and after the application of the drug, respectively. Each dataset has the eight conductances of the currents listed in Table (5.1).

To begin our analysis, we applied Kernel Density Estimation (KDE) to each conductance in both datasets (before and after drug) to represent their distributions. KDE provides a smoothed estimation of the probability density function for a stochastic variable, allowing for a clearer understanding of the underlying distribution. We generated KDEs for each conductance and compared them visually before and after drug application, refer to Figure 5.14. These plots of KDEs helped us observe how the distribution of each conductance was affected by the drug.

Following this, we selected specific data points from the KDE before the drug application (1000 points; 10% of the data points) and examined how these points shifted or changed after the drug was introduced. This approach enabled us to gain insights into the impact of the drug on the conductance distributions.

Let the KDE of a conductance g before the drug application be K_b, and K_a be the KDE of g after the application of the drug. For each selected point x_b on K_b, we have:

$$y_b = K_b\,(x_b), \tag{5.8}$$

and similarly, for points on K_a:

$$y_a = K_a\,(x_a). \tag{5.9}$$

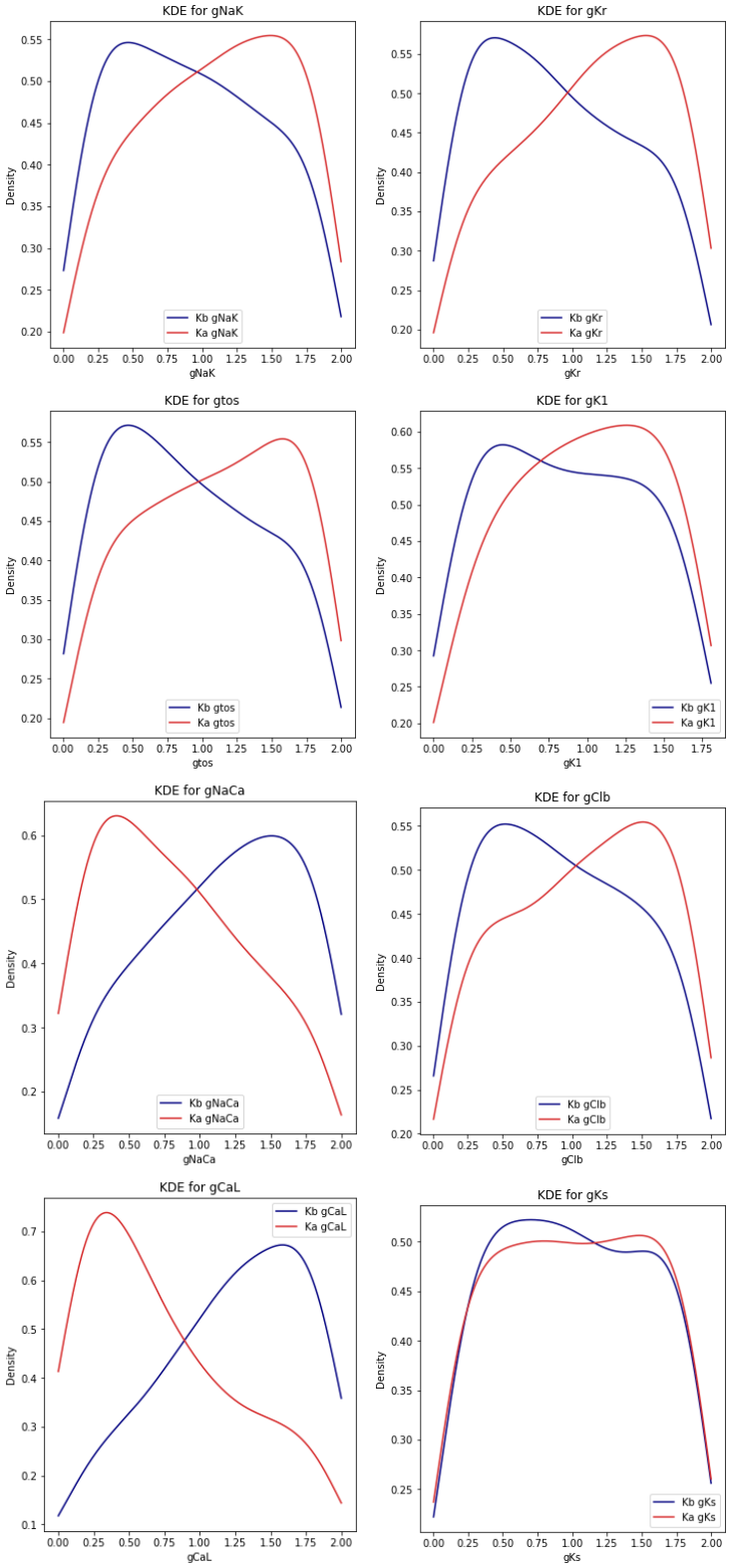

Figure 5.14: Kernel Density Estimation (KDE) plots illustrating the distributions of each ionic conductance before drug (navy lines) and drug-applied datasets (red lines). These plots provide a smoothed estimation of the probability density functions, enabling a visual comparison of how the distributions of the conductances change after drug application.

Since x_a is the value after the drug, we can write it as $x_a = (\alpha \cdot x_b)$, where α is a multiplicative factor representing the drug action applied to x_b.

Then we have:

$$K_b(x_b) = K_a(\alpha x_b). \tag{5.10}$$

For each selected point, we solve the equation (5.10) above for α, to identify the new value (αx_b) on the K_a distribution corresponding to each point x_b on the K_b distribution. To analyse the change in x_b we compute the derivative of K_b with respect to x_b to determine whether it is increasing or decreasing at each point. Based on this derivative, we decide which root (it could be more than one root) to accept as the new value after the drug action. To visualise we plot the roots (the solutions to the equation (5.10)) and the selected α values against the selected points from x_b.

Figure 5.15 shows how each point on the K_b distribution maps to the K_a distribution after the drug application. By systematically comparing the KDEs and analysing the transformation of specific points due to the drug, we gain insights into the effects of Nifedipine on the conductance values of APD90. This method provides a detailed understanding of how each conductance is affected by the drug, which can be crucial for further pharmacological studies and applications. When the α curve follows a root curve and then jumps to another root curve at some point, this behaviour can be interpreted in the context of the sign of the derivative of $K_b\,(x_b)$. As the alpha curve represents the scaling factor applied to x_b that makes the densities $K_b\,(x_b)$ and $K_a\,(\alpha x_b)$ equal. The derivative dK_b/dx_b indicates the rate of change of the density K_b with respect to x_b. When $dK_b/dx_b \geq 0$, it suggests that K_b is increasing or staying constant as x_b increases. In this case, the α value follows the first root curve. When $dK_b/dx_b < 0$, it suggests that K_b is decreasing as x_b increases. This is the point where the α value may jump to the other root curve, which provides the alternative solution.

The jump in the α curve from the first root to another root indicates a transition in the relationship between the densities K_b and K_a. This transition is closely related to the change in the sign of dK_b/dx_b. When the derivative changes sign, it signifies a shift in the density behaviour, prompting the α value to switch to the other root to maintain the equality $K_b\,(x_b) = K_a\,(\alpha x_b)$.

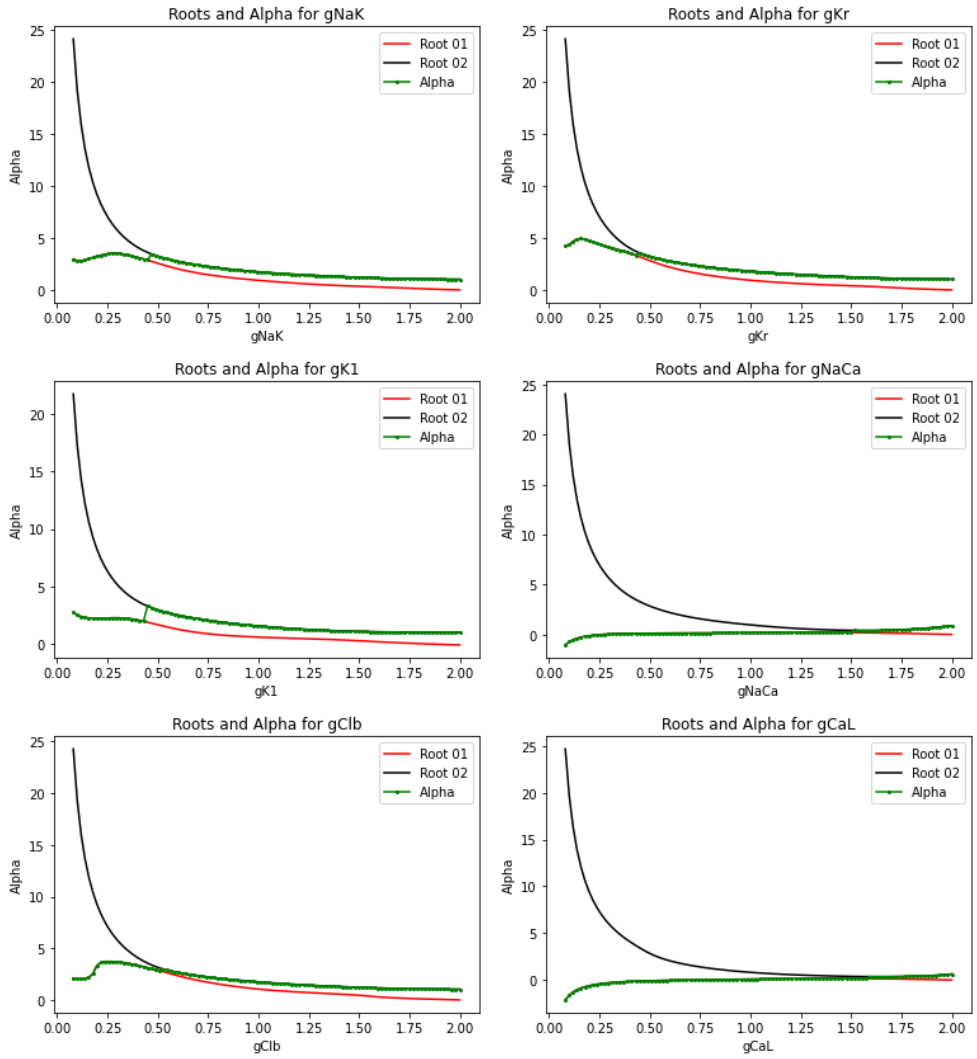

Figure 5.15: Visualisation of the mapping of specific data points from the Kernel Density Estimation (KDE) of conductance K_b (before drug application) to the KDE K_a (after drug application). The figure illustrates how each selected point x_b on distribution K_b shifts to a new value $\alpha \cdot x_b$ on the post-drug distribution K_a due to the application of Nifedipine. The roots of the equation $K_b(x_b) = K_a(\alpha \cdot x_b)$ are plotted to show the transformation, with the corresponding α values indicating the extent of change for each point. Notably, the figure reveals a jump from a root to another (root01 & root02 respectively) in the mapping process, highlighting a significant shift in conductance values due to the drug. This jump provides further insights into the non-linear effects of Nifedipine on the conductance values associated with APD90, offering a more detailed understanding of the drug's impact on the electrophysiological properties of the model.

Two conductances, g_{tos}, and g_{Ks}, exhibited unique behaviour, with gaps appearing where no roots could be found. This occurred because the KDE for the before drug condition (K_b) was higher than the KDE after drug application (K_a) over certain ranges, leading to intervals where the equation $K_b(x_b) = K_a(\alpha x_b)$ had no solutions. To address this issue, we made adjustments to our calculations, enabling us to resolve the problem. In Figure 5.16, these special cases are illustrated, clearly showing intervals where no solutions exist and where the value of α does not correspond to either of the roots.

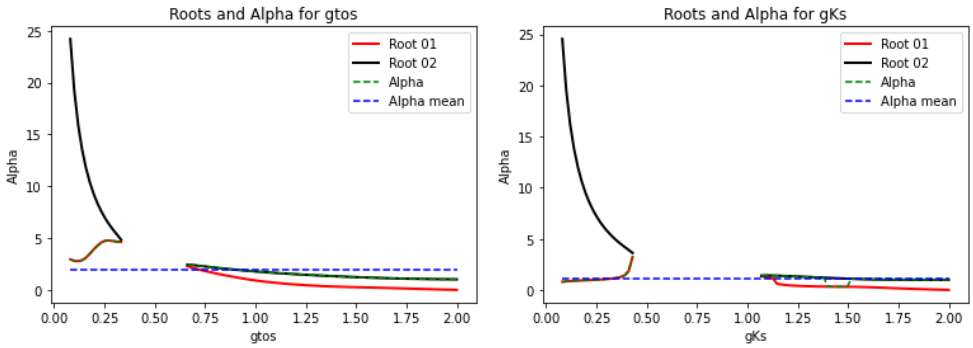

Figure 5.16: Visualisation of special cases for conductances g_{tos} and g_{Ks}, where gaps with no roots were identified. The figure illustrates intervals where the KDE (K_b) before the drug action exceeds the post-drug KDE (K_a), resulting in regions without solutions to the equation $K_b(x_b) = K_a(\alpha x_b)$. These intervals are marked by a lack of corresponding α values following the roots, highlighting the challenges in mapping conductance values when the before drug distribution is higher than the post-drug distribution.

5.4 Distributions of APD50 and APD30 in Nifedipine Population

In Figures 5.17 and 5.18, the distributions of APD50 and APD30 respectively from the Nifedipine dataset are represented in blue, while the distributions from the sampled models generated through the rejection sampling method are shown in red. The rejection sampling approach effectively produced model populations that closely mirror the variability observed in the experimental data. This successful alignment indicates that using rejection sampling with GP emulators for distributional calibration significantly enhances the accuracy of the model populations in reflecting the characteristics of the experimental datasets.

5.5 Distributions of APD90, APD50 and APD30 in Dofetilide Population

The following figures compare the distributions of APD90, APD50, and APD30 between the experimental data from Dofetilide administration and the sampled data generated through the rejection sampling method. Each figure includes two subplots: the left shows the distribution before the drug was applied, and the right shows the distribution after the drug application. These comparisons help to assess the effectiveness of the rejection sampling method in replicating the experimental variability observed in response to Dofetilide.

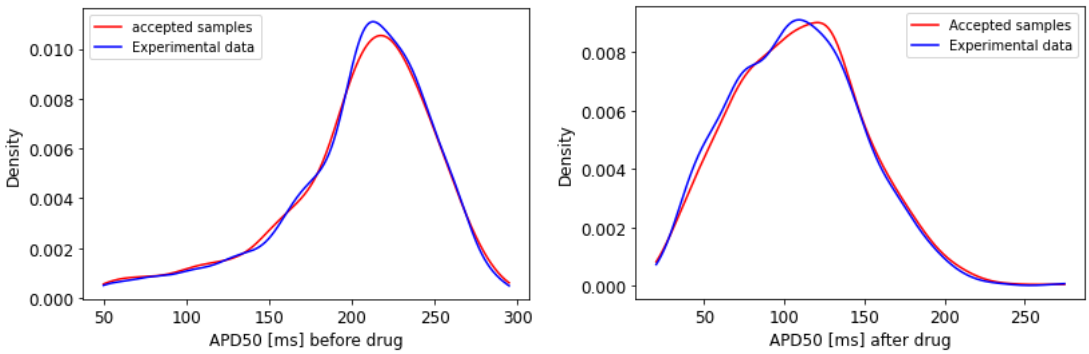

Figure 5.17: A comparison of the APD50 distributions between the Nifedipine experimental dataset (blue) and the model populations generated via rejection sampling (red). The left panel shows the distributions before the drug application, while the right panel displays the distributions after the drug application. The strong similarity between the two distributions highlights the success of the rejection sampling method with GP emulators in precisely capturing the variability seen in the experimental data.

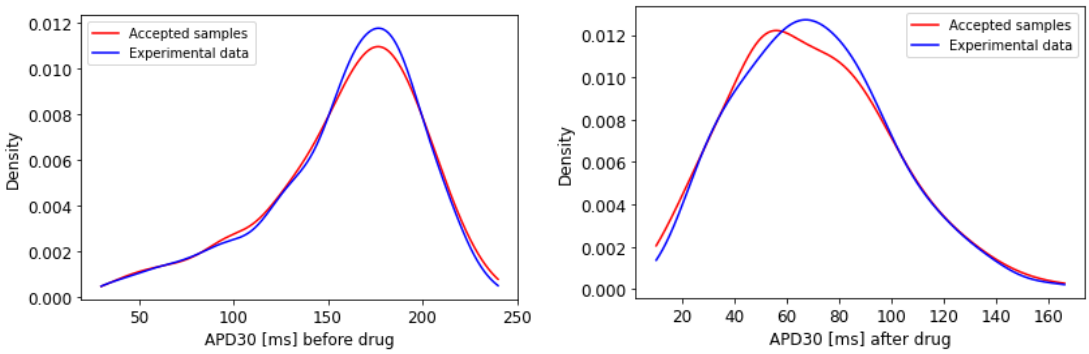

Figure 5.18: A comparison of the APD30 distributions between the Nifedipine experimental dataset (blue) and the model populations generated via rejection sampling (red). The left panel shows the distributions before the drug application, while the right panel displays the distributions after the drug application. The close alignment between the experimental and model distributions demonstrates the effectiveness of the rejection sampling method in capturing and replicating the observed experimental variability in the model populations.

5.6 Distributions of ion conductances

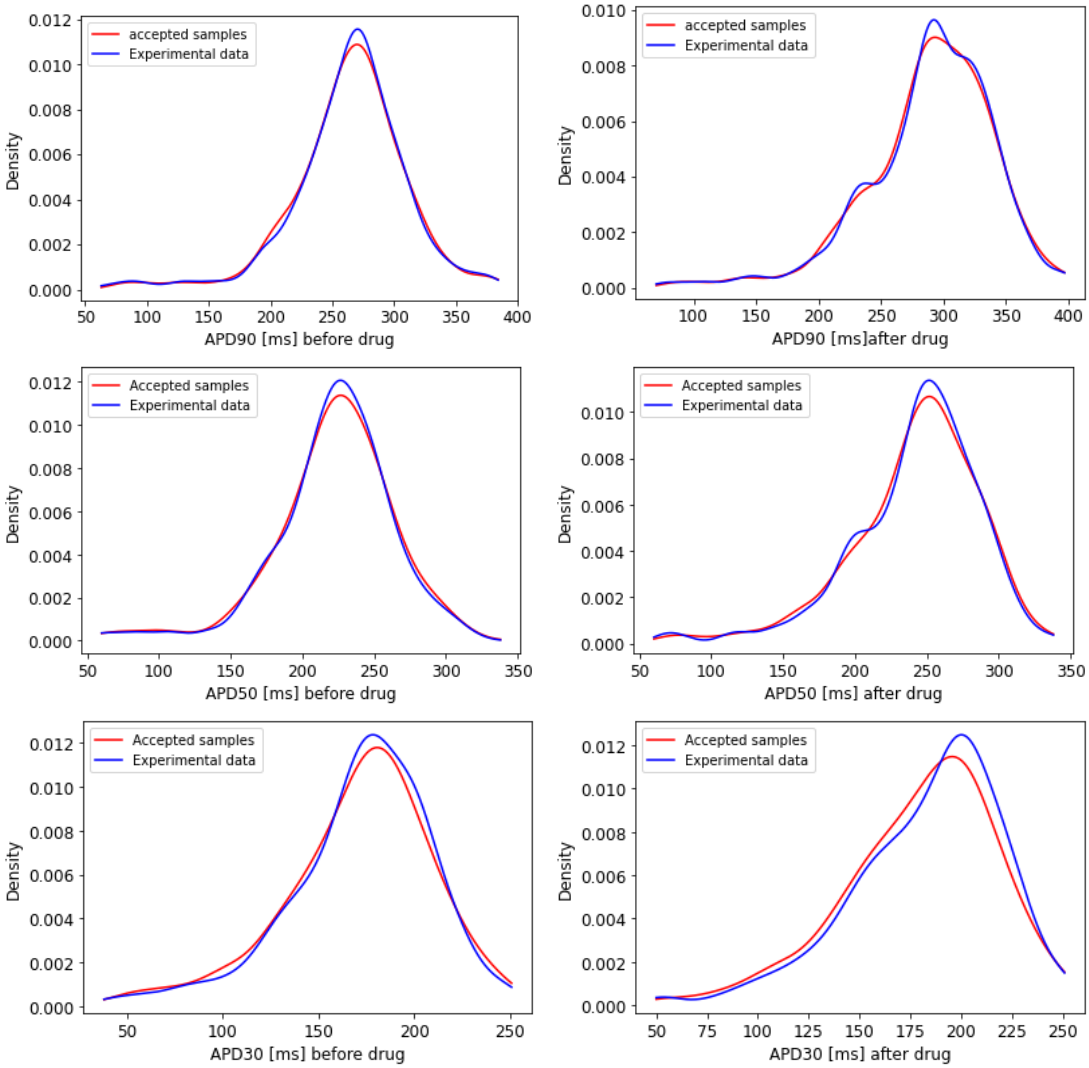

Figure 5.19: The figure compares the distributions of APD90, APD50, and APD30 between experimental data from Dofetilide administration and the sampled models generated through the rejection sampling method. The left column (from top to bottom) shows the distributions of APD90, APD50, and APD30 before drug application, while the right column presents the same distributions after drug administration. APD90 and APD50 exhibit strong alignment between experimental and sampled data, indicating successful replication of variability. However, the APD30 distribution shows less accuracy in capturing the experimental variability.

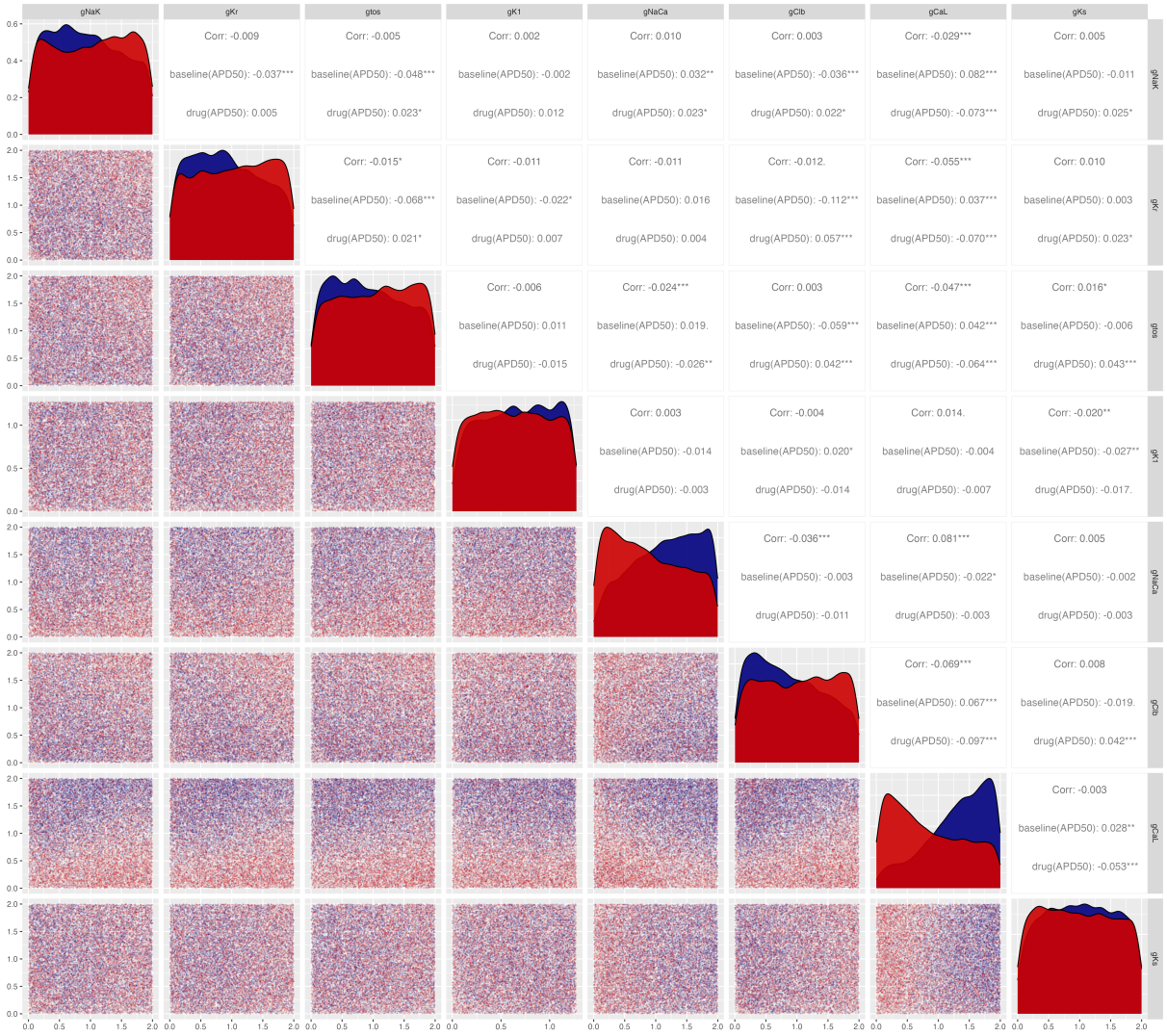

Figure 5.20: Pair plot visualising the relationships between conductances in the sampled APD50 population before and after Nifedipine administration. The navy colour represents the conductances before the drug, while the red colour represents the conductances after the drug application. The plot includes three key elements: the upper diagonal shows the correlation coefficients, indicating the strength and direction of relationships between conductance pairs; the diagonal displays the Kernel Density Estimates (KDE) for each conductance, illustrating the distribution of values within the population; and the lower diagonal presents scatter plots that provide a visual representation of the relationships between conductance pairs. This comprehensive visualisation effectively demonstrates the impact of Nifedipine on the correlations and distributions of ion conductances within the model population.

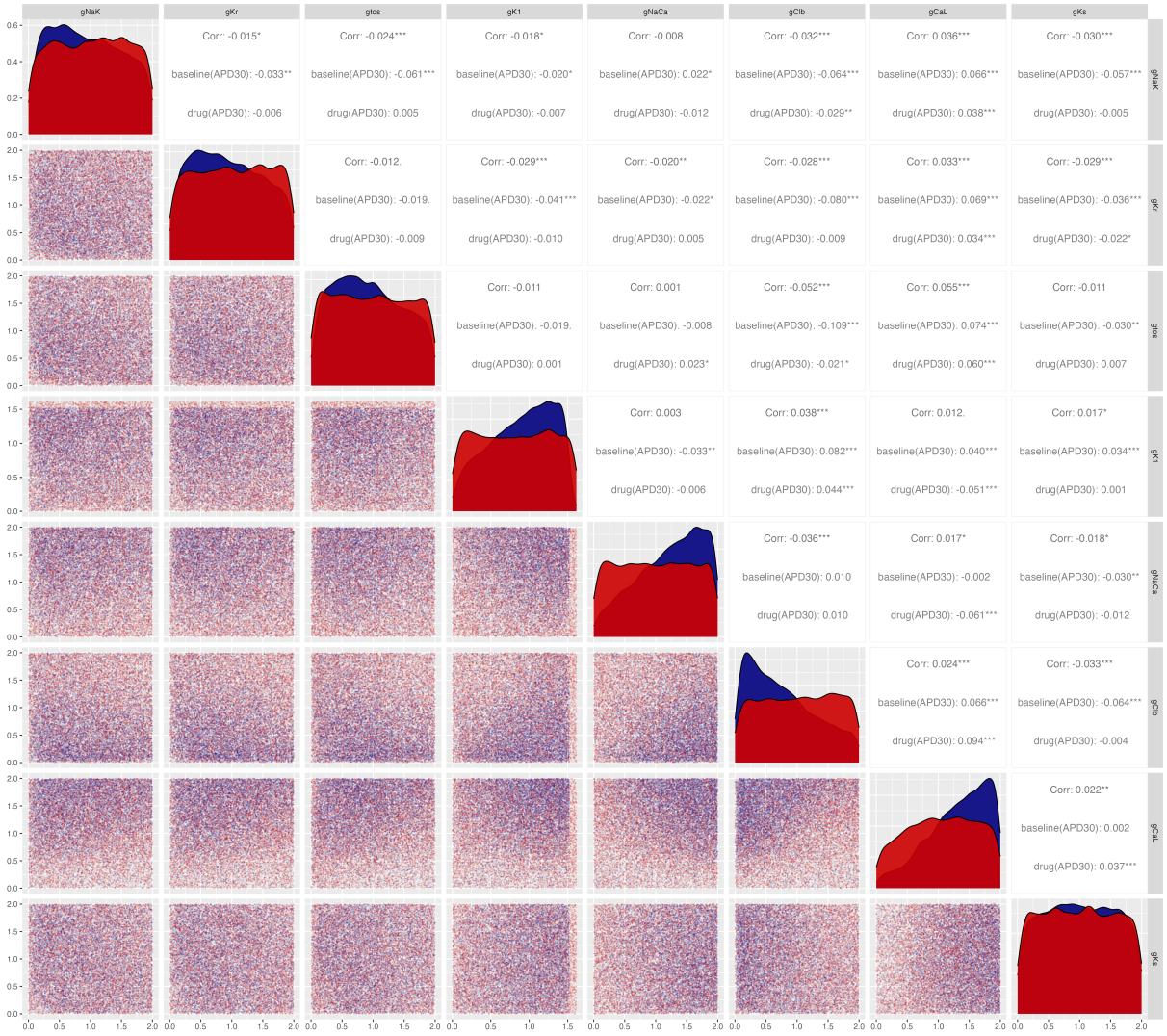

Figure 5.21: Pair plot visualising the relationships between conductances in the sampled APD30 population before and after Nifedipine administration. The navy colour represents the conductances at baseline (before the drug), while the red colour represents the conductances after the drug application. The plot includes three key elements: the upper diagonal shows the correlation coefficients, indicating the strength and direction of relationships between conductance pairs; the diagonal displays the Kernel Density Estimates (KDE) for each conductance, illustrating the distribution of values within the population; and the lower diagonal presents scatter plots that provide a visual representation of the relationships between conductance pairs. This comprehensive visualisation effectively demonstrates the impact of Nifedipine on the correlations and distributions of ion conductances within the model population.

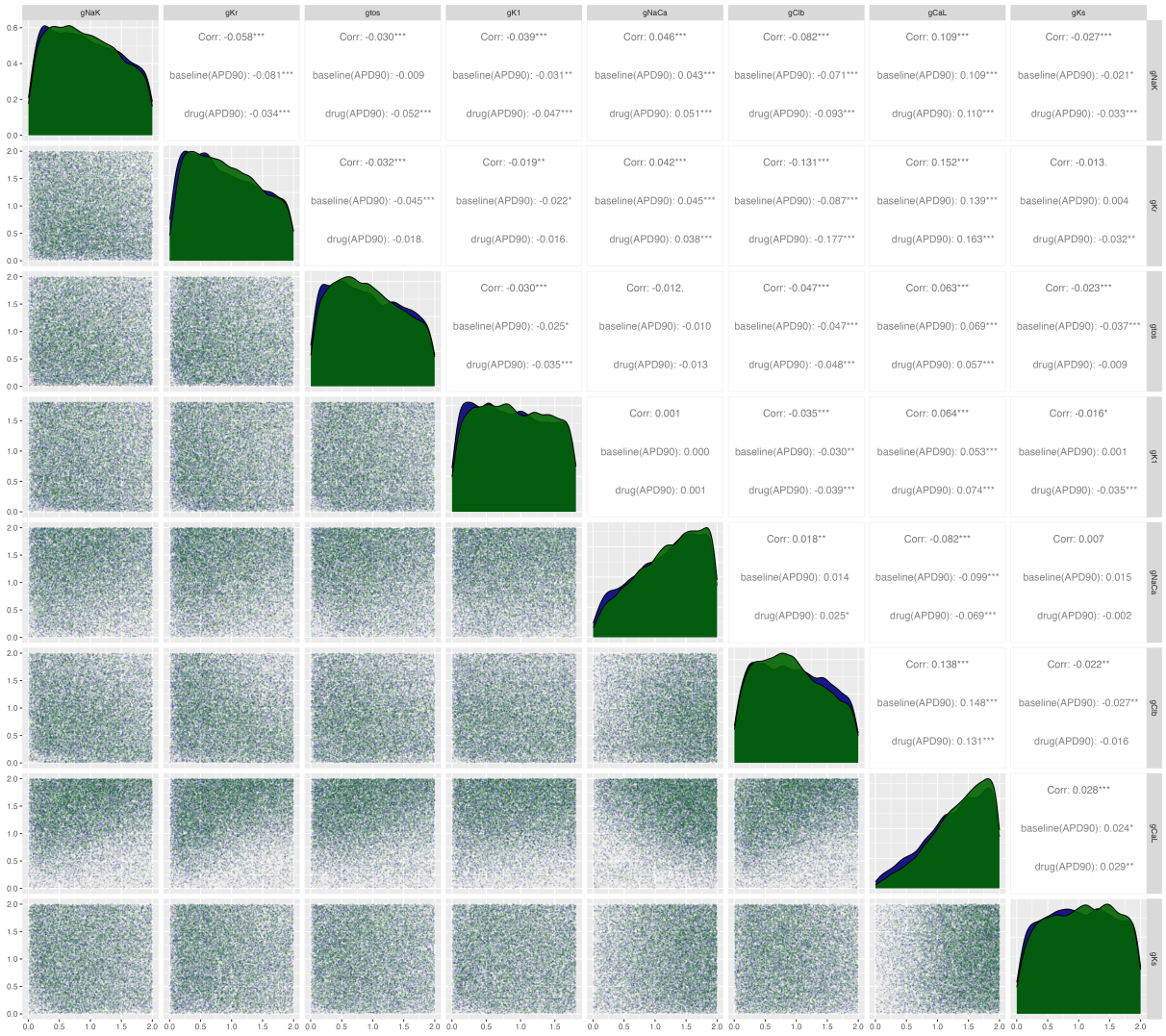

Figure 5.22: Pair plot visualising the relationships between conductances in the sampled APD90 population before and after Dofetilide administration. The navy colour represents the conductances at baseline, while the red colour represents the conductances after the drug application. Unlike the noticeable changes observed with Nifedipine, the impact of Dofetilide on the correlations and distributions of ion conductances is more moderate, indicating a less dramatic effect of this drug on the model population.

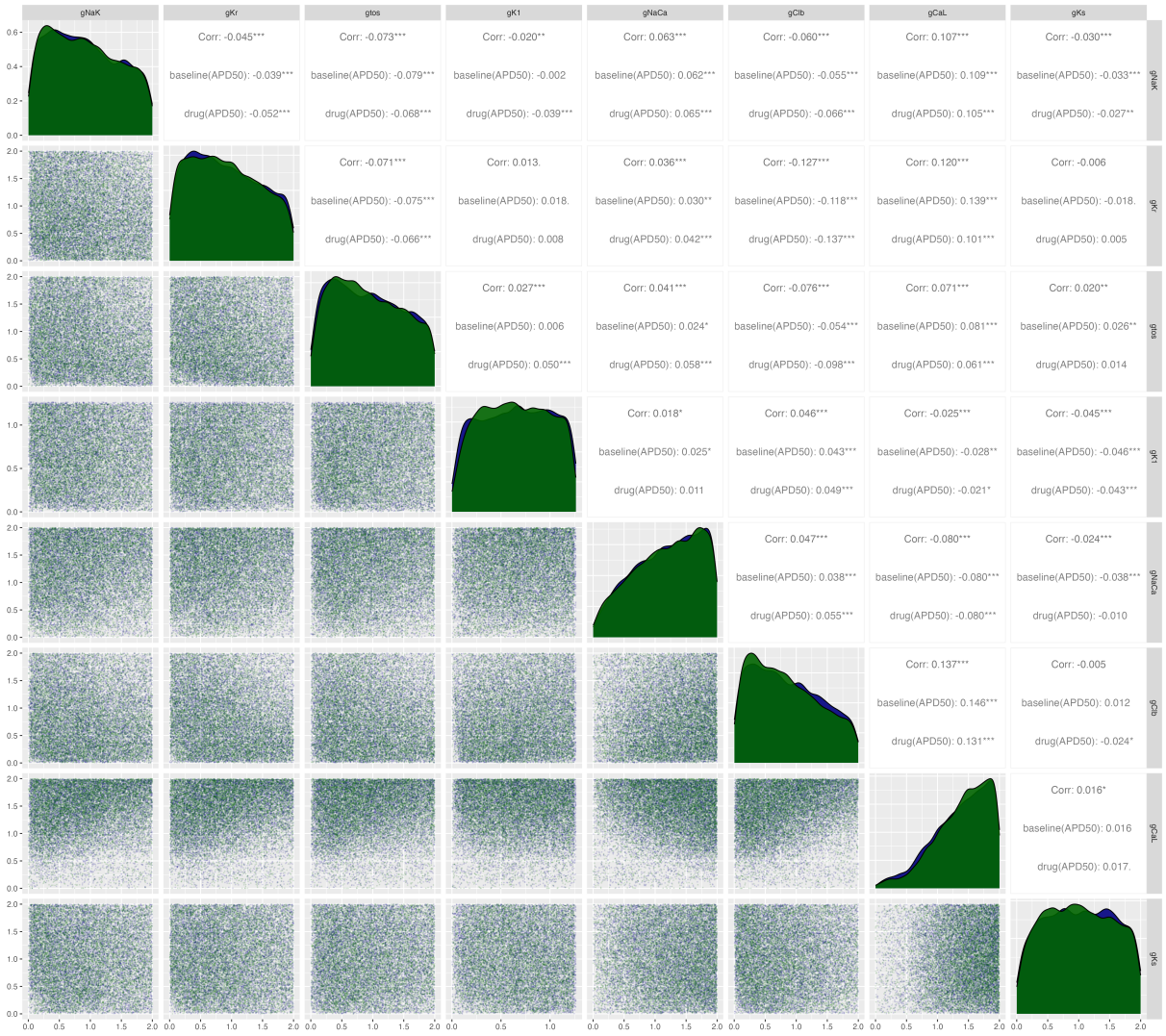

Figure 5.23: Pair plot visualising the relationships between conductances in the sampled APD50 population before and after Dofetilide administration. The navy colour represents the conductances at baseline, while the red colour represents the conductances after the drug application. Unlike the noticeable changes observed with Nifedipine, the impact of Dofetilide on the correlations and distributions of ion conductances is more moderate, indicating a less dramatic effect of this drug on the model population.

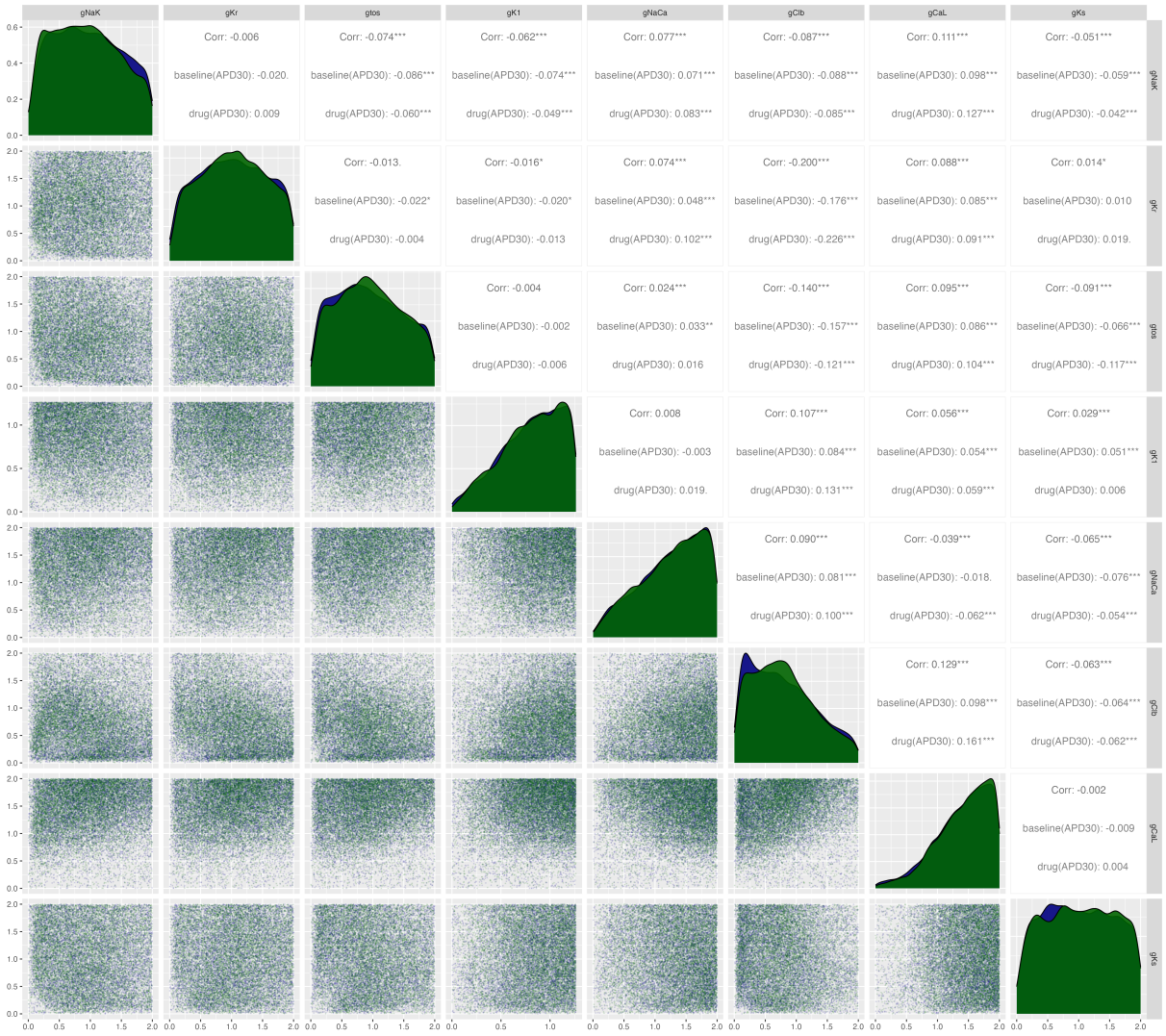

Figure 5.24: Pair plot visualising the relationships between conductances in the sampled APD30 population before and after Dofetilide administration. The navy colour represents the conductances at baseline, while the red colour represents the conductances after the drug application. Unlike the noticeable changes observed with Nifedipine, the impact of Dofetilide on the correlations and distributions of ion conductances is more moderate, indicating a less dramatic effect of this drug on the model population.

Chapter 6

Conclusion

In this chapter, we provide a comprehensive summary of our work and outcomes. We also discuss the limitations of our approaches and present a perspective on potential future advancements.

6.1 Summary of Results, Strengths and Limitations

Chapter 3

In Chapter 3, we present a comprehensive study that employed a simplified conceptual model of cellular excitability to analyse experimental measurements of ion channel blockade within a vast and diverse population of uncoupled cardiomyocytes. The experimental data, sourced from the work of (Lachaud et al. 2022), primarily consist of observations related to the shortening of action potential duration (APD) in nearly 500 rabbit ventricular myocytes. These cells, collected from various regions of the left ventricles across multiple animals, were subjected to an application of $1\mu\mathrm{M}$ of the drug nifedipine. This diverse sourcing resulted in a significant intrinsic variation in both the APD and the cellular response to the drug, a phenomenon already quantified in the original study by (Lachaud et al. 2022).

The primary objective of this analysis is to infer the intrinsic properties of each myocyte by determining cell-specific parameter values within a suitable mathematical framework. To this end, the McKean model (McKean Jr 1970) was selected due to its inherent simplicity and efficacy in capturing essential excitability dynamics. This model, characterised by a fast-slow system of piece-wise linear ordinary differential equations reminiscent of the FitzHugh-Nagumo type, incorporates two variables interpretable as voltage and an effective gating variable. It also includes two intrinsic parameters that can be viewed as an effective ion current conductance and an effective kinetic parameter. Within this framework, the authors delineate the parameter space domain where the model exhibits excitable dynamics, distinguishing it from oscillatory or bistable behaviors. They further derive an asymptotic approximation for the duration of $1:1$ action potentials generated under strictly periodic stimulation, leveraging standard fast-slow asymptotic analysis techniques (Fenichel 1979; Tikhonov 1952). This approximation appears as an explicit analytical expression for the APD as a function of the McKean model parameters and the basic cycle length of stimulation, denoted as $\alpha(a, b, \beta)$. Such relationships are commonly referred to as restitution curves in electrophysiological literature.

To model the pharmacological action of nifedipine, we introduce a multiplicative factor γ to the effective conductance parameter a. This modification leads to a set of nonlinear algebraic equations that, when solved, yield the McKean model parameters a_i and b_i for each cell $i = 1, \ldots, N$. These solutions can be determined using experimental measurements of the APDs A_i and $A_i + \Delta A_i$, recorded under periodic stimulation with a basic cycle length B before and after the application of the drug at concentration Γ. Intriguingly, this framework results in an adaptive domain problem where the parameter domain $\Omega_{\text{ex}}^{\gamma}(\beta, \gamma)$, along with the basic cycle length β and the drug dose parameter γ, must be determined as part of the solution. This determination is facilitated by introducing an additional modelling assumption: the Euclidean distance between the centroid of the domain and the algebraic mean of the McKean parameter values of the population is minimised. Through direct numerical evaluation, it is demonstrated that both the adaptive domain minimisation and the set of $2N$ nonlinear algebraic equations admit unique solutions, which are subsequently obtained using standard numerical routines.

Notably, the existence of $\Omega^{\gamma}_{\mathrm{ex}}(\beta,\gamma)$, distinct from $\Omega_{\mathrm{ex}}(\beta,\gamma)$, suggests that when incorporating heterogeneity into realistic models, parameter values should be selected from a restricted region of the parameter space. The findings derived from this study are subsequently utilised to:

- Further the understanding of the interrelationships proposed by (Lachaud et al. 2022), as necessary for ensuring the generation of stable AP morphology and repolarisation;
- Predict the scatter of APD values within the population in response to variations in basic cycle length and drug concentration;
- Calculate nifedipine drug-response curves for each cell in the population and ascertain the drug concentration required for each uncoupled cell, and the population collectively, to achieve a uniform APD value; (These predictions were investigated with experimental validation and showed agreement with independent experimental measurements (Himmel et al. 2012)
- Predict the proportion of cells that become inexcitable at elevated drug doses.

A significant strength of this work lies in its adept use of the McKean model (McKean Jr 1970) to interpret complex biological phenomena through a simplified mathematical model. The model's piece-wise linear nature facilitates exact solutions in closed form, enabling the derivation of explicit analytical expressions for key electrophysiological metrics such as the APD. This clarity not only aids in understanding the underlying dynamics but also in making precise predictions about cellular behavior in response to pharmacological interventions. The innovative approach of introducing an adaptive domain problem adds depth to the analysis, ensuring that the solutions are not just mathematically but also biologically relevant by accounting for the inherent heterogeneity within the myocyte population.

However, the reliance on an asymptotic expression for the APD, may not capture the full aspects observed in real-world data, and the fundamental mathematical structure of cardiac electrical excitability. Additionally, the exclusive focus on the drug action affecting the effective conductance parameter a, specifically in the context of APD shortening as induced by nifedipine, limits the generalisation of the findings. Other drugs, mechanisms of action, and scenarios such as APD prolongation remain unexplored within our research. Furthermore, the current model does not account for the coupling between myocytes, a factor that could significantly influence AP waveform synchronisation and tissue-wide responses.

Chapter 4

In Chapter 4, we carried out an extensive analysis to enhance the predictive power and understanding of cardiac electrophysiology models by integrating both linear and nonlinear regression techniques. The key findings from this chapter are summarised as follows:

- Successfully linked variations in ion channel expression to physiological phenomena such as action potentials (APs) and cellular calcium transients using ordinary least squares (OLS) regression models.
- Modelled the effects of a 30% reduction in GK conductance, simulating the impact of ion-channel block similar to Dofetilide experiments.
- Predicted APD90 values after drug application and compared them to simulated data, showcasing the practical utility of the OLS regression in predicting drug responses.
- Demonstrated the effectiveness of combining parameter randomisation with regression to assess parameter sensitivity in complex computational models.
- Enhanced the analysis by incorporating nonlinear predictors, particularly the squares of biomarker values, when applying stepwise regression with backward selection.
- Improved model accuracy through the careful selection of predictor variables, minimising overfitting and offering deeper insights into the relationships between ion channel conductances and physiological outputs.

The strengths of our methodology are multifaceted, offering significant improvements in the predictive power and accuracy of computational models, particularly in cardiac electrophysiology. By combining Ordinary Least Squares (OLS) regression with nonlinear modelling, we are able to conduct a more comprehensive analysis that shows the complex dependencies between ion channel conductances and physiological outputs. This detailed approach not enhances our understanding of these relationships andves highly practical for sensitivity analysis and predicting drug responses, making it a valuable tool in drug development research.

Incorporating nonlinear terms adds complexity to models, making them harder to interpret and requiring more computational resources. The method can be unstable, with small data changes leading to different model selections. Multicollinearity arises when predictor variables are highly correlated, potentially distorting the regression results. In our analysis, we addressed this by removing three biomarkers that exhibited high correlations with others. For instance, action potential amplitude (APA) was strongly correlated with Vmax, leading us to retain Vmax and exclude APA to avoid redundancy in the model. While stepwise regression helps reduce overfitting, it can still occur, especially with small or noisy datasets, affecting the results' applicability. Additionally, the accuracy of regression models depends on the quality of input data, and the methods may vary in effectiveness across different biological systems, requiring careful application beyond cardiac electrophysiology.

Chapter 5

In Chapter 5, we investigated the variability of action potentials (APs) in a population of rabbit cardiomyocytes under both controlled and drug-induced conditions, using rejection sampling combined with Gaussian Process (GP) emulators. The primary goal was to gain insights into the underlying mechanisms driving this variability and to explore how it influences drug action. The key findings from this study are summarised as follows:

- Successfully implemented GP emulators as an alternative to traditional simulators, significantly reducing computational cost and time in generating and analysing large populations of models.

- Accurately reproduced the heterogeneous experimental data recorded by (Lachaud et al. 2022), ensuring that the generated populations of models were well-calibrated to match observed experimental APD90 ranges.
- Conducted a detailed analysis of the corresponding ion conductances in the generated populations, providing valuable insights into the causes of variability in action potentials across cells.
- Performed a quantitative comparison of the effects of drug-induced channel blocks, particularly hERG and L-type calcium channels, with previous results, highlighting consistencies and differences between different modelling approaches.

The methodology introduced in Chapter 5 offers several strengths, particularly in the efficienc model generation and analysis efficiency. Gaussian Process (GP) emulators represents a significant advancement over traditional simulators by dramatically reducing computational cost and time, making it feasible to generate and analyse large populations of models. This efficiency does not come at the cost of accuracy, as the GP emulators were able to reproduce the heterogeneous experimental data with high fidelity, ensuring that the models remained well-calibrated to the observed data. Additionally, the ability to conduct a comprehensive analysis of ion conductances within the generated populations provides deep insights into the mechanisms driving variability in action potentials, which is crucial for understanding drug effects. The approach also facilitates direct comparisons with previous studies, allowing for the interpretation of drug-induced variability in cardiac cells.

The methodology presented in Chapter 5, while innovative and efficient, has some limitations. One key issue is the potential instability in the rejection sampling process when using Gaussian Process (GP) emulators, where small changes in input data could lead to different models being selected, affecting result consistency. Although GP emulators reduce computational costs, they might not fully capture the complex, nonlinear relationships between ion conductances and action potentials in all cases. The accuracy of the emulators is also highly dependent on the quality of the experimental data used for calibration; any inaccuracies in

this data could lead to incorrect conclusions. Additionally, the method may struggle with multicollinearity, where highly correlated ion conductance variables can distort the analysis and complicate the interpretation of the results. Finally, while the approach is practical for large populations, it may need further validation for use with different species or under varying conditions, limiting its broader applicability.

6.2 Future work

Expanding upon the foundation laid out in this thesis, many potential areas for future research can help us gain a deeper understanding of cardiac excitability, improve our knowledge of drug interactions, and advance the application of these findings in medical treatments.

Chapter 3

- **Enhancing Model Accuracy:** Given the piece-wise linear nature of the McKean model (McKean Jr 1970), it's feasible to replace the asymptotic expression used for APD with more precise exact expressions. This refinement would enable the incorporation of experimental measurements of secondary AP biomarkers, such as the action potential duration at 50% and 30% from the peak, which are currently indistinguishable using the present asymptotic approach.

- **Exploring Alternative Models:** Introducing the caricature Noble model, as proposed by (Biktashev et al. 2008), could offer a more comprehensive representation of cardiac excitability. Derived through a systematic procedure from an actual ionic current model, this model captures the fundamental mathematical structure of cardiac electrical excitability. Importantly, it includes a super-fast subsystem, absent in the McKean model, allowing for the analysis of biomarkers describing the initial phase of the action potential, such as the time from 10% to 90% of the upstroke (TRise). This aspect is crucial for understanding cellular processes distinct from those governing APD. The caricature Noble model has been recently tailored to replicate the action potential morphology and restitution properties of various cardiomyocyte phenotypes (Aziz and Simitev 2021) and possesses known exact and asymptotic solutions (Biktashev et al. 2008; Simitev and Biktashev 2011), albeit with increased complexity.

- **Broadening Drug Action Scenarios:** The current analysis focuses solely on the drug action affecting the effective conductance parameter a, particularly in the context of APD shortening as relevant to the nifedipine dataset of (Lachaud et al. 2022). Future investigations should explore scenarios involving APD prolongation and drug actions impacting the effective kinetic parameter b. For instance, the drug Dofetilide induces APD prolongation, with corresponding measurements reported in (Lachaud et al. 2022). Analysing such cases would necessitate adapting the parameter domain of excitability differently, warranting dedicated exploration.

- **Incorporating Myocyte Coupling:** Extending the current methodology to account for the coupling between myocytes would provide insights into AP waveform synchronisation, a factor likely pivotal in generating stable action potential responses at the tissue level. Such an extension would bridge the gap between cellular-level dynamics and organ-level electrophysiological behavior.

Chapter 4

- **Refining Nonlinear Models:** In Chapter 4 we used the square terms of the predictors such as CaTa^2, future work could explore higher-order nonlinear terms like CaTa^3 or CaTa^4. Alternative nonlinear modelling techniques could be used, such as using interaction terms, i.e. (CaTa $\times$ APD90). This could improve the accuracy of nonlinear regression models, which might lead to a deeper understanding of the complex relationships between ion channel conductances and physiological outputs, revealing correlations that the squared terms failed to identify.

- **Validating with Experimental Data:** For the work in Chapter 4, future efforts could focus on validating the computational predictions with additional experimental data, which is critical for ensuring the accuracy and reliability of the developed models. By validating the regression models against a larger and more diverse set of experimental data, it would be possible to assess how well the models generalise to different physiological conditions and experimental setups.

- **Exploring Multi-Dimensional Sensitivity Analysis:** The work in Chapter 4 could be extended by considering multi-dimensional parameter spaces. In the current analysis, we evaluated the sensitivity of individual parameters (such as the conductance of a single ion channel) on biomarkers like APD or CaTa. However, ion channels do not operate in isolation, and their interactions, such as ($G_{\mathrm{CaL}} \times G_{\mathrm{Ks}}$) often play a critical role in shaping the overall electrophysiological behaviour of the cell. This step could provide a deeper understanding of how multiple ion channels interact and collectively influence cardiac electrophysiology.

- **Incorporating Machine Learning Techniques:** To address the limitations identified in Chapter 4, where traditional regression models were used, we introduced Gaussian Process (GP) emulation techniques in Chapter 5. While GP emulators improved the computational efficiency and ability to capture nonlinear interactions, there are additional machine-learning approaches that could further enhance the model's predictive power. The neural networks (NNs) could be integrated to model highly nonlinear and complex relationships between input and output variables. The NNs could be trained to predict APD, or drug effects by learning from experimental data. NNs can capture multi-dimensional dependencies and offer flexibility in modeling interactions between multiple ion channels and their effects on any biomarkers of interest.

Chapter 5

- **Enhancing GP Emulator Accuracy:** The GP emulators developed in Chapter 5 used the Radial Basis Function (RBF) kernal. Future work could refine the GP by integrating more advanced kernel functions such as periodic kernels to capture cyclic biological rhythms or non-stationary kernels for modeling variability that changes over time or across different conditions. Additionally, GP emulators could be combined with other machine learning techniques like neural networks or decision trees could be explored. For instance, using neural networks to capture highly nonlinear relationships and GP emulators to model uncertainty could create a more robust framework for handling the complexity of cardiac electrophysiology data. These enhancements would likely improve the accuracy and predictive power of the GP emulators, particularly when reproducing experimental data characterized by high variability, such as heterogeneous

drug responses or varying ionic conductances across large populations of cardiomyocytes. Incorporating these advanced techniques would also allow for better generalization across different experimental conditions, making the models more versatile in predicting physiological outcomes.

- **Optimizing Rejection Sampling Efficiency:** Although the use of GP emulators in Chapter 5 already improved computational efficiency, future work could explore ways to optimise the rejection sampling process further. This might involve analysing the previously accepted or rejected samples and looking for the ranges of the input spaces where models are more likely to meet the acceptance condition and less sample rejection. This shall improve the efficiency and reduce the number of rejected models, thereby speeding up the analysis and enabling the study of even larger populations.
- **Expanding to Multi-Output Analysis:** In Chapter 5, we only considered a single output at a time such as APD90 and we attempted 2 outputs at a time. Future research could extend the current methodology to a higher-dimensional level by considering multiple outputs simultaneously. For instance, analysing APD90, APD50, and APD30 together would allow us to generate a population of models with corresponding conductances related to all outputs. This multi-output approach could provide a deeper understanding of how variations in ion conductances influence multiple aspects of cardiac function, offering more comprehensive insights into the underlying mechanisms and potentially revealing interactions between different physiological parameters.
- **Expanding Drug Response Models:** Extending the current work to include a wider variety of drug responses, including those affecting different ion channels or those with more complex mechanisms of action, could provide a broader understanding of how drugs influence cardiac cells. This could also involve studying multi-drug interactions to assess how combinations of drugs impact action potentials.

- **Exploring Heterogeneity in Different Cell Types:** While the current work in Chapter 5 focused on rabbit ventricular cardiomyocytes, future studies could explore heterogeneity in other species including human cardiomyocytes, atrial myocytes, or Purkinje fibers. For example, analyzing human atrial myocytes may provide insights into atrial fibrillation mechanisms. Expanding the model to these different cell types could help reveal cell-type-specific responses to drugs and contribute to a better understanding of cardiac diseases across species and regions of the heart.

By pursuing these future research directions, the work presented in Chapters 3, 4, and 5 could be significantly expanded, leading to a more comprehensive understanding of cardiac electrophysiology and its applications in drug development.

Bibliography

Aliev, Rubin R and Alexander V Panfilov (1996). “A simple two-variable model of cardiac excitation.” In: *Chaos, Solitons & Fractals* 7.3, pp. 293–301.

András, Varró et al. (2021). “Cardiac transmembrane ion channels and action potentials: cellular physiology and arrhythmogenic behavior.” In: *Physiological reviews*.

Anumonwo, Justus M and Sandeep V Pandit (2015). “Ionic mechanisms of arrhythmogenesis.” In: *Trends in cardiovascular medicine* 25.6, pp. 487–496.

Aziz, Muhamad HN and Radostin D Simitev (2021). “Estimation of parameters for an archetypal model of cardiomyocyte membrane potentials.” In: *arXiv preprint arXiv:2105.06853*.

Bai, Jieyun et al. (2018). “Ionic and cellular mechanisms underlying TBX5/PITX2 insufficiency-induced atrial fibrillation: Insights from mathematical models of human atrial cells.” In: *Scientific reports* 8.1, p. 15642.

Banyasz, Tamas et al. (2011). “Sequential dissection of multiple ionic currents in single cardiac myocytes under action potential-clamp.” In: *Journal of molecular and cellular cardiology* 50.3, pp. 578–581.

Barkley, Dwight (1991). “A model for fast computer simulation of waves in excitable media.” In: *Physica D: Nonlinear Phenomena* 49.1-2, pp. 61–70.

Benemerito, Ivan et al. (2022). “Reducing the complexity of musculoskeletal models using gaussian process emulators.” In: *Applied Sciences* 12.24, p. 12932.

Benitah, Jean-Pierre, Julio L Alvarez, and Ana María Gómez (2010). “L-type Ca2+ current in ventricular cardiomyocytes.” In: *Journal of molecular and cellular cardiology* 48.1, pp. 26–36.

Bers, Donald (2001). *Excitation-contraction coupling and cardiac contractile force*. Vol. 237. Springer Science & Business Media.

Biktashev, Vadim N et al. (2008). “Asymptotic analysis and analytical solutions of a model of cardiac excitation.” In: *Bulletin of mathematical biology* 70, pp. 517–554.

Bland, J Martin and DouglasG Altman (1986). “Statistical methods for assessing agreement between two methods of clinical measurement.” In: *The lancet* 327.8476, pp. 307–310.

Bonow, Robert O et al. (2011). *Braunwald’s heart disease e-book: A textbook of cardiovascular medicine*. Elsevier Health Sciences.

Britton, Oliver J et al. (2013). “Experimentally calibrated population of models predicts and explains intersubject variability in cardiac cellular electrophysiology.” In: *Proceedings of the National Academy of Sciences* 110.23, E2098–E2105.

Britton, Oliver J et al. (2014). “Effect of inter-subject variability in determining response to IKr block in human ventricular myocytes.” In: *Computing in Cardiology 2014*. IEEE, pp. 869–872.

Bueno-Orovio, Alfonso et al. (2012). “In vivo human left-to-right ventricular differences in rate adaptation transiently increase pro-arrhythmic risk following rate acceleration.” In: *PLoS One* 7.12, e52234.

Chang, Eugene TY, Mark Strong, and Richard H Clayton (2015). “Bayesian sensitivity analysis of a cardiac cell model using a Gaussian process emulator.” In: *PloS one* 10.6, e0130252.

Charnet, P et al. (1987). “Electrophysiological analysis of the action of nifedipine and nicardipine on myocardial fibers.” In: *Fundamental & clinical pharmacology* 1.6, pp. 413–431.

Clark, Alexander P et al. (2023). “Rapid ionic current phenotyping (RICP) identifies mechanistic underpinnings of iPSC-CM AP heterogeneity.” In: *bioRxiv*.

Clayton, Richard H et al. (2020). “An audit of uncertainty in multi-scale cardiac electrophysiology models.” In: *Philosophical Transactions of the Royal Society A* 378.2173, p. 20190335.

Corrias, A et al. (2010). “Arrhythmic risk biomarkers for the assessment of drug cardiotoxicity: from experiments to computer simulations.” In: *Philosophical Transactions of the Royal Society A: Mathematical, Physical and Engineering Sciences* 368.1921, pp. 3001–3025.

Courtemanche, Marc, Rafael J Ramirez, and Stanley Nattel (1998). “Ionic mechanisms underlying human atrial action potential properties: insights from a mathematical model.” In: *American Journal of Physiology-Heart and Circulatory Physiology* 275.1, H301–H321.

Coveney, Sam and Richard H Clayton (2020). “Sensitivity and uncertainty analysis of two human atrial cardiac cell models using Gaussian process emulators.” In: *Frontiers in Physiology* 11, p. 517249.

Crumb Jr, William J et al. (2016). “An evaluation of 30 clinical drugs against the comprehensive in vitro proarrhythmia assay (CiPA) proposed ion channel panel.” In: *Journal of pharmacological and toxicological methods* 81, pp. 251–262.

Cummins, Megan A et al. (2014). “Comprehensive analyses of ventricular myocyte models identify targets exhibiting favorable rate dependence.” In: *PLoS computational biology* 10.3, e1003543.

Darbar, Dawood (2018). “112 - Standard Antiarrhythmic Drugs.” In: *Cardiac Electrophysiology: From Cell to Bedside (Seventh Edition)*. Ed. by Douglas P. Zipes, José Jalife, and William G. Stevenson. Seventh Edition. Elsevier, pp. 1062–1075. ISBN: 978-0-323-44733-1. DOI: https://doi.org/10.1016/B978-0-323-44733-1.00112-7. URL: https://www.sciencedirect.com/science/article/pii/B9780323447331001127.

Davies, Mark Ri et al. (2012). “An in silico canine cardiac midmyocardial action potential duration model as a tool for early drug safety assessment.” In: *American Journal of Physiology-Heart and Circulatory Physiology* 302.7, H1466–H1480.

Devenyi, Ryan A and Eric A Sobie (2016). “There and back again: Iterating between population-based modeling and experiments reveals surprising regulation of calcium transients in rat cardiac myocytes.” In: *Journal of molecular and cellular cardiology* 96, pp. 38–48.

Dhamoon, Amit S and José Jalife (2005). “The inward rectifier current (IK1) controls cardiac excitability and is involved in arrhythmogenesis.” In: *Heart rhythm* 2.3, pp. 316–324.

Di Francesco, Dario and Denis Noble (1985). “A model of cardiac electrical activity incorporating ionic pumps and concentration changes.” In: *Philosophical Transactions of the Royal Society of London. B, Biological Sciences* 307.1133, pp. 353–398.

Fall, Christopher P et al. (2002). “Computational cell biology.” In: *New York*.

Feeny, Albert K et al. (2020). “Artificial intelligence and machine learning in arrhythmias and cardiac electrophysiology.” In: *Circulation: Arrhythmia and Electrophysiology* 13.8, e007952.

Feng, Jianlin et al. (1998). “Ionic mechanisms of regional action potential heterogeneity in the canine right atrium.” In: *Circulation research* 83.5, pp. 541–551.

Fenichel, Neil (1979). “Geometric singular perturbation theory for ordinary differential equations.” In: *Journal of differential equations* 31.1, pp. 53–98.

Fenton, Flavio H and Elizabeth M Cherry (2008). “Models of cardiac cell.” In: *Scholarpedia* 3.8, p. 1868.

Fink, Martin et al. (2011). “Cardiac cell modelling: observations from the heart of the cardiac physiome project.” In: *Progress in biophysics and molecular biology* 104.1-3, pp. 2–21.

FitzHugh, Richard (1961). “Impulses and physiological states in theoretical models of nerve membrane.” In: *Biophysical journal* 1.6, pp. 445–466.

Fox, Jeffrey J, Jennifer L McHarg, and Robert F Gilmour Jr (2002). “Ionic mechanism of electrical alternans.” In: *American Journal of Physiology-Heart and Circulatory Physiology* 282.2, H516–H530.

Gao, Jia et al. (2020). “Application of electrophysiological technique in toxicological study: from manual to automated patch-clamp recording.” In: *TrAC Trends in Analytical Chemistry* 133, p. 116082.

Geladi, Paul and Bruce R Kowalski (1986). “Partial least-squares regression: a tutorial.” In: *Analytica chimica acta* 185, pp. 1–17.

Gemmell, Philip et al. (2014). “Population of computational rabbit-specific ventricular action potential models for investigating sources of variability in cellular repolarisation.” In: *PLoS One* 9.2, e90112.

Gilks, Walter R, Gareth O Roberts, and Edward I George (1994). “Adaptive direction sampling.” In: *Journal of the Royal Statistical Society: Series D (The Statistician)* 43.1, pp. 179–189.

Gilks, Walter R and Pascal Wild (1992). “Adaptive rejection sampling for Gibbs sampling.” In: *Journal of the Royal Statistical Society: Series C (Applied Statistics)* 41.2, pp. 337–348.

Gong, Jingqi QX and Eric A Sobie (2018). “Population-based mechanistic modeling allows for quantitative predictions of drug responses across cell types.” In: *Biophysical Journal* 114.3, 472a.

Grant, Augustus O (2009a). “Cardiac ion channels.” In: *Circulation: Arrhythmia and Electrophysiology* 2.2, pp. 185–194.

– (2009b). “Cardiac ion channels.” In: *Circulation: Arrhythmia and Electrophysiology* 2.2, pp. 185–194.

Groenendaal, Willemijn et al. (2015). “Cell-specific cardiac electrophysiology models.” In: *PLoS computational biology* 11.4, e1004242.

Han, Jianan, Xiao-Ping Zhang, and Fang Wang (2016). “Gaussian process regression stochastic volatility model for financial time series.” In: *IEEE Journal of Selected Topics in Signal Processing* 10.6, pp. 1015–1028.

Heijman, Jordi, Stefan H Hohnloser, and A John Camm (2021). “Antiarrhythmic drugs for atrial fibrillation: lessons from the past and opportunities for the future.” In: *EP Europace* 23.Supplement_2, pp. ii14–ii22.

Himmel, Herbert M et al. (2012). “Field and action potential recordings in heart slices: correlation with established in vitro and in vivo models.” In: *British journal of pharmacology* 166.1, pp. 276–296.

Hodgkin, Alan L and Andrew F Huxley (1952). “A quantitative description of membrane current and its application to conduction and excitation in nerve.” In: *The Journal of physiology* 117.4, p. 500.

Hund, Thomas J et al. (2008). “Role of activated CaMKII in abnormal calcium homeostasis and INa remodeling after myocardial infarction: insights from mathematical modeling.” In: *Journal of molecular and cellular cardiology* 45.3, pp. 420–428.

Iyer, Vivek, Reza Mazhari, and Raimond L Winslow (2004). “A computational model of the human left-ventricular epicardial myocyte.” In: *Biophysical journal* 87.3, pp. 1507–1525.

Johnstone, Ross H et al. (2016). “Uncertainty and variability in models of the cardiac action potential: Can we build trustworthy models?” In: *Journal of molecular and cellular cardiology* 96, pp. 49–62.

Jost, Norbert et al. (2013). “Ionic mechanisms limiting cardiac repolarization reserve in humans compared to dogs.” In: *The Journal of physiology* 591.17, pp. 4189–4206.

Kennedy, Marc C and Anthony O’Hagan (2001). “Bayesian calibration of computer models.” In: *Journal of the Royal Statistical Society: Series B (Statistical Methodology)* 63.3, pp. 425–464.

Koivumäki, Jussi T, Topi Korhonen, and Pasi Tavi (2011). “Impact of sarcoplasmic reticulum calcium release on calcium dynamics and action potential morphology in human atrial myocytes: a computational study.” In: *PLoS computational biology* 7.1, e1001067.

Kuehn, Christian et al. (2015). *Multiple time scale dynamics*. Vol. 191. Springer.

Künsch, Hans R (2005). “Recursive Monte Carlo filters: algorithms and theoretical analysis.” In: *Annals of Statistics*, pp. 1983–2021.

Kurata, Yasutaka et al. (2005). “Dynamical mechanisms of pacemaker generation in IK1-downregulated human ventricular myocytes: insights from bifurcation analyses of a mathematical model.” In: *Biophysical journal* 89.4, pp. 2865–2887.

Lachaud, Quentin et al. (2018). “High-throughput study of rabbit ventricle action potential populations in MI model.” In: *Biophysical Journal* 114.3, 625a.

Lachaud, Quentin et al. (2022). “Electrophysiological heterogeneity in large populations of rabbit ventricular cardiomyocytes.” In: *Cardiovascular research* 118.15, pp. 3112–3125.

Lancaster, M Cummins and EA Sobie (2016). “Improved prediction of drug-induced Torsades de Pointes through simulations of dynamics and machine learning algorithms.” In: *Clinical Pharmacology & Therapeutics* 100.4, pp. 371–379.

Lawson, Brodie AJ et al. (2018). “Unlocking data sets by calibrating populations of models to data density: A study in atrial electrophysiology.” In: *Science advances* 4.1, e1701676.

Lee, JH (1996). “The Na/K pump, resting potential and selective permeability in canine Purkinje fibres at physiologic and room temperatures.” In: *Experientia* 52.7, pp. 657–660.

Li, Zhihua et al. (2017). “Improving the in silico assessment of proarrhythmia risk by combining hERG (human ether-à-go-go-related gene) channel–drug binding kinetics and multichannel pharmacology.” In: *Circulation: Arrhythmia and Electrophysiology* 10.2, e004628.

Livshitz, Leonid and Yoram Rudy (2009). “Uniqueness and stability of action potential models during rest, pacing, and conduction using problem-solving environment.” In: *Biophysical journal* 97.5, pp. 1265–1276.

Luo, Ching-hsing and Yoram Rudy (1991). “A model of the ventricular cardiac action potential. Depolarization, repolarization, and their interaction.” In: *Circulation research* 68.6, pp. 1501–1526.

– (1994). “A dynamic model of the cardiac ventricular action potential. I. Simulations of ionic currents and concentration changes.” In: *Circulation research* 74.6, pp. 1071–1096.

Mahajan, Aman et al. (2008). “A rabbit ventricular action potential model replicating cardiac dynamics at rapid heart rates.” In: *Biophysical journal* 94.2, pp. 392–410.

Maleckar, Mary M et al. (2009). “K+ current changes account for the rate dependence of the action potential in the human atrial myocyte.” In: *American Journal of Physiology-Heart and Circulatory Physiology* 297.4, H1398–H1410.

Marder, Eve and Adam L Taylor (2011). “Multiple models to capture the variability in biological neurons and networks.” In: *Nature neuroscience* 14.2, pp. 133–138.

McAllister, Ro E, Dt Noble, and RW Tsien (1975). “Reconstruction of the electrical activity of cardiac Purkinje fibres.” In: *The Journal of physiology* 251.1, pp. 1–59.

McEntire, Kira D et al. (2021). “Understanding drivers of variation and predicting variability across levels of biological organization.” In: *Integrative and Comparative Biology* 61.6, pp. 2119–2131.

McKay, Michael D, Richard J Beckman, and William J Conover (2000). “A comparison of three methods for selecting values of input variables in the analysis of output from a computer code.” In: *Technometrics* 42.1, pp. 55–61.

McKean Jr, HP (1970). “Nagumo’s equation.” In: *Advances in mathematics* 4.3, pp. 209–223.

Melis, Alessandro, Richard H Clayton, and Alberto Marzo (2017). “Bayesian sensitivity analysis of a 1D vascular model with Gaussian process emulators.” In: *International Journal for Numerical Methods in Biomedical Engineering* 33.12, e2882.

Michael, Georghia et al. (2009). “Remodelling of cardiac repolarization: how homeostatic responses can lead to arrhythmogenesis.” In: *Cardiovascular research* 81.3, pp. 491–499.

Miller, Andrew K et al. (2010). “An overview of the CellML API and its implementation.” In: *BMC bioinformatics* 11, pp. 1–12.

Miller, Jacob A, Seth H Weinberg, and Nicolae Moise (2023). “Modeling incomplete penetrance in long QT syndrome type 3 (LQT3) through ion channel heterogeneity: An in silico population study.” In: *Biophysical Journal* 122.3, 379a.

Mirams, Gary R et al. (2011). “Simulation of multiple ion channel block provides improved early prediction of compounds clinical torsadogenic risk.” In: *Cardiovascular research* 91.1, pp. 53–61.

Mitchell, Colleen C and David G Schaeffer (2003). “A two-current model for the dynamics of cardiac membrane.” In: *Bulletin of mathematical biology* 65.5, pp. 767–793.

Mori, Shumpei et al. (2019). “What is the real cardiac anatomy?” In: *Clinical Anatomy* 32.3, pp. 288–309.

Morotti, Stefano and Eleonora Grandi (2017). “Logistic regression analysis of populations of electrophysiological models to assess proarrythmic risk.” In: *MethodsX* 4, pp. 25–34.

Morotti, Stefano et al. (2016). “Atrial-selective targeting of arrhythmogenic phase-3 early afterdepolarizations in human myocytes.” In: *Journal of molecular and cellular cardiology* 96, pp. 63–71.

Müllenbroich, M Caroline et al. (2021). “Novel optics-based approaches for cardiac electrophysiology: a review.” In: *Frontiers in physiology* 12, p. 769586.

Muszkiewicz, Anna et al. (2016). “Variability in cardiac electrophysiology: using experimentally-calibrated populations of models to move beyond the single virtual physiological human paradigm.” In: *Progress in biophysics and molecular biology* 120.1-3, pp. 115–127.

Nagumo, Jinichi, Suguru Arimoto, and Shuji Yoshizawa (1962). “An active pulse transmission line simulating nerve axon.” In: *Proceedings of the IRE* 50.10, pp. 2061–2070.

National Health Service (n.d.). *Arrhythmia*. Accessed: 2024-06-19. URL: https://www.nhs.uk/conditions/arrhythmia/.

Nelder, John A and Roger Mead (1965). “A simplex method for function minimization.” In: *The computer journal* 7.4, pp. 308–313.

Ni, Haibo, Stefano Morotti, and Eleonora Grandi (2018). “A heart for diversity: simulating variability in cardiac arrhythmia research.” In: *Frontiers in physiology* 9, p. 391359.

Ni, Haibo et al. (2020). “Populations of in silico myocytes and tissues reveal synergy of multiatrial-predominant K+-current block in atrial fibrillation.” In: *British journal of pharmacology* 177.19, pp. 4497–4515.

Noble, Denis (1962). “A modification of the HodgkinHuxley equations applicable to Purkinje fibre action and pacemaker potentials.” In: *The Journal of physiology* 160.2, p. 317.

Nygren, Anders et al. (1998). “Mathematical model of an adult human atrial cell: the role of K+ currents in repolarization.” In: *Circulation research* 82.1, pp. 63–81.

Odening, Katja E et al. (2021). “ESC working group on cardiac cellular electrophysiology position paper: relevance, opportunities, and limitations of experimental models for cardiac electrophysiology research.” In: *EP Europace* 23.11, pp. 1795–1814.

O’Hara, Thomas et al. (2011). “Simulation of the undiseased human cardiac ventricular action potential: model formulation and experimental validation.” In: *PLoS computational biology* 7.5, e1002061.

Paci, Michelangelo et al. (2013). “Computational models of ventricular-and atrial-like human induced pluripotent stem cell derived cardiomyocytes.” In: *Annals of biomedical engineering* 41, pp. 2334–2348.

Padala, Santosh K, José-Angel Cabrera, and Kenneth A Ellenbogen (2021). “Anatomy of the cardiac conduction system.” In: *Pacing and Clinical Electrophysiology* 44.1, pp. 15–25.

Pandit, Sandeep V (2018). “Ionic mechanisms of atrial action potentials.” In: *Cardiac electrophysiology: from cell to bedside*, pp. 293–303.

Passini, Elisa, Simonetta Genovesi, and Stefano Severi (2014). “Human atrial cell models to analyse haemodialysis-related effects on cardiac electrophysiology: work in progress.” In: *Computational and Mathematical Methods in Medicine* 2014.1, p. 291598.

Passini, Elisa et al. (2016). “Mechanisms of pro-arrhythmic abnormalities in ventricular repolarisation and anti-arrhythmic therapies in human hypertrophic cardiomyopathy.” In: *Journal of molecular and cellular cardiology* 96, pp. 72–81.

Polak, Sebastian and Kamil Fijorek (2012). “Inter-individual variability in the pre-clinical drug cardiotoxic safety assessmentanalysis of the age–cardiomyocytes electric capacitance dependence.” In: *Journal of cardiovascular translational research* 5, pp. 321–332.

Pontryagin, LS (1957). “The asymptotic behaviour of systems of differential equations with a small parameter multiplying the highest derivatives.” In: *Izv. Akad. Nauk SSSR, Ser. Mat* 21.5, pp. 107–155.

Pouranbarani, Elnaz, Rodrigo Weber dos Santos, and Anders Nygren (2019). “A robust multiobjective optimization framework to capture both cellular and intercellular properties in cardiac cellular model tuning: Analyzing different regions of membrane resistance profile in parameter fitting.” In: *PloS one* 14.11, e0225245.

Powell, Michael JD (1970). “A hybrid method for nonlinear equations.” In: *Numerical methods for nonlinear algebraic equations*, pp. 87–161.

Pueyo, Esther et al. (2010). “Mechanisms of ventricular rate adaptation as a predictor of arrhythmic risk.” In: *American Journal of Physiology-Heart and Circulatory Physiology* 298.5, H1577–H1587.

Ridley, Gavin and Benoit Forget (2021). “A simple method for rejection sampling efficiency improvement on SIMT architectures.” In: *Statistics and Computing* 31, pp. 1–11.

Robert, Christian P, George Casella, and George Casella (1999). *Monte Carlo statistical methods*. Vol. 2. Springer.

Roberts, Stephen et al. (2013). “Gaussian processes for time-series modelling.” In: *Philosophical Transactions of the Royal Society A: Mathematical, Physical and Engineering Sciences* 371.1984, p. 20110550.

Romero, Lucía et al. (2009). “Impact of ionic current variability on human ventricular cellular electrophysiology.” In: *American Journal of Physiology-Heart and Circulatory Physiology* 297.4, H1436–H1445.

Sakakibara, Yusaku et al. (1993). “Sodium current in isolated human ventricular myocytes.” In: *American Journal of Physiology-Heart and Circulatory Physiology* 265.4, H1301–H1309.

Sánchez, Carlos et al. (2014). “Inter-subject variability in human atrial action potential in sinus rhythm versus chronic atrial fibrillation.” In: *PloS one* 9.8, e105897.

Sarkar, Amrita X, David J Christini, and Eric A Sobie (2012). “Exploiting mathematical models to illuminate electrophysiological variability between individuals.” In: *The Journal of physiology* 590.11, pp. 2555–2567.

Sarkar, Amrita X and Eric A Sobie (2010). “Regression analysis for constraining free parameters in electrophysiological models of cardiac cells.” In: *PLoS computational biology* 6.9, e1000914.

Saxton, Anthony, Muhammad Ali Tariq, and Bruno Bordoni (2023). “Anatomy, thorax, cardiac muscle.” In: *StatPearls [Internet]*. StatPearls Publishing.

Shannon, Thomas R et al. (2004). “A mathematical treatment of integrated Ca dynamics within the ventricular myocyte.” In: *Biophysical journal* 87.5, pp. 3351–3371.

Shaw, Robin M and Yoram Rudy (1997). “Electrophysiologic effects of acute myocardial ischemia: a theoretical study of altered cell excitability and action potential duration.” In: *Cardiovascular research* 35.2, pp. 256–272.

Simitev, Radostin D et al. (2023). “Phenomenological analysis of simple ion channel block in large populations of uncoupled cardiomyocytes.” In: *Mathematical Medicine and Biology: A Journal of the IMA* 40.2, pp. 175–198.

Simitev, RD and VN Biktashev (2011). “Asymptotics of conduction velocity restitution in models of electrical excitation in the heart.” In: *Bulletin of Mathematical Biology* 73, pp. 72–115.

Sims, Carl et al. (2008). “Sex, age, and regional differences in L-type calcium current are important determinants of arrhythmia phenotype in rabbit hearts with drug-induced long QT type 2.” In: *Circulation research* 102.9, e86–e100.

Sobie, Eric A (2009). “Parameter sensitivity analysis in electrophysiological models using multivariable regression.” In: *Biophysical journal* 96.4, pp. 1264–1274.

Sobie, Eric A and Amrita X Sarkar (2011). “Regression methods for parameter sensitivity analysis: applications to cardiac arrhythmia mechanisms.” In: *2011 Annual International Conference of the IEEE Engineering in Medicine and Biology Society*. IEEE, pp. 4657–4660.

Syed, Z et al. (2005). “Atrial cell action potential parameter fitting using genetic algorithms.” In: *Medical and Biological Engineering and Computing* 43, pp. 561–571.

Ten Tusscher, Kirsten HWJ and Alexander V Panfilov (2006). “Alternans and spiral breakup in a human ventricular tissue model.” In: *American Journal of Physiology-Heart and Circulatory Physiology* 291.3, H1088–H1100.

Tikhonov, Andrei Nikolaevich (1952). “Systems of differential equations containing small parameters in the derivatives.” In: *Matematicheskii sbornik* 73.3, pp. 575–586.

Tixier, Eliott et al. (2017). “Modelling variability in cardiac electrophysiology: a moment-matching approach.” In: *Journal of the Royal Society Interface* 14.133, p. 20170238.

Trayanova, Natalia A (2011). “Whole-heart modeling: applications to cardiac electrophysiology and electromechanics.” In: *Circulation research* 108.1, pp. 113–128.

Trayanova, Natalia A et al. (2023). “Computational modeling of cardiac electrophysiology and arrhythmogenesis.” In: *Physiological Reviews*.

Trovato, Cristian et al. (2020). “Human Purkinje in silico model enables mechanistic investigations into automaticity and pro-arrhythmic abnormalities.” In: *Journal of molecular and cellular cardiology* 142, pp. 24–38.

Tsallis, Constantino and Daniel A Stariolo (1996). “Generalized simulated annealing.” In: *Physica A: Statistical Mechanics and its Applications* 233.1-2, pp. 395–406.

Tse, Gary (2016). “Mechanisms of cardiac arrhythmias.” In: *Journal of arrhythmia* 32.2, pp. 75–81.

Tusscher, Kirsten HWJ ten et al. (2004). “A model for human ventricular tissue.” In: *American Journal of Physiology-Heart and Circulatory Physiology* 286.4, H1573–H1589.

Virtanen, Pauli et al. (2020). “SciPy 1.0: fundamental algorithms for scientific computing in Python.” In: *Nature methods* 17.3, pp. 261–272.

Walmsley, John et al. (2015). “Application of stochastic phenomenological modelling to cell-to-cell and beat-to-beat electrophysiological variability in cardiac tissue.” In: *Journal of theoretical biology* 365, pp. 325–336.

Warren, Mark et al. (2010). “High-precision recording of the action potential in isolated cardiomyocytes using the near-infrared fluorescent dye di-4-ANBDQBS.” In: *American Journal of Physiology-Heart and Circulatory Physiology* 299.4, H1271–H1281.

Whittaker, Dominic G et al. (2020). “Calibration of ionic and cellular cardiac electrophysiology models.” In: *Wiley Interdisciplinary Reviews: Systems Biology and Medicine* 12.4, e1482.

Wikimedia Commons contributors (2024a). *Blausen 0457 Heart Sectional Anatomy*. Accessed: 20-Aug-2024. URL: https://commons.wikimedia.org/wiki/File:Blausen_0457_Heart_SectionalAnatomy.png.

– (2024b). *Conduction system of the heart*. Accessed: 20-Aug-2024. URL: https://commons.wikimedia.org/wiki/File:Conductionsystemoftheheart.png.

Wilhelms, Mathias et al. (2013). “Benchmarking electrophysiological models of human atrial myocytes.” In: *Frontiers in physiology* 3, p. 487.

Williams, Christopher KI and Carl Edward Rasmussen (2006). *Gaussian processes for machine learning*. Vol. 2. 3. MIT press Cambridge, MA.

Xiang, Yang and XG Gong (2000). “Efficiency of generalized simulated annealing.” In: *Physical Review E* 62.3, p. 4473.

Yang, Tao, Dirk Snyders, and Dan M Roden (2001). “Drug block of I Kr: model systems and relevance to human arrhythmias.” In: *Journal of cardiovascular pharmacology* 38.5, pp. 737–744.

Zeng, Jinglin and Yoram Rudy (1995). “Early afterdepolarizations in cardiac myocytes: mechanism and rate dependence.” In: *Biophysical journal* 68.3, pp. 949–964.

Zhou, Xin et al. (2013). “Population of human ventricular cell models calibrated with in vivo measurements unravels ionic mechanisms of cardiac alternans.” In: *Computing in Cardiology 2013*. IEEE, pp. 855–858.

Zhou, Xin et al. (2016). “In vivo and in silico investigation into mechanisms of frequency dependence of repolarization alternans in human ventricular cardiomyocytes.” In: *Circulation research* 118.2, pp. 266–278.

Zipes, Douglas P, Jose Jalife, and William Gregory Stevenson (2017). *Cardiac electrophysiology: from cell to bedside E-book*. Elsevier Health Sciences.